



2015-07-01

Geometry and Material Properties of Vocal Fold Models

Kimberly Ann Stevens

Brigham Young University - Provo

Follow this and additional works at: <https://scholarsarchive.byu.edu/etd>

 Part of the [Mechanical Engineering Commons](#)

BYU ScholarsArchive Citation

Stevens, Kimberly Ann, "Geometry and Material Properties of Vocal Fold Models" (2015). *All Theses and Dissertations*. 5595.
<https://scholarsarchive.byu.edu/etd/5595>

This Thesis is brought to you for free and open access by BYU ScholarsArchive. It has been accepted for inclusion in All Theses and Dissertations by an authorized administrator of BYU ScholarsArchive. For more information, please contact scholarsarchive@byu.edu, ellen_amatangelo@byu.edu.

Geometry and Material Properties of Vocal Fold Models

Kimberly Ann Stevens

A thesis submitted to the faculty of
Brigham Young University
in partial fulfillment of the requirements for the degree of
Master of Science

Scott L. Thomson, Chair
Brian D. Iverson
Jonathan J. Wisco

Department of Mechanical Engineering
Brigham Young University
July 2015

Copyright © 2015 Kimberly Ann Stevens
All Rights Reserved

ABSTRACT

Geometry and Material Properties of Vocal Fold Models

Kimberly Ann Stevens

Department of Mechanical Engineering, BYU

Master of Science

Voiced communication plays a fundamental role in society. Voice research seeks to improve understanding of the fundamental physics governing voice production, with the eventual goal of improving methods to diagnose and treat voice disorders. For this thesis, three different aspects of voice production research were studied. First, porcine vocal fold medial surface geometry was determined, and the three-dimensional geometric distortion induced by freezing the larynx, especially in the region of the vocal folds, was quantified. It was found that porcine vocal folds are qualitatively geometrically similar to canine and human vocal folds, as well as commonly used models, and that freezing of tissue in the larynx causes distortion of around 5%. Second, a setup of multiple high-resolution cameras and a stereo-endoscopy system simultaneously recorded positions on the superior surface of synthetic, self-oscillating vocal fold models to estimate the error in the measurement of the three-dimensional location by the stereo-endoscopy system. The error was found to be low in the transverse plane, whereas the error was relatively large in the inferior-superior direction, suggesting that the stereo-endoscope is applicable for *in vivo* measurements of absolute distances of the glottis in the transverse plane such as glottal length, width, and area. Third, a function for strain-varying Poisson's ratio for silicone was developed from experimental data. It is anticipated that the findings herein can aid voice researchers as they study voice production, leading to improved voice care.

Keywords: vocal folds, porcine vocal folds, vocal fold medial surface geometry, tissue distortion, histological processing, vocal fold modeling, Poisson's ratio, stereo-endoscopy, image processing

ACKNOWLEDGMENTS

Jeff Allen deserves acknowledgment for the fact that I actually pulled this research together into a thesis. Not only did he suggest it, but he convinced and persistently reminded me of the reasons it was a good idea when I was reluctant to do something I knew would be difficult. Kevin Cole has graciously come to the rescue on several occasions, and I'm grateful for his patient help. Thanks goes to the members of the Bio-fluids Lab and Splash Lab for good ideas and good times. Kevin Moore is responsible for the collection of the data presented in Chapter 4, and I appreciate his excellent work on that and several other projects.

Isao Tokuda provided a great deal of mentoring and support and helped with the development and writing of Chapter 3. He and the members of his lab gave me a warm welcome and helped me to have a great experience working in Japan. I'm grateful to Dr. Brian Iverson for being willing to let me work on my master's and PhD research simultaneously and for going above and beyond the work of a normal committee member. I appreciate valuable feedback on this thesis from him, Dr. Jonathon Wisco, and Dr. Anton Bowden.

I cannot sufficiently emphasize the impact my committee chair has had on not only this thesis and the research in general, but on me personally and professionally. Dr. Scott Thomson has consistently raised my vision of my potential and helped increase my confidence. I have him to thank that I ever began pursuing a PhD. His support, encouragement, advice, and willingness to listen have been an invaluable part of my graduate school experience. He has been "Brother Thomson" in all the right moments, and I'm grateful for his wisdom, inspiration, and example the last several years.

Everything that I am and have ever accomplished I can trace back to the unfailing support, excellent examples, and invaluable friendship of my parents. Similarly, I'm grateful to my Heavenly Father for countless blessing in my life, not the least of which is putting many of the good people mentioned above in my path. He has guided me and given me comfort throughout my life in ways I'm incapable of describing.

I gratefully acknowledge the funding sources that supported this research, including the National Science Foundation under grant number IIA-1414741 as part of the EASPI program and the National Institute on Deafness and Other Communications Disorders of the National Institute of Health, award number R01 DC005788 (Prof. Luc Mongeau, PI). Any opinions, findings, and conclusions or recommendations expressed in this material are those of the author and do not necessarily reflect the views of the National Science Foundation or National Institute of Health.

TABLE OF CONTENTS

LIST OF TABLES	vii
LIST OF FIGURES	viii
Chapter 1 Introduction	1
1.1 Context for Present Research	1
1.1.1 Larynx Anatomy and Function	1
1.1.2 Vocal Fold Research	3
1.2 Research Objectives	4
1.3 Thesis Overview	5
Chapter 2 Quantification of Porcine Vocal Fold Geometry¹	7
2.1 Introduction to Porcine Geometry Research	7
2.2 Methods	11
2.2.1 Medial Surface Profile	12
2.2.2 Tissue and Airway Volume	14
2.3 Results and Discussion	15
2.3.1 Medial Surface Profile	15
2.3.2 Tissue and Airway Volume	18
2.4 Conclusion	26
Chapter 3 Validating a Stereo-Endoscope with a Synthetic Vocal Fold Model	28
3.1 Introduction	28
3.2 Method	30
3.2.1 Experimental Setup	30
3.2.2 Stereo-endoscopy System	32
3.2.3 DSLR System	34
3.2.4 Application to Synthetic Vocal Fold Model	36
3.3 Results and Discussion	36
3.4 Conclusion	39
Chapter 4 Poisson's Ratio of Silicone	42
4.1 Introduction	42
4.2 Poisson's Ratio Estimates	43
4.3 Method	46
4.4 Results and Discussion	48
4.4.1 Length and Width Measurements	48
4.4.2 Poisson's Ratio	49
4.4.3 Comparison Between Types of Silicone	50
4.4.4 Poisson's Ratio Function	52
4.5 Conclusion	53
4.5.1 Future Work	53

Chapter 5	Conclusion	55
5.1	A Mother’s Lullaby	55
5.2	Chapter 2: Quantification of Porcine Vocal Fold Geometry	55
5.3	Chapter 3: Validating a Stereo-Endoscope with a Synthetic Vocal Fold Model	57
5.4	Chapter 4: Poisson’s Ratio of Silicone	57
REFERENCES		58
Appendix A	Relevant Matlab Code from Chapter 1	64
A.1	ExtractAreaALL.m	64
A.2	PickThreshAuto.m	69
Appendix B	Image Processing details from Chapter 3	71
B.1	Overview	71
B.2	Ground-Truth System Calibration	71
B.3	Ground-Truth System Reconstruction	79
B.4	Stereo-endoscope Reconstruction	85
	B.4.1 trackdot3DStereo.m	85
	B.4.2 XCorrPts.m	87
	B.4.3 ReconstructStereoKS.m	89
B.5	Comparison Between Stereo-endoscope and Ground-truth Systems	91
Appendix C	MATLAB Code from Chapter 4	98
C.1	Overview	98
C.2	XCorrPtsPoisson.m	98
C.3	FindWidths.m	100
C.4	Smooth.m	103
C.5	Poisson.m	104
C.6	Compare.m	105

LIST OF TABLES

- 2.1 Percent change in volume between room temperature and frozen larynges. 22
- 3.1 Averaged estimation of error in each direction (mm) measured by distance between the stereo-endoscope and DSLR cameras. The phase of the glottal cycle is indicated by ϕ , where the zero phase corresponds to maximum glottal pressure. . . 40

LIST OF FIGURES

1.1	Sagittal (left) and coronal (middle) views of the vocal tract and larynx, with a transverse view at the level of the glottis (right) (adapted from Gray’s Anatomy of the Human Larynx [1]).	2
1.2	Diagram of a coronal view of the vocal folds depicting the various tissue layers. . .	3
2.1	Photographs of porcine Larynges 1 (a) and 2 (b).	11
2.2	Sagittal view of porcine larynx (left) and computer rendering of segmented porcine laryngeal airway (right).	12
2.3	Medial surface profile (left) and airway CAD model rendering (right)	13
2.4	Manual registration of Larynx 1 at room temperature (left column) to Larynx 1 when frozen (right column). The center column includes the overlap in yellow, the frozen tissue in green, and the room temperature tissue in red. The three rows are the three orthogonal views of the larynx that roughly correspond to the transverse, coronal, and sagittal planes. The yellow, red, and green lines show the locations of the coronal, sagittal, and transverse planes, respectively.	13
2.5	(a) Sample image from the transverse plane midway through the volume. These images were imported into MATLAB and the tissue or airway segmented, as follows. (b) The edges of the image were found using the method of Sorbel. (c) The border of the tissue was found automatically. (d) The location of the edge of the tissue for all the images in that plane was used to select a threshold, which was applied to all the images, and used to calculate the area of the tissue in that slice. Further details regarding this procedure can be found in Appendix A.	14
2.6	Left and right medial surface profiles of Larynges 1 through 5 (a through e, respectively) at room temperature.	15
2.7	(a) Average of left and right medial surface profiles of the five room temperature larynges, normalized. (b) Mean profile (solid line) of all five larynges, including left and right sides, and envelope corresponding to plus and minus one standard deviation (dotted line).	17
2.8	(a) Average of left and right medial surface profiles of the five frozen larynges, normalized. (b) Mean profile (solid line) of all five larynges, including left and right sides, and envelope corresponding to plus and minus one standard deviation (dotted line).	17
2.9	Mean frozen (dashed line) and room temperature (solid line) profiles	18
2.10	(a) Location of planes anterior and posterior to the mid-membranous plane. (b) Profiles from three planes: 2 mm anterior (dashed lines), mid-membranous (solid lines), 2 mm posterior (dotted lines).	19
2.11	Medial surface profile from present study along with profiles from human and canine data as well as with models from other studies.	20
2.12	Area of the tissue in the transverse plane for each of the five larynges (a through e), including room temperature (solid lines) and frozen (dashed lines). The horizontal and vertical scales of plots (a) through (d) are the same as those denoted by the axis labels in plot (e).	21

2.13	Normalized difference between room temperature and frozen larynges. The numbers 1-5 in the legend denote which of the five larynges.	22
2.14	Cross-sectional area of the airway in the transverse plane for each of the five larynges (a through e) when the tissue was at room temperature (solid lines) and frozen (dashed lines).	23
2.15	Tissue (larger) and airway (smaller) areas (e.g., as illustrated in plot e) in the sagittal plane for each of the five larynges (a through e), including room temperature (solid lines) and frozen (dashed lines)	24
2.16	Tissue (larger) and airway (smaller) areas in the coronal plane for each of the five larynges (a through e), including room temperature (solid lines) and frozen (dashed lines).	25
3.1	Grid of dots painted on the model to reduce error due to the correspondence problem.	31
3.2	The surface of the vocal folds was recorded simultaneously with two DSLR cameras and the stereo-endoscope.	31
3.3	Representative image from the stereo-endoscope.	33
3.4	Photograph of the stereo-endoscope	33
3.5	Sample calibration image	35
3.6	Image of the vocal fold model surface at $\phi = 92.6^\circ$, taken with the (a) DSLR and (b) stereo-endoscope and the (c,d) locations of the markers plotted in three-dimensions. Note the different scales on the vertical axes.	37
3.7	Locations of the marker points on the right vocal fold when (a) $\phi = 0^\circ$, (b) $\phi = 43.5^\circ$, and (c) $\phi = 73.1^\circ$. Note the different scales on the vertical axes.	38
4.1	Sample image of the DS6a sample after measuring the length and width. Triangles indicate the location of the edges used to calculate length; red and green points indicate the location of the edges used to calculate width over time as the sample was stretched.	45
4.2	(a) Window from previous image with edge marked. (b) Window from present image, showing the location of the edge at the previous step and the present step. (c and d) The cross-correlation with the peak, which indicates the location of the new edge, marked.	47
4.3	(a) Horizontal green lines indicate the location of the window used to find the width. (b) Sample at the location of the window, after thresholding.	48
4.4	Length (a) and width (b) of one sample before and after smoothing.	49
4.5	Poisson's ratio calculated four different ways, before (a) and after (b) smoothing. The legend is the same for (a) and (b).	50
4.6	Comparison of v_{xy}^{tot} between sets (a) and (b), showing the repeatability of the measurements. Set (b) is a duplicate of set (a).	51
4.7	Poisson's ratio, v_{xy}^{tot} , for the six types of silicone tested. (a) and (b) represent two separate sets of data. Note that the average of all the samples is also plotted and represents the behavior of the individual samples well.	52

CHAPTER 1. INTRODUCTION

1.1 Context for Present Research

”Help!” ”Stop!” ”Run!” From expressions of distress and alarm to comfort and encouragement, humans have always relied on verbal communication to convey messages of persuasion, instruction, and inspiration. Even with the increase in written communication seen in the last several centuries, voice is still one of the most utilized tools for communication. Voice plays a central role in social interactions with others. In addition, many professionals rely heavily on voice, including singers, coaches, actors, doctors, law enforcement officers, lawyers, and those involved in sales. However, 7.5 million people in the United States have trouble using their voices, significantly impacting their quality of life [2]. Those who frequently use their voice professionally, such as teachers, are at a significantly higher risk of having voice disorders [3]. Though many advances in understanding voice production and clinical treatment have been made over the years, much regarding the fundamental physics of voice production is still unknown. Improved understanding of how the deformation of vocal fold tissue leads to voice production and the development of tools for studying the voice can lead to better prevention, diagnosis, and treatment of voice disorders.

1.1.1 Larynx Anatomy and Function

Speech production is often described as a source-filter model. Sound originates with rapid oscillation of the vocal folds in the larynx, which serves as the acoustic source. The vocal tract, including oral and nasal cavities, functions as a linear acoustic filter. Vocal folds are located in the anterior neck, approximately posterior to the Adam’s apple. Figure 1.1 shows a coronal and sagittal view of the vocal tract and larynx, and a transverse view at the level of the abducted (open) vocal folds. The space between the vocal folds is the glottis. The portion of the airway superior to the glottis is the supraglottis, and inferior to the glottis is referred to as the subglottis.

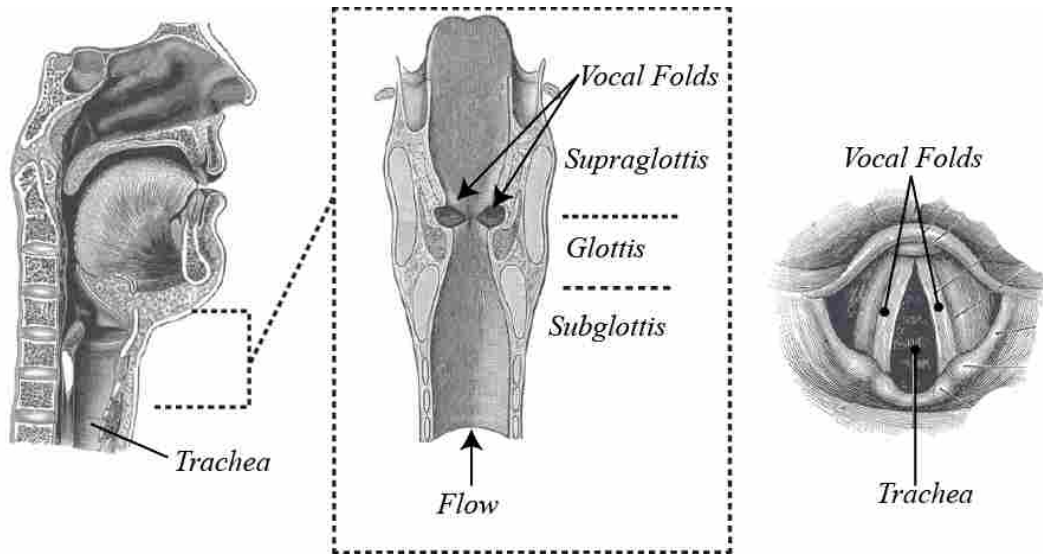


Figure 1.1: Saggital (left) and coronal (middle) views of the vocal tract and larynx, with a transverse view at the level of the glottis (right) (adapted from Gray's Anatomy of the Human Larynx [1]).

Pressure in the lungs from the diaphragm induces air flow through the trachea into the larynx, where the vocal folds are located. During phonation (voicing), the vocal folds are brought together medially, inhibiting the flow of air. As air pressure builds on the inferior side of the vocal folds, they are forced apart, creating a burst of air flow until they are brought back together by elastic forces within the larynx and decreased pressure caused by the increased air velocity, completing the glottal cycle. This periodic, self-oscillation occurs on the order of hundreds of times per second and creates pressure fluctuations that are filtered as they travel through the vocal tract to create the sound heard during phonation.

Geometry and material properties of vocal folds significantly affect vibration and are described here. Vocal folds are composed of multiple layers of tissue with vastly different material properties, as shown in Figure 1.2. The most medial layer is the epithelium, which is a very thin, relatively strong tissue which functions to protect vocal folds from high stress during vibration. It is composed of stratified squamous cells. The lamina propria consists of collagen and elastin fibers, and is often divided into superficial, intermediate, and deep layers. Due to the increasing density of collagen fibers, the lamina propria primarily increases in stiffness from extremely soft in the superficial layer (often compared to the consistency of gelatin) to more stiff in the deep layer.

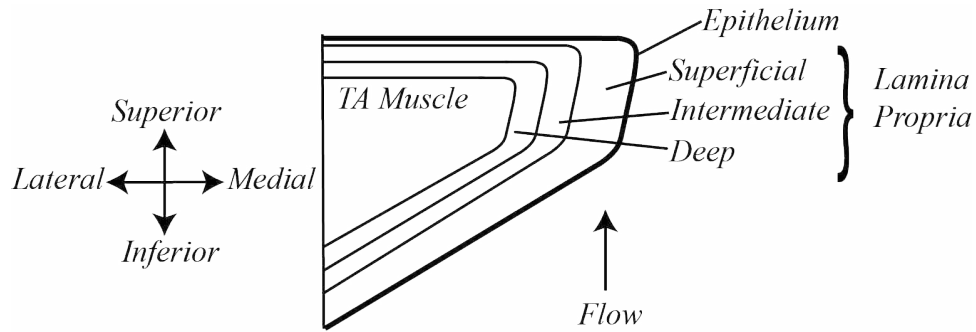


Figure 1.2: Diagram of a coronal view of the vocal folds depicting the various tissue layers.

The thyroarytenoid (TA) muscle is also stiff and contributes to the tensing and posturing of the vocal folds for speech.

1.1.2 Vocal Fold Research

Investigators of voice production have used a variety of approaches to study vocal folds and diagnose voice disorders. A brief introduction to each approach is given below to provide context for the work presented in this thesis.

Clinical Methods

Several techniques are employed in the diagnosis of voice problems and disorders, including electroglottography, stroboscopy, and high-speed endoscopy, as well as indirect methods including acoustic and aerodynamic techniques [4]. These techniques are also used in voice research to gain insight into vocal fold motion, and offer an incomparable degree of physiological reality relative to other approaches. However, limited space and access to the larynx severely limits the amount of information available from these tools. For example, direct imaging of the larynx is generally limited to a two-dimensional superior view.

Ex vivo/In vivo Studies

Experiments with excised human or animal larynges provide information about the effect of stimulation (e.g., muscle tension and air supply) on output conditions (e.g., dynamics, pressure, flow, etc.) as well as access to additional views of the larynx [5]. While these experiments offer

greater fidelity than synthetic or computational models, they lack physiological influences present in living conditions, such as complete neurological stimulation, vascularity, and mucosal secretion. *in vivo* animal studies can provide some physiological influences, but can only be done with animals, limiting the applicability to human vocal fold phonation. Access to larynx supply, vocal fold tissue durability, and difficulty in obtaining reproducible results from a single specimen are particular challenges in both *in vivo* and *ex vivo* experiments.

***In vitro* Studies**

Experiments with synthetic models offer greater control and reproducibility while also exhibiting more robustness than *ex vivo/in vivo* studies. Further, synthetic models eliminate the challenges associated with experiments in once live tissue, such as procurement and disposal. *In vitro* studies can also serve to validate numerical and mathematical studies. Kniesburges *et al.* have provided a review of models used for *in vitro* studies, including self-oscillating vocal fold models made of silicone [6].

Numerical and Mathematical Models

Numerical and mathematical models offer complete control over most factors influencing vibration (e.g., geometry, flow characteristics, material properties), leading to easily parameterized studies which can provide detailed information about the specific influence of each condition on vocal fold vibration. Additionally, pressure, velocity distributions, flow rates, etc., can be examined in great detail. They also complement *in vitro* studies, offering greater flexibility in changing parameters such as geometry. However, idealized material and geometrical properties and the difficulty in accounting for effects such as turbulence and acoustics limit the applicability of these studies [7].

1.2 Research Objectives

This thesis is concerned with further understanding the vibratory motion of the vocal folds during phonation. More specifically, it increases understanding of vocal fold geometry and me-

chanical properties. The research presented in this work addresses several limiting aspects of the approaches described above:

- *In vivo* imaging studies of human vocal folds are generally limited to two dimensions. This research contributes to the development of a stereo-endoscope, capable of recording three-dimensional motion.
- Excised canine larynges are difficult to obtain. This research explores the suitability of porcine larynges as a model by comparing porcine vocal fold geometry with human and canine geometry.
- Knowledge of vocal fold geometry is important for synthetic and computational modeling, but accurate knowledge of geometry is difficult to obtain. This research describes the level of distortion induced by freezing, an important step in obtaining information regarding vocal fold geometry.
- Knowledge of the material properties of the materials used in synthetic modeling is important for comparing between *in vitro* studies, as well as comparing to computational studies and excised data. However, no Poisson's ratio data for the silicone presently used in synthetic models is presently available. This research provides a strain-varying Poisson's ratio for silicone.

By addressing these specific limitations, this work seeks to build upon the valued work of others while furthering the work of future investigators in the voice community.

1.3 Thesis Overview

Characterization of Porcine Vocal Fold Geometry—Chapter 2

Five porcine larynges were scanned on a MicroCT scanner in a frozen state and at room temperature. The three dimensional geometry was imported into CAD programs, and relevant geometrical information was extracted using CAD tools and then further refined using a series of custom MATLAB codes. The porcine geometry was compared to geometry of human, canine, and commonly used synthetic model vocal folds. The effect of freezing on vocal fold geometry was

also examined by comparing frozen and room temperature geometry. A variety of computer vision techniques, implemented in MATLAB, were used to make the comparison.

Stereo-endoscope Validation–Chapter 3

The performance of a stereo-endoscope recording the superior surface of vibrating, synthetic vocal fold models was evaluated. Two DSLR cameras and the stereo-endoscope simultaneously recorded the surface of vibrating vocal fold models. The location of specific points marked on the surface were tracked through time. A Direct Linear Transformation (DLT) was used with the DSLR cameras to obtain three-dimensional coordinates that were used as reference data to evaluate the stereo-endoscope accuracy in each dimension.

Characterization of the Poisson’s Ratio of Silicone–Chapter 4

The Poisson’s ratio of silicone was measured as a function of strain. A range of silicone samples, aimed to match the stiffness of the various layers of the vocal folds, were subjected to a tensile load. Photos of the samples at varying strain levels were used to find the Poisson’s ratio as a function of strain for the material, as defined by Smith et al. [8]. This information can be used to more fully quantify the material properties of synthetic models and to thereby improve the accuracy of numerical models.

CHAPTER 2. QUANTIFICATION OF PORCINE VOCAL FOLD GEOMETRY¹

2.1 Introduction to Porcine Geometry Research

In terms of the underlying physics of voice production, the manner in which the human vocal folds respond to flow through the respiratory airway is primarily governed by the spatial distribution of tissue layers of differing stiffness. Thus, two of the most important characteristics of the vocal folds, from a mechanical point of view, are geometry and material properties. A few specific examples include the following: First, geometry is needed to describe mass distribution, which in turn plays an essential role in vocal fold vibratory characteristics. Second, the shapes of the vocal folds' medial surfaces define the shape of the glottal airway, directly influencing glottal air flow. Finally, studies of vocal fold tissue material properties depend on geometric details for interpretation since the spatial distribution of the stiffness of the various tissue layers is fundamentally a geometric description.

Several studies have highlighted and characterized connections between vocal fold geometry and voicing. For example, it has been shown that surgical geometric alterations can cause significant change in voice quality [9, 10], that pre-phonatory glottal shape influences vocal register and vibration [11], and that mathematical [12, 13] and computational [14, 15] models are highly dependent on initial and boundary conditions (the latter of which, in particular, are directly tied to model geometries). In addition, an understanding of vocal fold geometry is essential for developing and studying anatomically-accurate synthetic vocal fold replicas that exhibit realistic vibratory responses and that thus have the potential to advance voice production research [16–18].

Considering these factors, it is apparent that accurate geometrical descriptions of the human vocal folds are needed in order to develop a more complete understanding of the physics of voice production, in addition to the clear surgical and clinical implications. Indeed, knowledge of both

¹Accepted for publication: Stevens KA, Jette ME, Thibeault SA, Thomson SL. Quantification of porcine vocal fold geometry. *Journal of Voice*.

the geometry and material properties of vocal fold tissue is important for accurate model creation. A significant amount of research has been done to quantify the material properties of the various tissue layers [19–26]. A somewhat smaller, though important, body of work involving a variety of methods to obtain vocal fold geometric data also exists, including that which is summarized below.

Casting techniques have been used to create detailed three-dimensional (3D) models of the airway in the region of the vocal folds. Berry et al. [27] measured the medial surface geometry of canine larynges using a lost wax technique, and Sidlof et al. [28] provided quantitative descriptions of profiles along the medial surface for excised female human larynges using a plaster casting technique. These studies have provided important quantitative information about the geometry of the laryngeal lumen, although more data are needed to more completely quantify airway geometry for a broader population. The casting technique is limited to providing information about the shape of the medial surface and is not able to be used to quantify geometry of internal vocal fold tissue layers.

Medical imaging modalities, such as X-ray, magnetic resonance (MR), and computed tomography (CT), have yielded vocal fold dimension and shape data, but have not yet been fully exploited to provide complete 3D geometrical descriptions. Agarwal et al. [29] used laminagraphic tracings of the larynx to obtain dimensions of the vocal folds in one plane. Bakhshaei et al. [30] described the use of CT scans to create a generic standard model of the laryngeal framework and models of the airway, but no geometric descriptions were included (e.g., providing equations for surface profiles or making 3D computer models available). Others have used CT imaging to study conditions such as unilateral vocal fold immobility [31], paralysis [32], or post-surgical airflow characteristics [33]. However, rather than reporting full 3D geometric descriptions, instead they have provided basic geometric measures such as glottal area [33] or vocal fold length [31]. Pickup and Thomson [18] created an MRI-based model of the vocal folds, and provided an equation for the medial surface; however, this was only for one patient and no subglottic or supraglottic data were included. In general, CT imaging is well-suited for quantifying geometry of the airway, cartilage, or bulk tissue, but it is not useful for distinguishing between soft tissue layers. MR has potential for imaging soft tissue layers, but it has not yet been widely utilized for imaging vocal fold layer structure because of challenges with spatial resolution and tissue distinction.

Processing histological sections can yield information regarding the geometry of the various vocal fold layers, but the technique is limited to two dimensions and often induces significant tissue deformation. This approach appears to be the best option for generating layer geometric descriptions, but a more in-depth knowledge of the geometrical artifacts induced by histologic processing is required in order to rely on geometric data obtained by such methods. Traditional histologic sample processing induces high levels of deformation. Various researchers have shown that resection [34] and fixation in formalin [35] create significant artifacts in tissue geometry. Johnson et al. [34] measured the change in linear dimensions from in situ to post resection, fixation in 10% formalin, and slide preparation for tissue from canine labiobuccal mucosal margins and tongue. They reported a change in linear dimensions of 20 to 40% for tissue resection, 8 to 10% change after fixation, and a further shrinkage of 2 to 10% during slide preparation. Kimura et al. [35] compared the geometry in the mid-coronal plane of formalin-fixed and unfixed canine larynges and found that significant shrinkage was caused by the formalin fixation and histological processing. The most shrinkage was observed in the depth (medial-lateral direction) of the vocal fold body, with around 42% shrinkage induced by fixation in formalin and less than 17% induced from histological treatment. The depth of the vocal fold cover exhibited less shrinkage than the body, with less than 20% shrinkage from fixation and less than 20% shrinkage in cover from histological processing. Less shrinkage, on the order of 9% to 24% for fixation, was observed in the thickness (inferior-superior direction), demonstrating the influence of direction on shrinkage.

In order to avoid the excessive shrinkage caused by fixation, Eckel and Sittel [36] snap froze human larynges in liquid nitrogen and performed a morphometric analysis of the entire larynx based on horizontal sections. However, since freezing vocal fold tissue still induces some expansion, accurate quantification of the expansion induced by freezing the tissue would enable better approximation of actual vocal fold dimensions. Tayama et al. [37] began this process by measuring the linear shrinkage that occurred in coronal sections of canine larynges. They snap froze the larynges and then measured vocal fold depth and thickness as the larynges thawed in saline. They found that freezing the tissue induced small changes in vocal fold length ($< 2\%$), depth ($< 5\%$), and thickness (5 to 10%), and that thawed larynges returned to pre-freezing dimensions.

The first purpose of this chapter is to build on the work of Tayama [37] by quantifying the expansion of the tissue in three dimensions, providing needed insight into multi-dimensional effects of freezing on airway and vocal fold tissue geometry. It is intended as an intermediate step towards a more complete quantitative description of the geometry of the vocal folds, which would entail a three-dimensional description of all of the tissue layers. To obtain information regarding the internal tissue distribution found in the vocal folds, either medical imaging capable of differentiating between the layers or information obtained from histological processing is necessary. However, medical imaging has not yet been demonstrated for vocal fold tissue layer distinction. Though histological processing enables very high spatial resolution, since it induces deformation, quantification of the deformation is necessary to obtain accurate geometry from histology. Therefore, in this chapter, the three-dimensional-deformation induced by freezing tissue is quantified, which is one step towards quantifying the overall deformation that results from histological processing.

Animal modeling, particularly excised larynx studies, has been an important fixture in voice production research. Though canine vocal folds have been the primary animal model for the study of phonation, in some aspects of voice production, other animals may more closely model human vocal folds. For example, it is known that significant differences do exist between porcine and human vocal folds, such as the vibration of the superior folds in pigs, the incline of the porcine vocal folds in the inferior direction (anterior aspect is more inferior than posterior), as well as differences in phonation threshold pressure, subglottal pressure, sound pressure level, and Young's modulus [38]. Despite these differences, research has shown that for some situations porcine vocal folds serve as a suitable model, especially those focusing on variations in pitch [38–41]. Jiang et al. [41] observed that the thickness and structure of the vocal fold cover, overall vocal fold stiffness, fundamental frequency, and range of phonation of a the pig most closely resembles that of human when compared with those of a dog or deer. Alipour et al. [38] found that the frequency range and non-linear stress-strain patterns of pigs most closely resembled those of human when compared with dog, sheep, and cow. Garrett et al. [40] found that though the pig only has a two-layer lamina propria, in contrast with the three-layer lamina propria of humans, the composition of the superficial and deep layers are almost identical between the pig and human. Alipour et al. [38] hypothesized that this similarity is what contributes to the large dynamic range in both species.

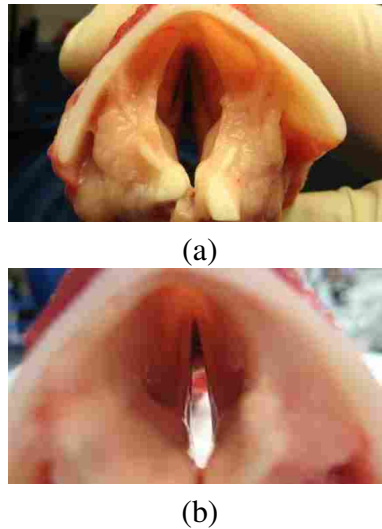


Figure 2.1: Photographs of porcine Larynges 1 (a) and 2 (b).

In addition, the availability of porcine larynges is significantly more convenient than canine vocal folds.

Notably, given the advantages of using porcine vocal folds as a model, quantitative descriptions of porcine vocal fold geometry beyond length, depth, and thickness have not been reported. In this chapter, additional aspects of porcine vocal fold geometry are quantified and compared to canine geometry from Berry et al. [27], human geometry from Sidlof et al. [28], and other geometries that have been used for vocal fold modeling purposes. Therefore, the second purpose of this work is to quantify geometric aspects of porcine vocal folds relative to human vocal folds.

2.2 Methods

Five fresh porcine larynges (Figure 2.1) were obtained from a local abattoir. Less than six hours from procurement, all five larynges were placed in specimen bags and imaged with a Siemens Inveon MicroPET/CT scanner using Inveon Acquisition Workplace (IAW) software for data acquisition at the University of Wisconsin-Madison. The folds were in the resting position and placed with the posterior larynx flat on the imaging bed of the scanner. After scanning, the larynges were then frozen with isopentane cooled over liquid nitrogen in order to prevent cracking and then rescanned. Voxel size for all scans was 0.1029 mm along each side, with the interrogation region containing 992 voxels in each dimension.

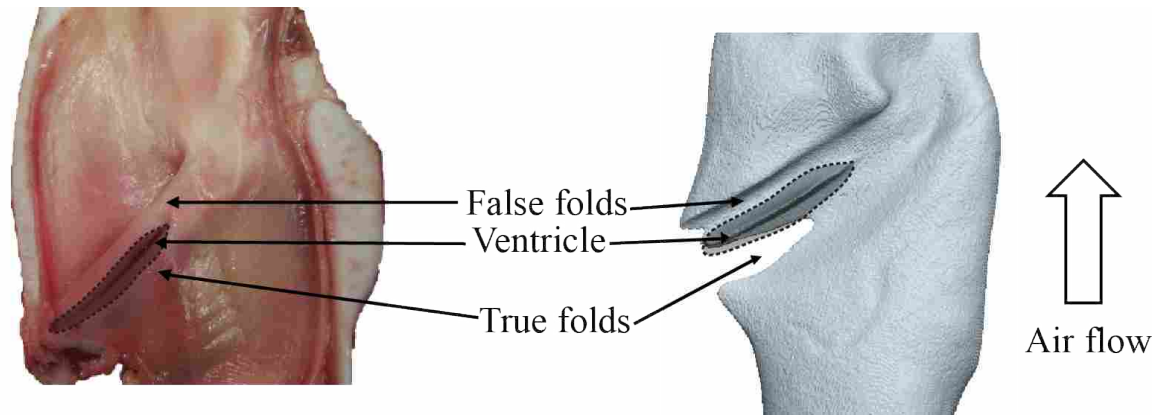


Figure 2.2: Sagittal view of porcine larynx (left) and computer rendering of segmented porcine laryngeal airway (right).

The scans were then analyzed using two different methods. First, medial surface profiles were extracted from the scans in order to compare porcine vocal fold geometry with other commonly used models. Second, tissue and airway volumes were analyzed to quantify the effects of freezing the tissue on the geometry. These are described in detail below.

2.2.1 Medial Surface Profile

The laryngeal airway was segmented using ITK-SNAP [42] for both scans (room temperature and frozen). A sagittal section of the larynx and a segmented airway is shown in Figure 2.2. The volumes were imported into computer-aided design (CAD) software packages (NX, Siemens PLM Software, and ProEngineer Wildfire 3.0), and a profile of the medial surface of the vocal folds was obtained by defining a reference plane perpendicular to both the sagittal plane and the vocal folds, placed halfway between the anterior commissure and the vocal process, as shown in Figure 2.3. Note the porcine vocal folds are inclined inferiorly at about a 40° angle to the horizontal, as described by Alipour et al. [39] and as can be seen in Figure 2.2, so this reference plane differs somewhat from the human coronal plane that is typically used to characterize human vocal fold medial surface profiles. The intersection data of the CAD geometry and the reference plane was exported and converted into a series of points in a plane using custom MATLAB codes, yielding medial surface profiles such as shown in Figure 2.3. Because the false or superior folds vibrate in pigs [39], superior fold geometry was also reported.

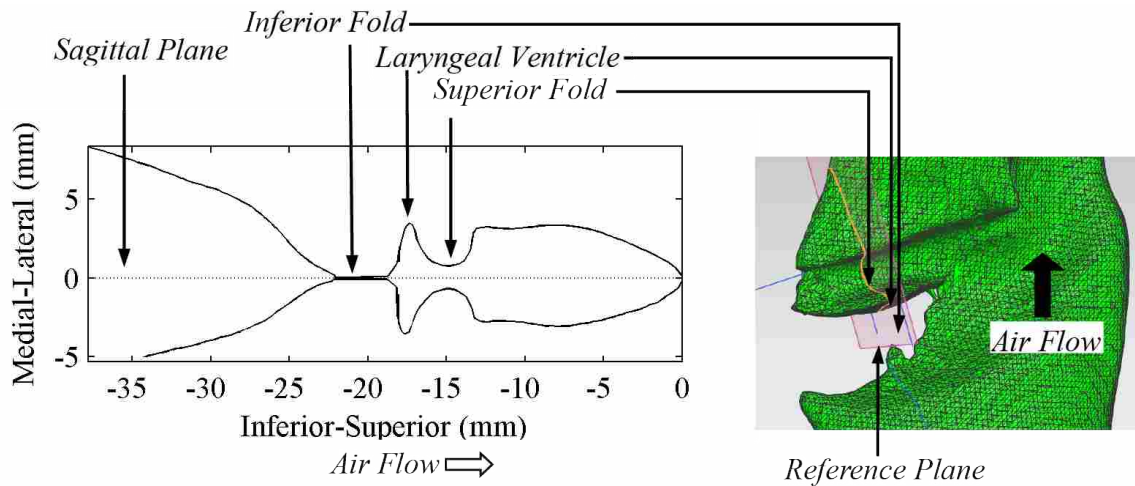


Figure 2.3: Medial surface profile (left) and airway CAD model rendering (right)

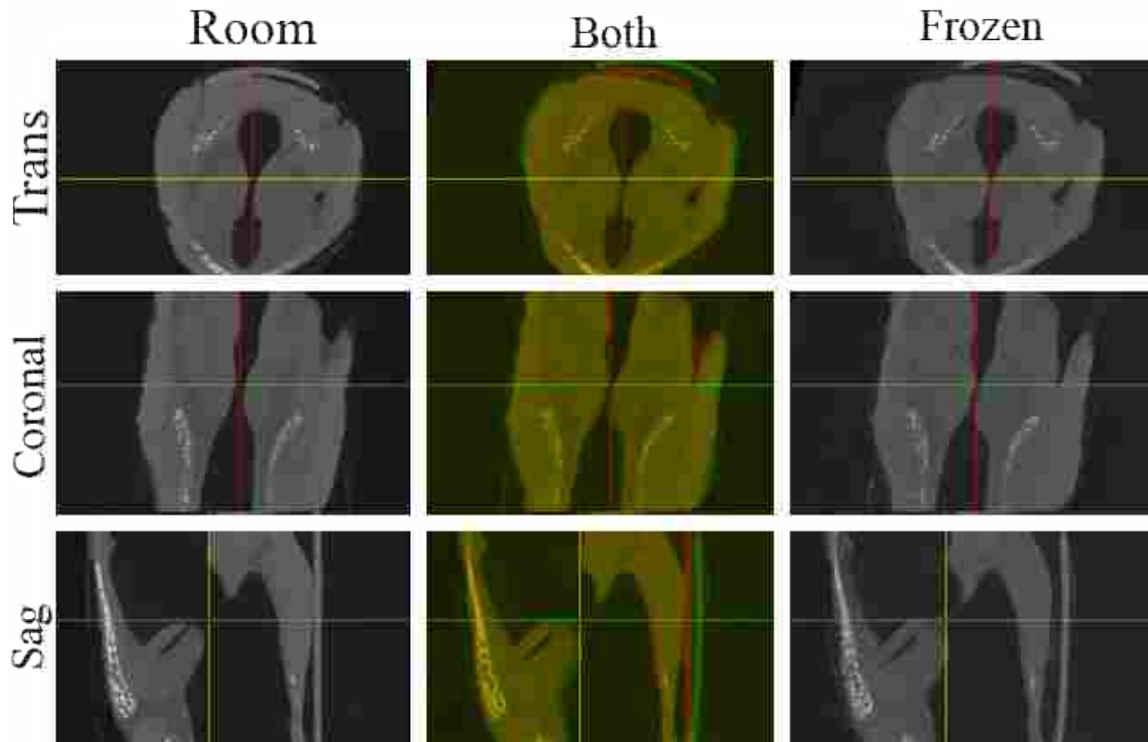


Figure 2.4: Manual registration of Larynx 1 at room temperature (left column) to Larynx 1 when frozen (right column). The center column includes the overlap in yellow, the frozen tissue in green, and the room temperature tissue in red. The three rows are the three orthogonal views of the larynx that roughly correspond to the transverse, coronal, and sagittal planes. The yellow, red, and green lines show the locations of the coronal, sagittal, and transverse planes, respectively.

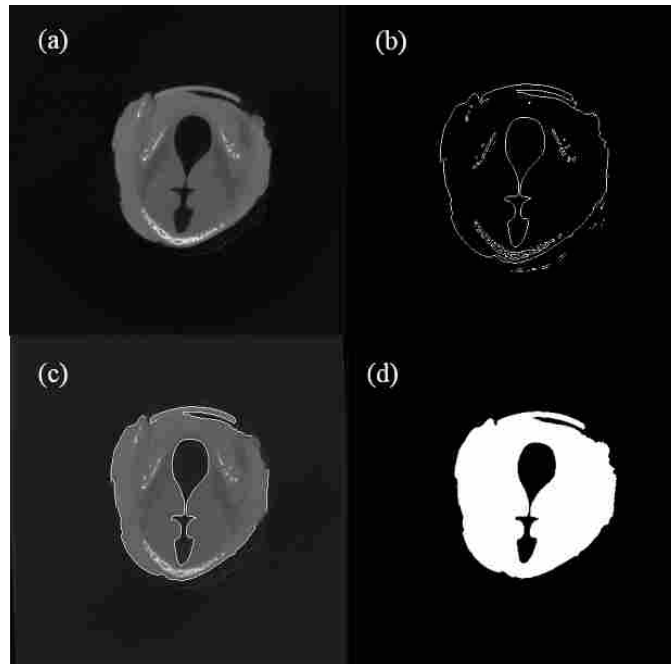


Figure 2.5: (a) Sample image from the transverse plane midway through the volume. These images were imported into MATLAB and the tissue or airway segmented, as follows. (b) The edges of the image were found using the method of Sobel. (c) The border of the tissue was found automatically. (d) The location of the edge of the tissue for all the images in that plane was used to select a threshold, which was applied to all the images, and used to calculate the area of the tissue in that slice. Further details regarding this procedure can be found in Appendix A.

2.2.2 Tissue and Airway Volume

The microCT scans were resampled in Analyze 8.1 (AnalyzeDirect, Inc.) such that the voxel size was 0.218 mm along each side. The room temperature and frozen volumes were manually registered to each other in Analyze using the Analyze 3-D Voxel Registration Tool. Since the tissue expanded unevenly with freezing, the volumes were manually registered such that there was an even amount of overlap across the larynx in all three directions as illustrated in Figure 2.4. The registered volumes were then exported as a series of images in the transverse, sagittal, and coronal planes. In MATLAB, the tissue was segmented from the surrounding air by thresholding each image and the area of the tissue in each cross section was then calculated, as illustrated in Figure 2.5.

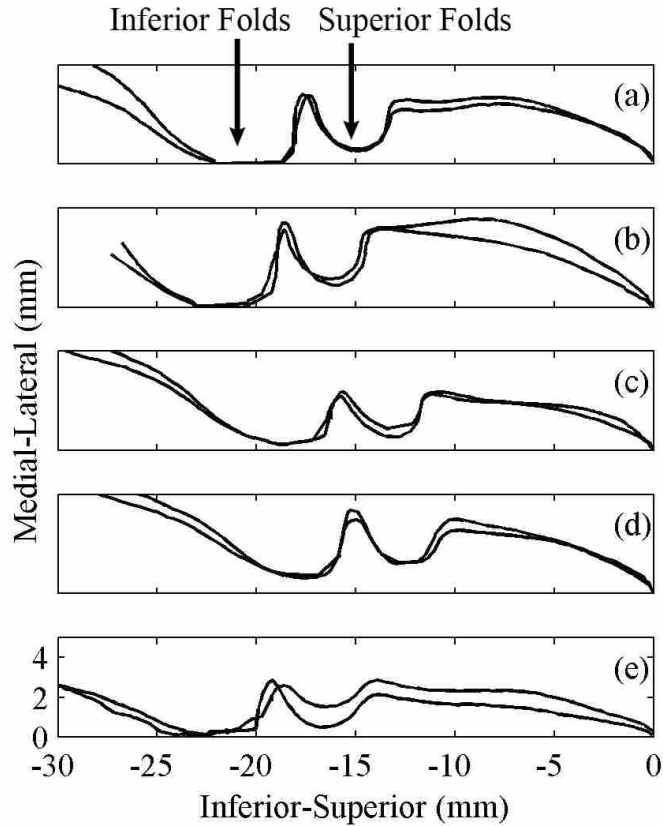


Figure 2.6: Left and right medial surface profiles of Larynges 1 through 5 (a through e, respectively) at room temperature.

2.3 Results and Discussion

2.3.1 Medial Surface Profile

The medial surface profile for each larynx was obtained and analyzed. Figure 2.6 contains the left and right sides of the profiles superimposed on each other for each of the five larynges at room temperature. The horizontal axis corresponds to the sagittal plane, from inferior to superior. The vertical axis denotes medial to lateral sense. A degree of natural asymmetry on the order of 10 to 30% between the left and right sides is manifest.

In order to account for size variations between samples, profiles from each larynx were normalized relative to a characteristic height (the average distance from the most superior point to the middle of the laryngeal ventricle) and a characteristic width (the average distance from the sagittal plane to the most lateral edge of the laryngeal ventricle), and are plotted in Figure 2.7a

for the room temperature larynges and Figure 2.8a for the frozen larynges. The average of the profiles with one standard deviation above and below the mean for the room temperature and frozen larynges, respectively, is shown in Figures 2.7b and 2.8b. It should be noted that the superior edges of the superior folds were located at several different positions, due to the fact that the length of the larynges was normalized relative to the distance from the most superior point to the middle of the laryngeal ventricle and the height of the superior folds varied between individual samples. Therefore, the slope of the superior edge of the superior fold is lost in the averaged profile. One interested in the shape of the superior folds can refer to the shape of the individual profiles. The normalized, average profile from the room temperature larynx could be used in vocal fold modeling. Since the shape is not able to be readily described by an equation, the data will be made available in the on-line data repository at www.larynxdata.org. The averaged profiles from the room temperature and frozen scans are shown together in Figure 2.9. No consistent variation in either the medial-lateral or inferior-superior direction is evident, other than the fact that the room temperature inferior folds were not all fully adducted in the mid-membranous plane. However, it is clear from the standard deviation plots in Figures 2.7 and 2.8 that distortion was introduced by freezing the tissue. Tayama et al. [37] measured canine vocal fold geometry in the mid-membranous coronal plane at various stages of thawing after quick freezing. They showed that the frozen tissue expands by about 5% and returns to within 1 to 2% of pre-frozen dimensions with thawing. This is comparable to the level of distortion seen in the present study.

The medial surface profiles from one of the room temperature larynges at locations other than the mid-membranous section are shown in Figure 2.10; profiles correspond to planes offset 2 mm anterior and posterior to the mid-membranous profile, as denoted in Figure 2.10a. Slight variation of the porcine vocal folds can be seen, but in general the shape of the vocal folds is similar in the anterior-posterior direction. Even though the vocal folds are inclined inferiorly, there is little variation in the direction of the length of the folds. The ability to neglect variation in the third dimension significantly simplifies modeling the shape of the vocal folds for computational and experimental studies.

The averaged profile obtained from the porcine folds at room temperature is compared with data obtained by other researchers and two models in Figure 2.11. Berry et al. [27] provided an equation for the surface profile of canine larynges, and the profile shown here corresponds to the

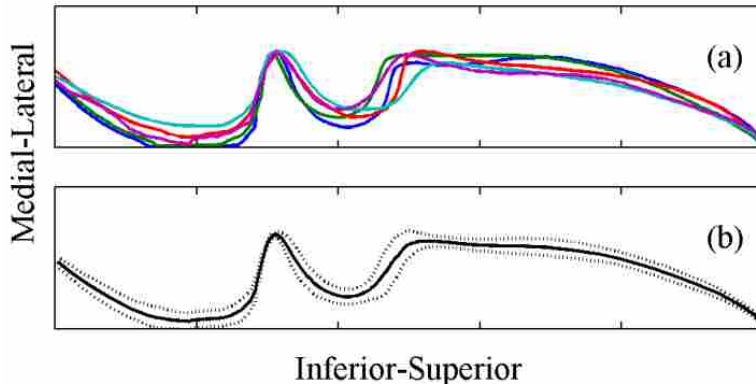


Figure 2.7: (a) Average of left and right medial surface profiles of the five room temperature larynges, normalized. (b) Mean profile (solid line) of all five larynges, including left and right sides, and envelope corresponding to plus and minus one standard deviation (dotted line).

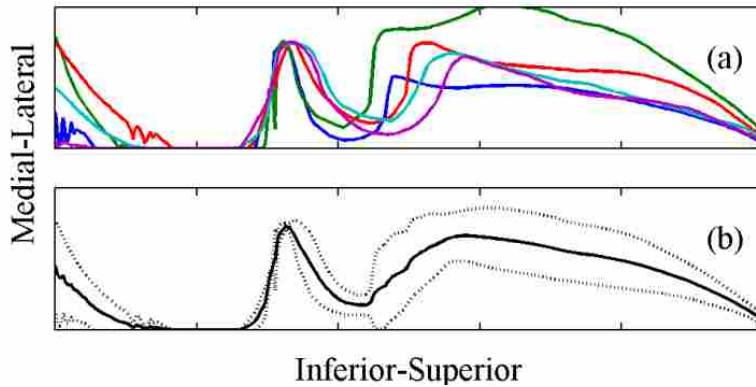


Figure 2.8: (a) Average of left and right medial surface profiles of the five frozen larynges, normalized. (b) Mean profile (solid line) of all five larynges, including left and right sides, and envelope corresponding to plus and minus one standard deviation (dotted line).

profile midway between the anterior and posterior sides of the surface. Sidlof et al. [28] reported data for two female human larynges, and the data shown here is the mid-membranous coronal section from their specimen labeled Larynx 8 when it was positioned for phonation at 148 Hz. The Agarwal et al. [29] data is for human false fold geometry obtained from coronal laryngeal laminagrams near the midmembranous location of the vocal fold length; the combined mean data for non-singers is shown. The shape of two models is also included: the commonly used M5 model from Scherer et al. [43] and a recent variation of the M5 model, used by Murray and Thomson [16], the primary variation being a larger inferior glottal radius. This latter model is referred to as the EPI model (due to the inclusion of an epithelial layer in the model).

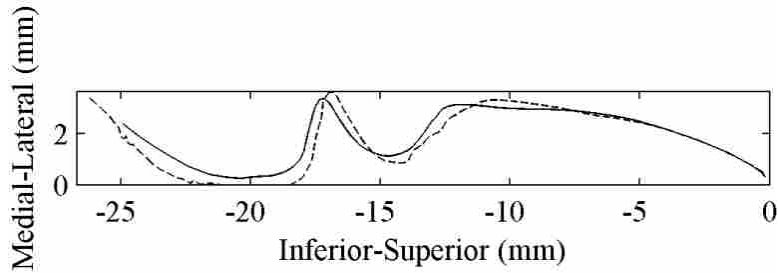


Figure 2.9: Mean frozen (dashed line) and room temperature (solid line) profiles

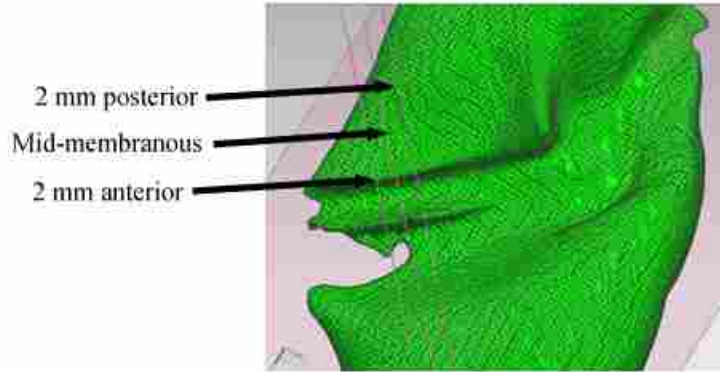
All models and vocal fold data are qualitatively similar, although some significant quantitative differences existed. The porcine mid-membranous profile from the present study is similar to other commonly used models of human vocal folds and the EPI profile is remarkably similar to the canine data of Berry et al [27]. Differences can be seen in the inlet and exit radii and the slopes of the inferior regions. The data of Sidlof et al. [28] exhibited notable differences compared with that of the others, possibly because the larynx was from a female and/or due to the folds having been postured for phonation prior to casting. More data are clearly needed in order to accurately quantify vocal fold geometry, including the vast individual variations that are known to occur.

2.3.2 Tissue and Airway Volume

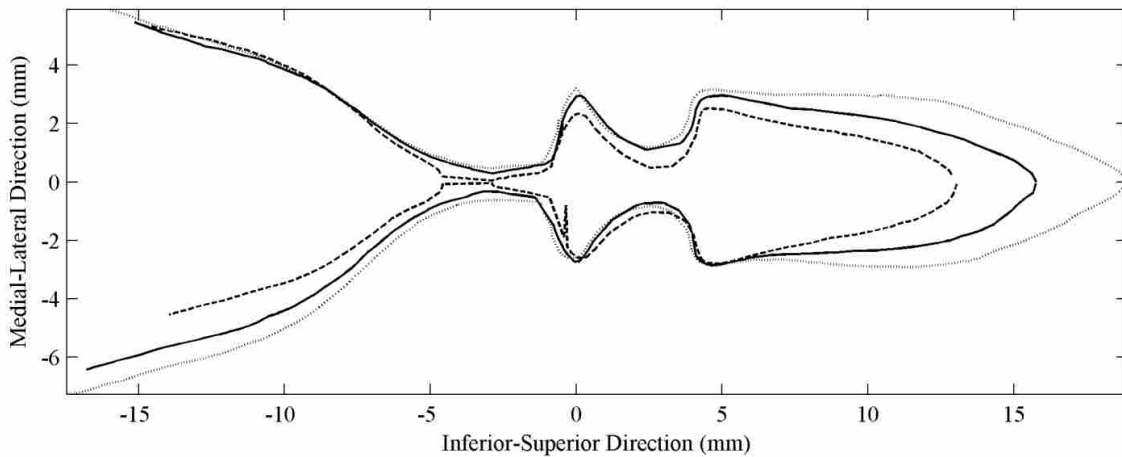
The changes in tissue and airway area in all three dimensions due to freezing are here reported and discussed. Plots of area at each transverse cross section along the inferior-superior direction for the room temperature and frozen larynges are shown in Figure 2.12. In this plane the tissue generally seems to expand when frozen.

The percent difference in area between the room temperature and frozen larynges at each cross section for each of the five larynges is shown in Figure 2.13. The difference is on the order of 5%, but none of the larynges exhibit a uniform level of expansion at each cross section.

The tissue volume was calculated by summing all of the areas from all of the cross sections, and the changes in volume between the room temperature and frozen larynges were calculated; see Table 2.1. All changes are positive, meaning that the tissue expanded, as would be expected. The average change in volume for all the larynges was 5%, but as shown in Figure 2.13, the expansion



(a)



(b)

Figure 2.10: (a) Location of planes anterior and posterior to the mid-membranous plane. (b) Profiles from three planes: 2 mm anterior (dashed lines), mid-membranous (solid lines), 2 mm posterior (dotted lines).

is not uniform throughout the volume. Therefore, one cannot predict a change of 5% in any given dimension, even if it lies in the transverse plane.

The area of each airway is shown in Figure 2.14. Note that the areas of the secretory laryngeal gland ducts or other sinus ducts were not considered. The distortion in the geometry caused by freezing is much less uniform. For example, in some places the airway constricted due to inward displacement of the tissue, while in other places the airway was enlarged.

Figures 2.15 and 2.16 show the area of the tissue at cross sections in the sagittal and coronal plane, respectively, along with the area of the airway. No consistent changes in area between room temperature and frozen specimens are observable. The tissue expansion in the transverse plane is

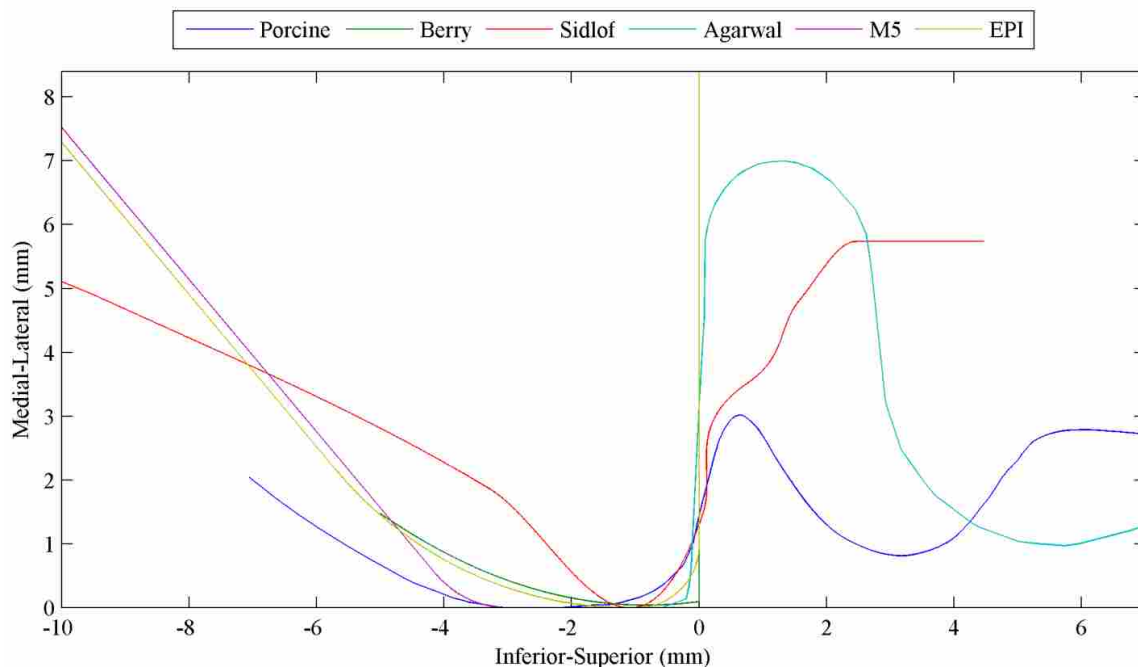


Figure 2.11: Medial surface profile from present study along with profiles from human and canine data as well as with models from other studies.

accompanied by non-uniform distortions in the other areas. Given the wide variety of tissue types present in the larynx, including cartilage, muscle, and soft tissue, each of which would likely tend to expand differently when frozen, such variation is not surprising. It is therefore evident that no generalizable description of the expected direction of distortion in a single coronal cross section can be given, which is unfortunate given that a single coronal cross section of the vocal folds provides the most detail regarding the distribution of the internal layers of the vocal fold tissue. However, the present data do provide some idea of the degree of distortion that could be expected. The data in Table 2.1 suggest that freezing can be expected to cause distortion on the order of five percent.

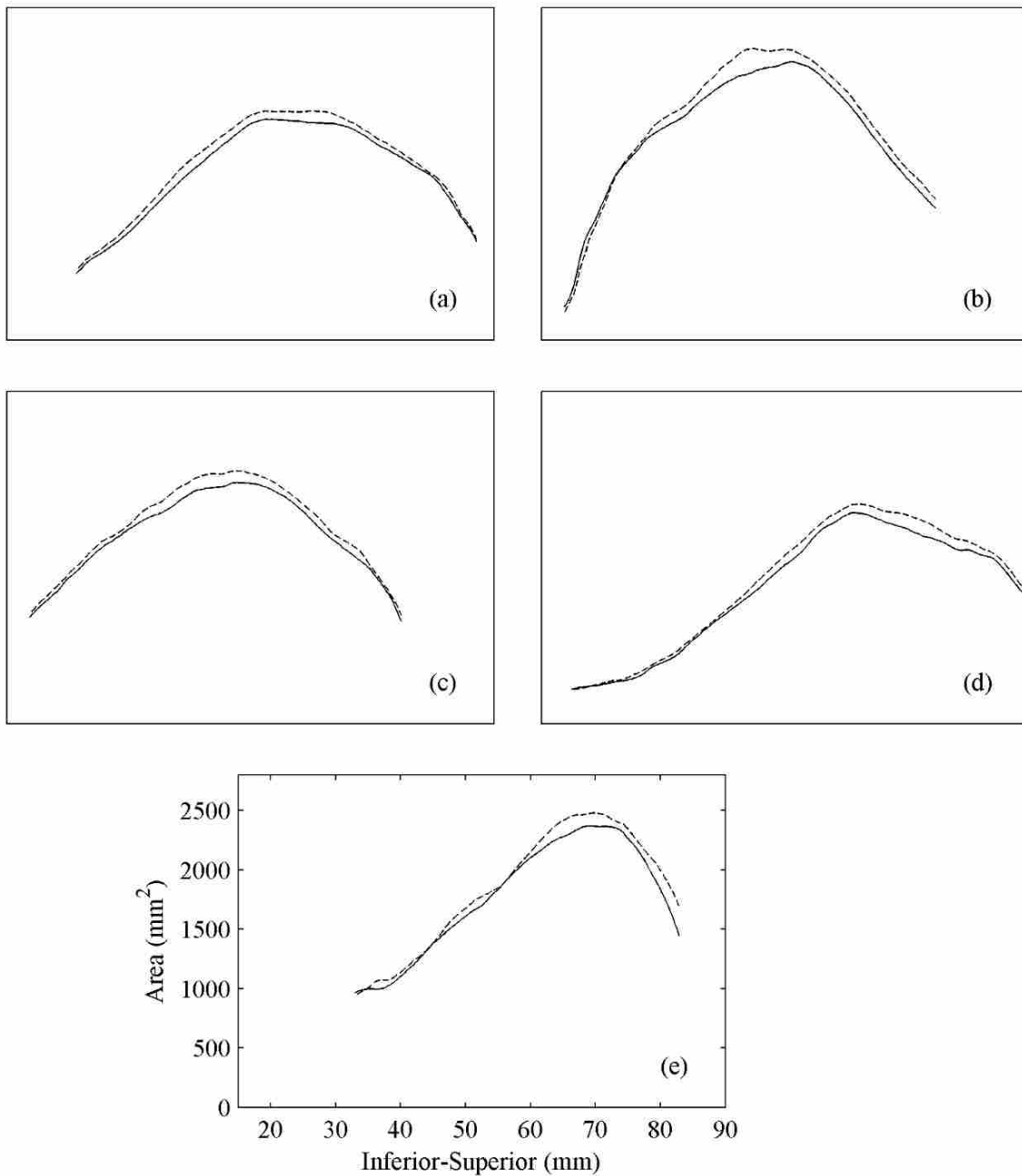


Figure 2.12: Area of the tissue in the transverse plane for each of the five larynges (a through e), including room temperature (solid lines) and frozen (dashed lines). The horizontal and vertical scales of plots (a) through (d) are the same as those denoted by the axis labels in plot (e).

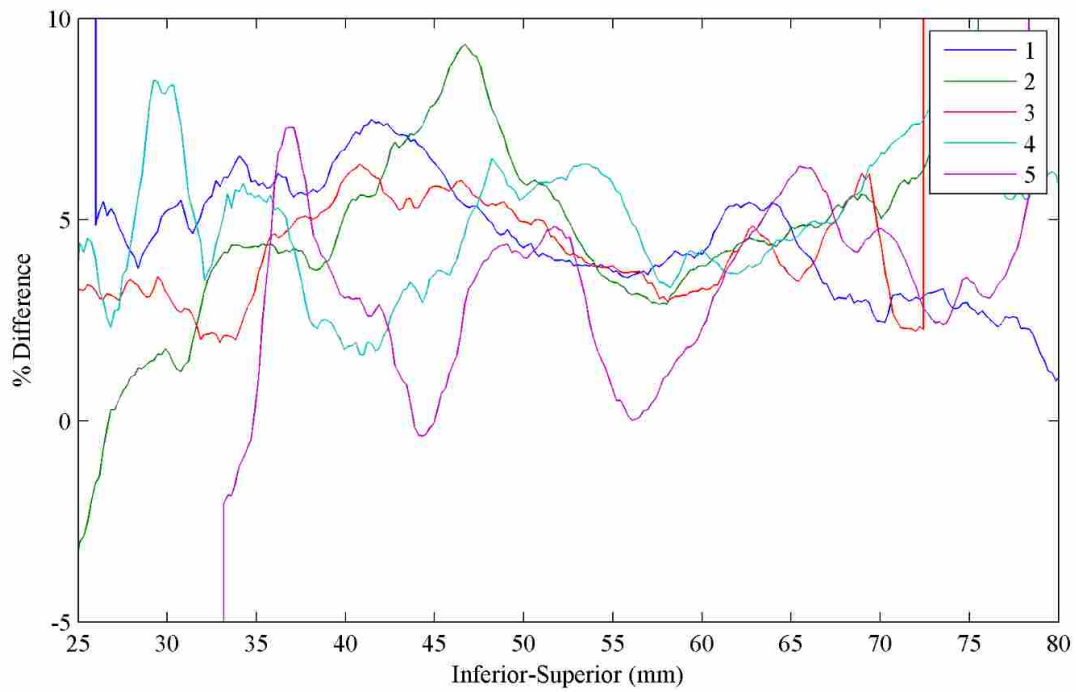


Figure 2.13: Normalized difference between room temperature and frozen larynges. The numbers 1-5 in the legend denote which of the five larynges.

Table 2.1: Percent change in volume between room temperature and frozen larynges.

Larynx	% Volume Change
1	4.6
2	5.1
3	4.4
4	4.5
5	3.0
Mean	4.5

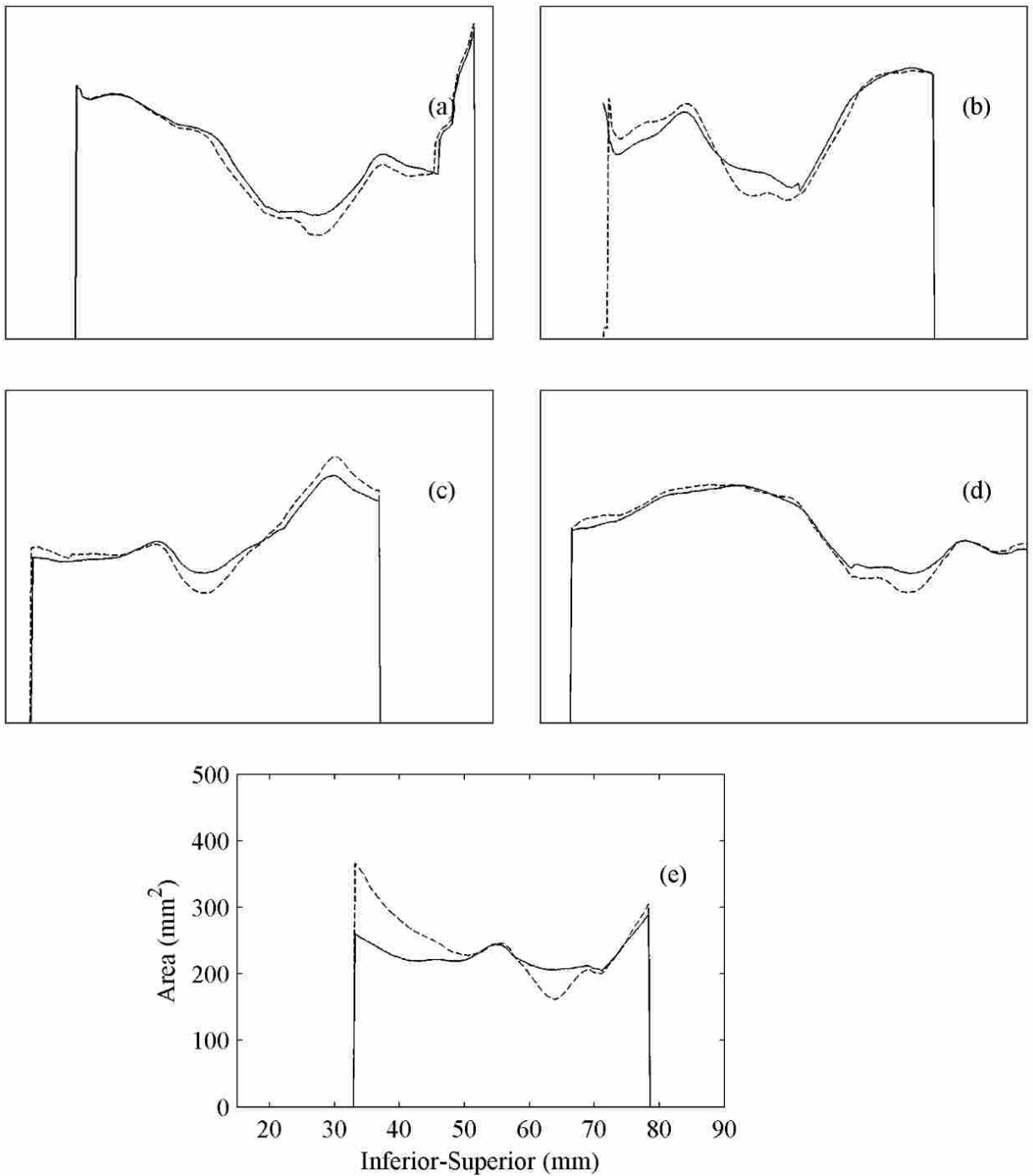


Figure 2.14: Cross-sectional area of the airway in the transverse plane for each of the five larynges (a through e) when the tissue was at room temperature (solid lines) and frozen (dashed lines).

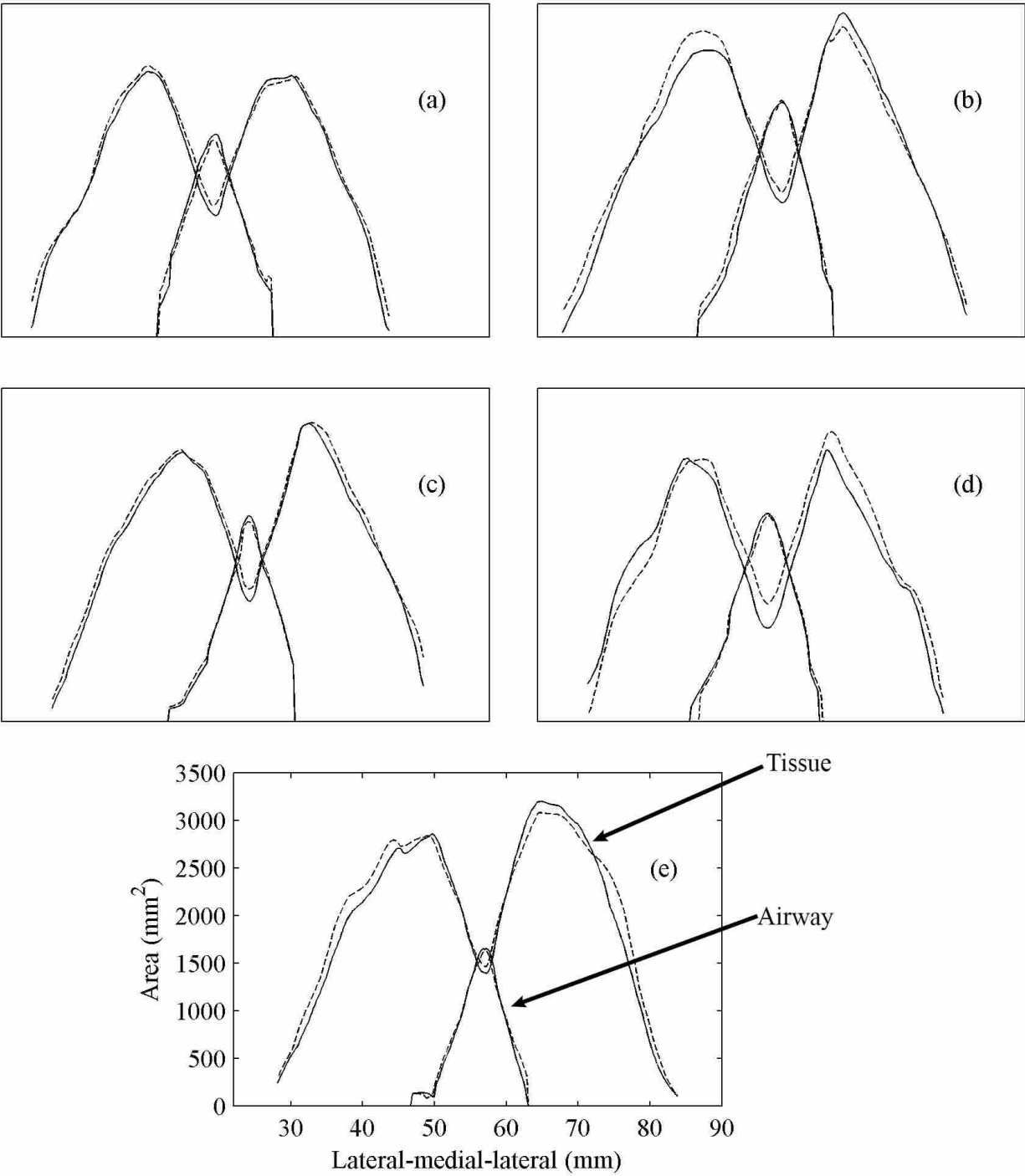


Figure 2.15: Tissue (larger) and airway (smaller) areas (e.g., as illustrated in plot e) in the sagittal plane for each of the five larynges (a through e), including room temperature (solid lines) and frozen (dashed lines)

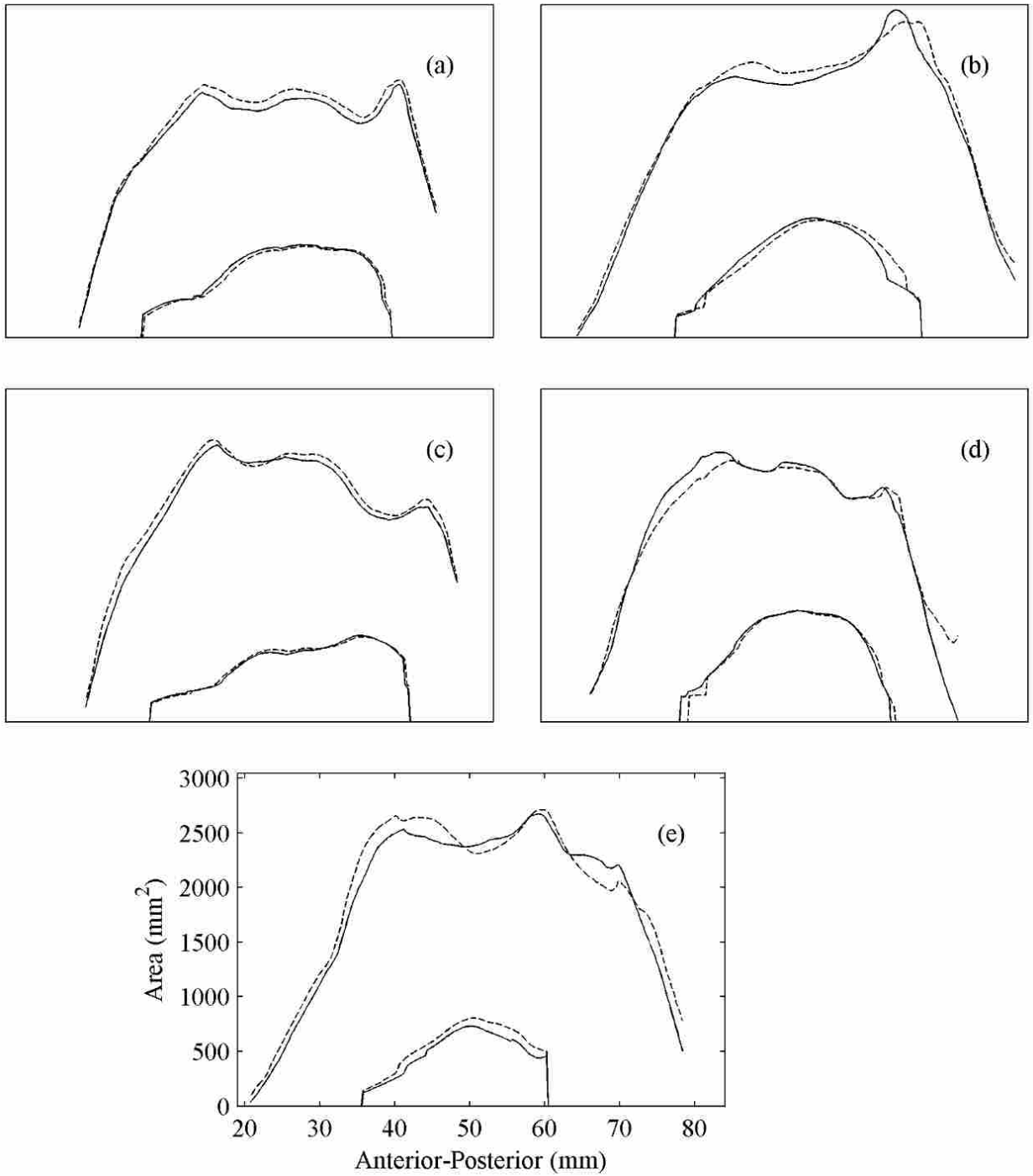


Figure 2.16: Tissue (larger) and airway (smaller) areas in the coronal plane for each of the five larynges (a through e), including room temperature (solid lines) and frozen (dashed lines).

2.4 Conclusion

Despite the fact that the geometry plays such an important role in phonation, relatively little quantitative information is available regarding the shape of the vocal folds, particularly that of the internal layers. This is due to the challenge of obtaining such information—the difficulty associated with obtaining sufficient spatial resolution in medical imaging and the distortion associated with histological processing. The present work addresses one part of the challenge of obtaining accurate geometrical information from histological processing by quantifying the overall three-dimensional effect of freezing, one step in a common method of fixation shown to have less distortion, on tissue geometry.

By comparing the medial surfaces at the mid-membranous section of the vocal folds, it is shown that freezing does cause a geometrical distortion of the tissue, but not in a consistent manner. Overall, the tissue experiences about a 5% change in volume in the entire larynx, but this does not appear to cause consistent or uniform shrinkage or expansion in any one direction in the region of the vocal folds.

The present work also quantifies the geometry of the medial surface of porcine vocal folds, and compares it with human and canine vocal folds and various synthetic model geometric data. The shape is similar to the other comparisons, though the porcine folds appear to be slightly thicker. It is difficult to compare exactly since the human data was from females; thus more human geometric data is needed for a more general comparison. Other obvious differences between porcine and human vocal folds exist, such as the underlying tissue structure and the 40° downward angle of the porcine folds, but otherwise it is evident that the geometry of porcine vocal folds is relatively similar to that of canine and human vocal folds.

As model development and geometrical quantification of the vocal folds becomes more sophisticated and extends into three dimensions, description of the vocal folds with drawings and simple splines becomes quite limiting. Therefore, to facilitate access by other researchers, all data described in this chapter will be made available at www.larynxdata.org, including the original microCT scans and the curve describing the medial surface of the porcine vocal folds.

Though traditional medical imaging does not yet allow the differentiation of tissue layers, the technology is continually improving and the future development of such capabilities seems likely. The method outlined in this chapter to go from medical images to a 2D profile describing

the geometry could be applied to obtain descriptions of the different tissue layers on excised human larynges, and even to *in vivo* humans, once this level of detail becomes technologically feasible. One obvious limitation of histological processing is that the excised tissue cannot be postured for voicing in precisely the same way as that which occurs *in vivo*. Even when the vocal folds are adducted via sutures or other means for phonation, the nerves controlling muscles activation are not stimulated, thus geometry obtained in this manner is still only a limited representation of *in vivo* conditions. The ability to posture the folds for speech is a major advantage of *in vivo* medical imaging and will certainly be used in the future to obtain more accurate geometrical models of the vocal folds. However, until that time, the methods described in this chapter can contribute to an overall estimate of the accuracy of future geometries derived from histological section processing.

CHAPTER 3. VALIDATING A STEREO-ENDOSCOPE WITH A SYNTHETIC VOCAL FOLD MODEL

3.1 Introduction

Stroboscopy and high-speed video endoscopy have been used for decades in both research and clinical settings to gain insight into the dynamics of the vocal folds and to diagnose voice disorders [44–46]. However, such tools are limited to providing information regarding glottal movement in the transverse plane. Yet, information outside of that plane would be of benefit to both clinicians and researchers, allowing the observation of left-right vertical asymmetry, measurement of absolute lengths, and providing further insight into the motion of the mucosal wave, which has been shown to be very important in phonation [47].

Various techniques have been employed to obtain three-dimensional information of the vocal fold dynamics. Three-dimensional measurement of vocal fold vibration has been obtained by observation of the medial surface of the vocal folds in a hemi-larynx setup, where half of the larynx is removed to allow visual access to the medial surface. Such a technique is limited to excised larynges, or at best *in vivo* canine [48–50]. Excised larynges lack the muscle activities present in *in vivo* vocal folds, and the material properties of the tissue begins to change upon excision. Although valuable insight into the motion of the mucosal wave is gained, this technique cannot completely capture the dynamics of real human vocal fold vibration. Moreover, these studies have attached small markers to the vocal folds in order to track their movement, which is not possible with human subjects.

Non-invasive techniques with high-frame-rate ultrasound [51] or stroboscopic x-ray laminagraphy [52] have allowed the observation of bulk motion; however, these techniques are not sufficiently sensitive to capture detailed vocal fold surface movements. Other researchers have used various optical techniques to augment traditional endoscopy systems to obtain three-dimensional information [53–57]. Luegmair et al. used a high-speed camera and a laser projection system to

reconstruct the surface of the vocal folds during vibration [57]. However, the technique has not been applied to a real subject *in vivo* because a tedious and complicated calibration procedure is needed every time the laser grid system is utilized. Furthermore, laser systems provide only point-wise information and cannot trace the medial edge when it falls between the laser dots, rendering the capture of surface dynamics, such as tracing the moving location of the medial edge, impossible. Optical coherence tomography (OCT) has also been utilized to reconstruct *in vivo* vocal fold motion at a point [58]. The advantage of OCT methods is that it can penetrate into the vocal fold tissue approximately 2 mm and show the movement of both the epithelium and underlying tissue. Although triggered OCT has been successful in reconstructing three-dimensional displacement of excised calf larynges, it requires scanning of the vocal fold tissue over many periodic cycles, and artifacts can be introduced if the signal is not perfectly periodic [59].

The present work focuses on a stereo-endoscopic observation of the vocal folds as an alternative approach to non-invasive three-dimensional measurements [60–62]. Stereo-endoscopy provides two views of the larynx from different angles, enabling three-dimensional viewing of the laryngeal structure. With its compact design, the stereo-endoscope has a relatively low impact on articulators and controlling musculature of the vocal folds, thus enabling a natural vocalization. Once the camera is calibrated, it does not require further adjustment between other measurement devices, e.g., alignment of lasers or unique calibration for each subject. To recover three-dimensional dynamics from the stereo-endoscopic measurement of vocal folds *in vivo*, Tokuda et al. [53] and Sommer et al. [63] used stereo-matching, a widely developed technique in computer vision research. They extracted quantitative information regarding vocal fold movement in three dimensions. However, their work has not yet been extensively validated.

The purpose of the work described here was to evaluate the accuracy of the stereo-endoscopy technique by comparing it with a standard stereo vision technique using two high-resolution cameras. In a controlled environment, three-dimensional motion of a synthetic vocal fold model was simultaneously recorded by the two imaging techniques and compared to evaluate the efficacy of the stereo-endoscopy system.

Synthetic vocal fold models are ideally suited for the task of evaluating the stereo-endoscope. Their motion is similar to the vibration of *in vivo* vocal folds, but their location outside of the larynx provided a more controlled environment and permitted the use of a secondary imaging system

to evaluate the accuracy of the stereo-endoscope. Without limitations on the size or location of cameras, the secondary imaging system was able to have a much higher resolution and wider baseline, making it more accurate than the stereo-endoscope. Because of this, the secondary imaging system was considered “ground truth” in evaluating the stereo-endoscope. The accuracy of the stereo-endoscope is heavily influenced by the distance from the imaging surface, but patient comfort often precludes ideal placement of the endoscope during an exam. However, synthetic models allow for fixed and ideal placement of the endoscope. Additionally, models allow a controlled lighting system without the spectral reflections commonly encountered in an *in vivo* environment. Correspondence between left and right camera views is a major challenge encountered in using stereo-vision inside the larynx. With models, tracking markers can be used, eliminating this challenge, as well as allowing precise comparison of points between the stereo-endoscope system and the evaluating system. With many of the challenges of stereo-vision eliminated by the use of synthetic models, the accuracy of the stereo-endoscope was more easily evaluated, thus providing voice researchers a tool to study the three-dimensional vibration of the vocal folds.

3.2 Method

3.2.1 Experimental Setup

A synthetic vocal fold model was created, based on the geometry of Drechsel and Thomson [64] and following the methods of Murray and Thomson [16, 65]. Rather than using a commercial release agent to prevent the silicone models from sticking to the rubber molds, a thin, precisely sized sheet of plastic was adhered to the mold with vacuum grease to prevent the silicone from adhering to the mold. A grid of black dots was painted onto the surface in order to match points between recording systems, as shown in Figure 3.1. The model vibrated at an onset pressure of 0.74 kPa with a frequency of 108 Hz, comparable to that of Drechsel and Thomson [64]. The frequency is comparable to that of human phonation [66], though the onset pressure is slightly higher than human threshold pressure, as is common with many synthetic models [67]. The length of the duct upstream from the vocal folds was 70 cm. Further details regarding the experimental setup can be found in [68]. The vibrating surface of the model was recorded simultaneously with the stereo-endoscope (Nagashima Medical Instrument Corporation) and two digital single lens reflex



Figure 3.1: Grid of dots painted on the model to reduce error due to the correspondence problem.

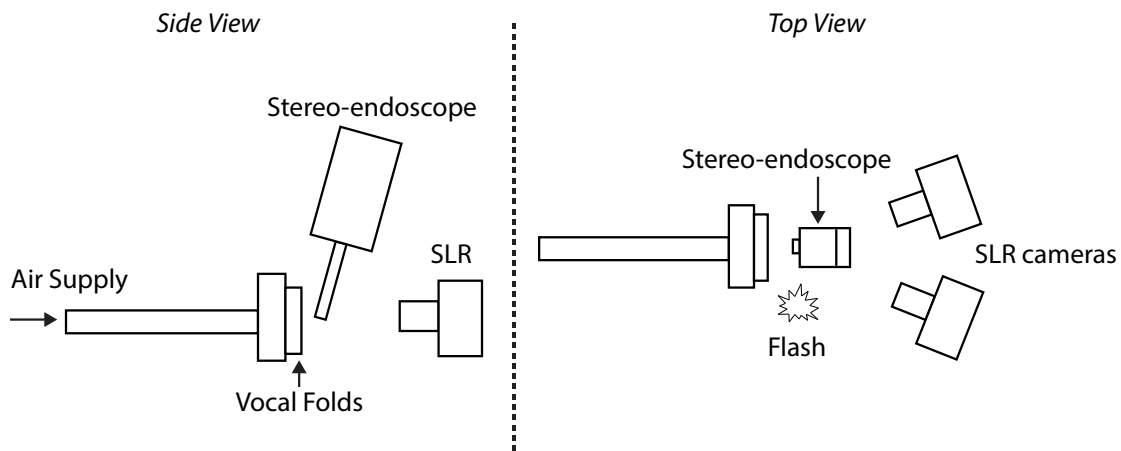


Figure 3.2: The surface of the vocal folds was recorded simultaneously with two DSLR cameras and the stereo-endoscope.

(DSLR) cameras (Nikon D5100) as shown in Figure 3.2. The two DSLR cameras with 105 mm lenses (AF Micro Nikkor) comprised the secondary imaging system used to evaluate the stereo-endoscope. The centers of the two DSLR cameras were approximately 20 cm apart and 60° apart. The stereo-endoscope included two independent, ordinary, rigid optical systems with diameters of 4 mm, a fiber-optic light guide, an optical connector, a light source, and a camera [53, 63]. The tips of the optical systems house objective lenses with prisms designed for 70° oblique-angled view, with a field angle of 40° . The distance between the optical axes of the tips was 6 mm. The stereo-

endoscope was attached to a CCTV lens with a focal length of 50 mm, which was connected to the high-speed digital camera (Photron FASTCAM 1024PCI). The high-speed recordings were made at 10,000 frames per second with a shutter speed of 1/1,000,000 second. A flash (Bolt VX-760N) was used to synchronize timing between the two imaging systems. While the stereo-endoscope was recording, the shutter on both DSLR cameras was opened, the flash was fired at 1/8 power, and the shutters were closed. The camera settings and ambient lighting were adjusted such that only the light from the flash was visible in both systems. As described in Chapter 1, the vocal folds vibrate in a periodic manner, creating a glottal cycle. The phase of the glottal cycle is referred to as ϕ , where the zero phase corresponds to maximum glottal pressure. Because the vibration is periodic, images of vibrating folds were captured over the course of hundreds of glottal cycles. As long as the phase is known, images from different glottal cycles can be compared as if they came from the same cycle, negating the need for high speed imaging in the secondary imaging system. However, even though the vibration was periodic, it should be noted that the images from the two imaging systems were both recorded at the same instant due to the fact that the model was illuminated by the flash.

3.2.2 Stereo-endoscopy System

A representative stereo-endoscopic image from the high-speed camera is shown in Figure 3.3. Additional details regarding the three-dimensional reconstruction of coordinates from this system can be found in [53]. Pixel-based coordinates x and y are defined, with the origin located at the top left of the stereo image. With respect to a feature point indicated by diamonds in both left and right images, the main parameters needed to recover its three-dimensional location are their vertical distance, D_V , and horizontal distances, D_L and D_R , from the corresponding center of the optical field (circles). Locations of the center of the optical field, (x_{LC}, y_{LC}) and (x_{RC}, y_{RC}) , in left and right images are determined through calibration, and they remain constant for a given optical set-up. Note that lowercase coordinates x and y correspond to pixel locations in the image, whereas uppercase coordinates X , Y , and Z represent physical dimensions relative to the endoscope probe head as defined in Figure 3.4. X and Y are in the plane normal to the stereo-endoscope and Z is orthogonal to that plane. In terms of physiological coordinates, X is in the medial-lateral direction, Y is in the anterior-posterior direction, and Z is in the inferior-superior direction. Given the pixel

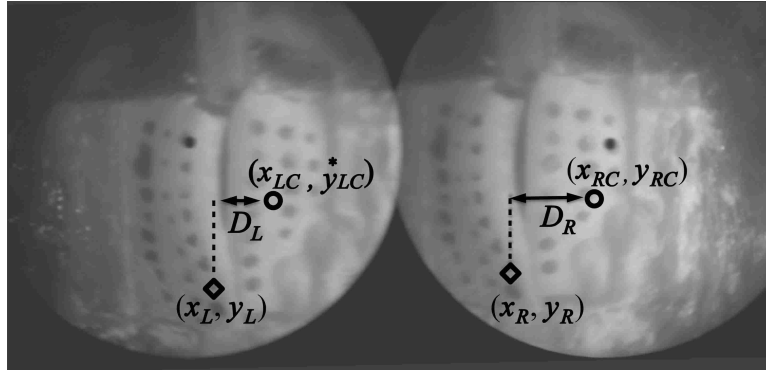


Figure 3.3: Representative image from the stereo-endoscope.

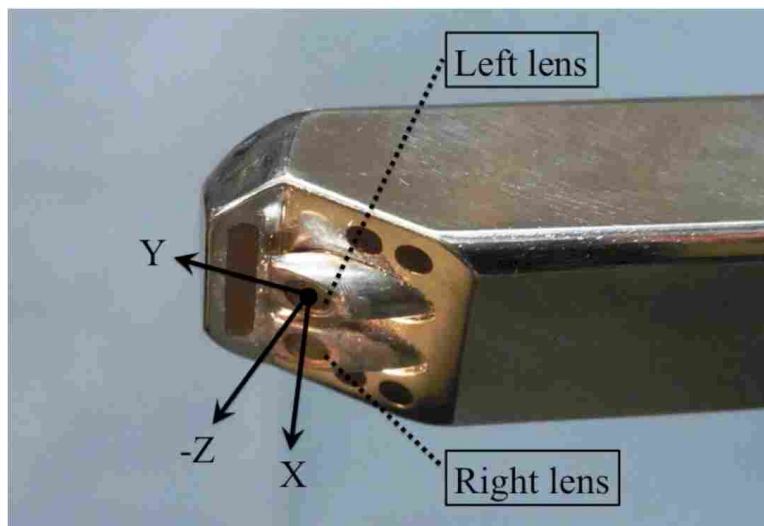


Figure 3.4: Photograph of the stereo-endoscope

coordinates of the feature in the left and right images, (x_L, y_L) and (x_R, y_R) , the quantities D_L , D_R , and D_V are given by:

$$D_L = x_L - x_{LC}, \quad (3.1)$$

$$D_R = x_R - x_{RC}, \quad (3.2)$$

$$D_V = y_{LC} - 0.5(y_L + y_R). \quad (3.3)$$

The left-right disparity is defined as $\Delta = D_L - D_R$. The Cartesian coordinates of the feature point are then estimated as:

$$\tilde{Z} = 1/(k_1\Delta + k_2), \quad (3.4)$$

$$\tilde{X} = k_3\tilde{Z}D_L + k_4, \quad (3.5)$$

$$\tilde{Y} = k_5\tilde{Z}D_V + k_6, \quad (3.6)$$

where the constants k_1 through k_6 are calibrated for a given optical set-up. Equation 3.1 is, in general, valid for an idealistic situation. To account for optical distortion inherent in the lens and camera systems, a modified version of Equation 3.4 having higher-order polynomials is used, as follows [53]:

$$\tilde{Z} = 1/(k_1[\Delta + c_1D_L^2 + c_2D_L + c_3D_V^2 + c_4D_V] + k_2). \quad (3.7)$$

The calibration constants $\{k_i\}$ and $\{c_i\}$ were optimized for the current camera setup with the following procedure. Images on a Cartesian graph paper with a grid of 5 mm by 5 mm were captured at distances ranging from $Z = 32$ mm to $Z = 52$ mm. At each distance, the X -, Y -, and Z -coordinates of the grid points with known dimensions D_L , D_R , and D_V were obtained. The calibration constants were then determined by the least squares method to best fit the data. The average calibration errors were $\langle |X - \tilde{X}| \rangle = 0.11$ mm, $\langle |Y - \tilde{Y}| \rangle = 0.088$ mm, and $\langle |Z - \tilde{Z}| \rangle = 0.18$ mm in X -axis, Y -axis, and Z -axis, respectively, where $\langle \cdot \rangle$ denotes averaging over all calibration points. The average calibration error in all three dimensions was $\langle \sqrt{(X - \tilde{X})^2 + (Y - \tilde{Y})^2 + (Z - \tilde{Z})^2} \rangle = 0.27$ mm.

3.2.3 DSLR System

The image space for the DSLR system was calibrated using a direct linear transformation (DLT), as described by Abdel-Aziz and Karara [69]. A checkerboard pattern (10 cm by 10 cm, Fig. 3.5) was placed in view of both cameras, a picture was taken, and then the target was moved forward manually 2 mm. The target was adhered to a block of aluminum, which was machined to have square edges, and moved along a grid of Cartesian graph paper to ensure movement only

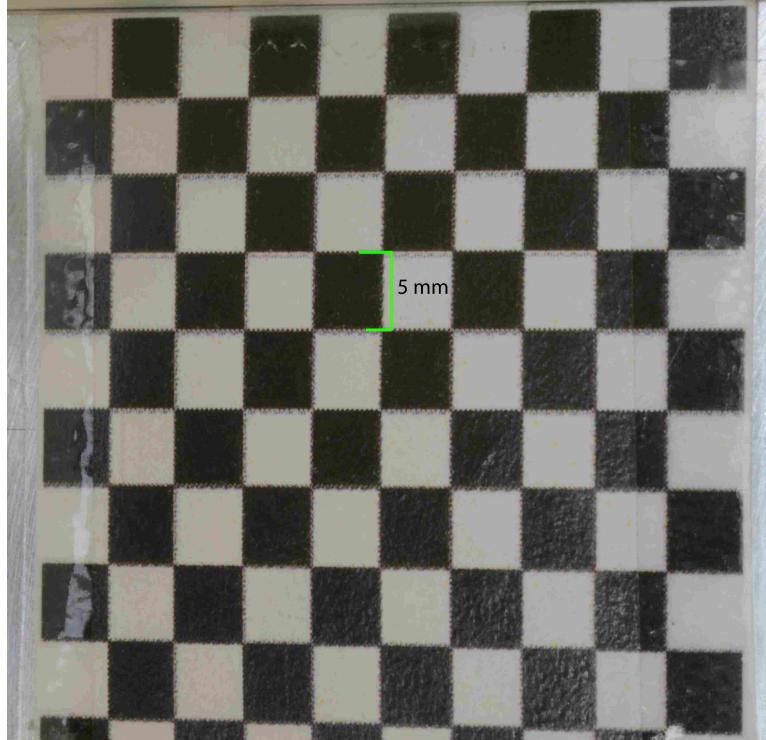


Figure 3.5: Sample calibration image

in the inferior-superior direction. This was repeated six times. The centers of the white portions of the checkerboard were found automatically using connected components, a common computer vision technique. Appendix B further describes this procedure and contains the MATLAB code used in the calibration.

Twenty-eight points were visible in the field of view of each image for a total of 196 calibration points. Calibration points from the left and right camera images are denoted as (u_L, v_L) and (u_R, v_R) , respectively, whereas the corresponding three-dimensional location is represented by (X, Y, Z) . For all calibration points, the Moore-Penrose pseudo-inverse method determined the DLT, which maps (u_L, v_L) and (u_R, v_R) to $(\hat{X}, \hat{Y}, \hat{Z})$, the three-dimensional coordinates reconstructed from the DSLR system. In order to ascertain the accuracy of the transform, the average error was calculated for all calibration points. The programs were written and executed in MATLAB (MathWorks, Inc., V7.13 (R2011b)). Further details can be found in Appendix B. The obtained errors were $\langle |X - \hat{X}| \rangle = 0.031$ mm, $\langle |Y - \hat{Y}| \rangle = 0.016$ mm, $\langle |Z - \hat{Z}| \rangle = 0.073$ mm, and $\langle \sqrt{(X - \hat{X})^2 + (Y - \hat{Y})^2 + (Z - \hat{Z})^2} \rangle = 0.0808$ mm. This error represents the average amount that the actual location of the calibration points differed from their location calculated using the transform.

mation. The error could come from inaccuracies in selecting the location of the calibration points in the image, as well as from any error caused by not precisely moving the calibration target. Because the magnitude of the error in each direction was small, the calibration was deemed sufficient to provide a ground-truth estimation of the location of any point within the calibration volume in three-dimensions.

3.2.4 Application to Synthetic Vocal Fold Model

For each point in time, three-dimensional locations of the markers on the synthetic vocal fold model were estimated as follows. In the stereo-endoscopy system, the locations of the corresponding points were selected manually. To improve the accuracy, cross-correlation was computed between the left and right images when selecting the corresponding points. A *Gaussian* 3-point curve was fitted to the surface to achieve sub-pixel accuracy. The estimated three-dimensional locations of the points were then calculated by Eqs. 3.1-3.7. In the DSLR system, the locations of the markers were automatically selected using connected components, as summarized below.

- Each image was converted to black and white with a user defined threshold and inverted.
- A filter was applied so that only the marker points remained in the image.
- The points were sorted such that they were always in the same order.
- MATLAB's connected components algorithm was used to find the location and centroid of each marker point.

The three-dimensional locations of the marked points were then computed using the DLT algorithm. Appendix B contains additional details regarding the conversion to three-dimensional points for both systems.

3.3 Results and Discussion

The coordinate spaces of the two systems, i.e., DSLR cameras and stereo-endoscope, were shifted to the same origin and rotated to match the anatomical directions. Example images of the SLRs and stereo-endoscope, along with the three-dimensional locations of the marker points from

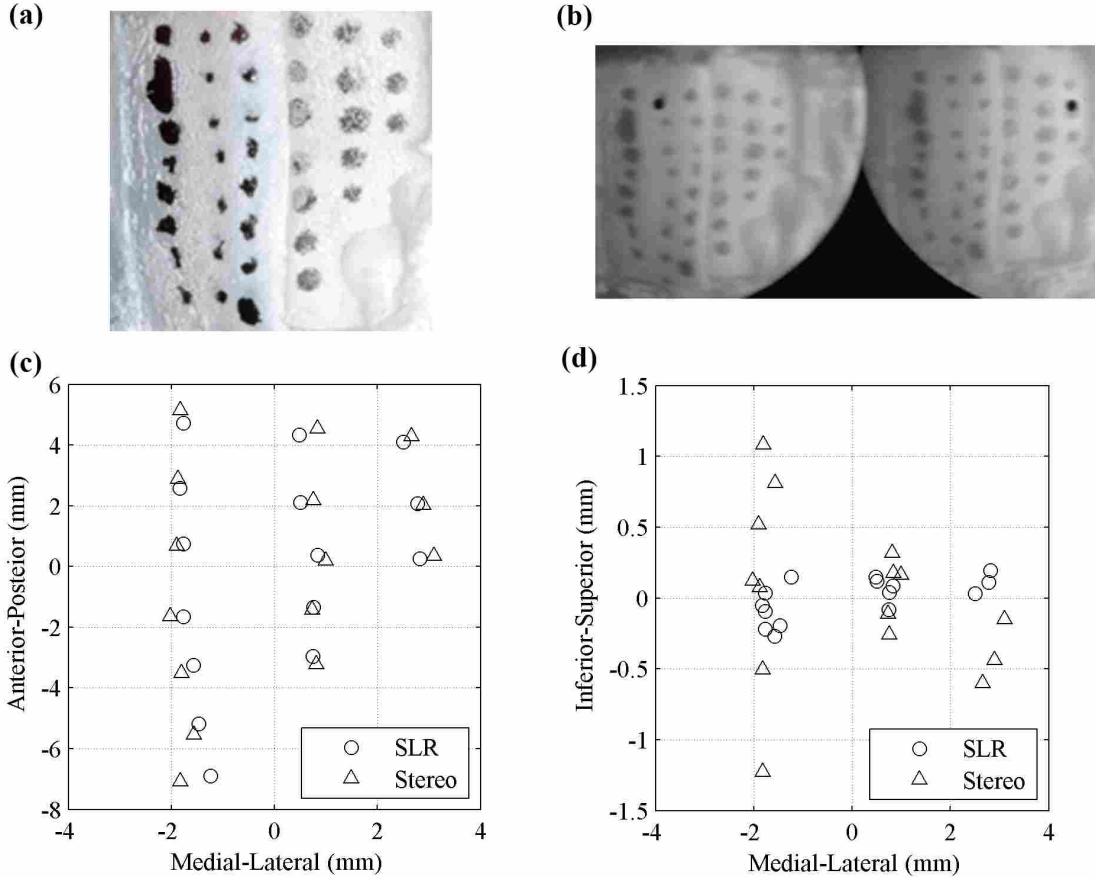


Figure 3.6: Image of the vocal fold model surface at $\phi = 92.6^\circ$, taken with the (a) DSLR and (b) stereo-endoscope and the (c,d) locations of the markers plotted in three-dimensions. Note the different scales on the vertical axes.

the right vocal fold are plotted in Fig. 3.6. The locations of the marker points on the right side of the vocal folds are plotted in Figure 3.7. The three-dimensional locations of the points were compared using Eqs. 3.8-3.10 for the error in each direction and Eq. 3.11 (for the total error):

$$\varepsilon_X = \frac{1}{N} \sum_{i=1}^N |\tilde{X}_i - \hat{X}_i| \quad (3.8)$$

$$\varepsilon_Y = \frac{1}{N} \sum_{i=1}^N |\tilde{Y}_i - \hat{Y}_i| \quad (3.9)$$

$$\varepsilon_Z = \frac{1}{N} \sum_{i=1}^N |\tilde{Z}_i - \hat{Z}_i| \quad (3.10)$$

$$\varepsilon_{XYZ} = \frac{1}{N} \sum_{i=1}^N \sqrt{(\tilde{X} - \hat{X})^2 + (\tilde{Y} - \hat{Y})^2 + (\tilde{Z} - \hat{Z})^2} \quad (3.11)$$

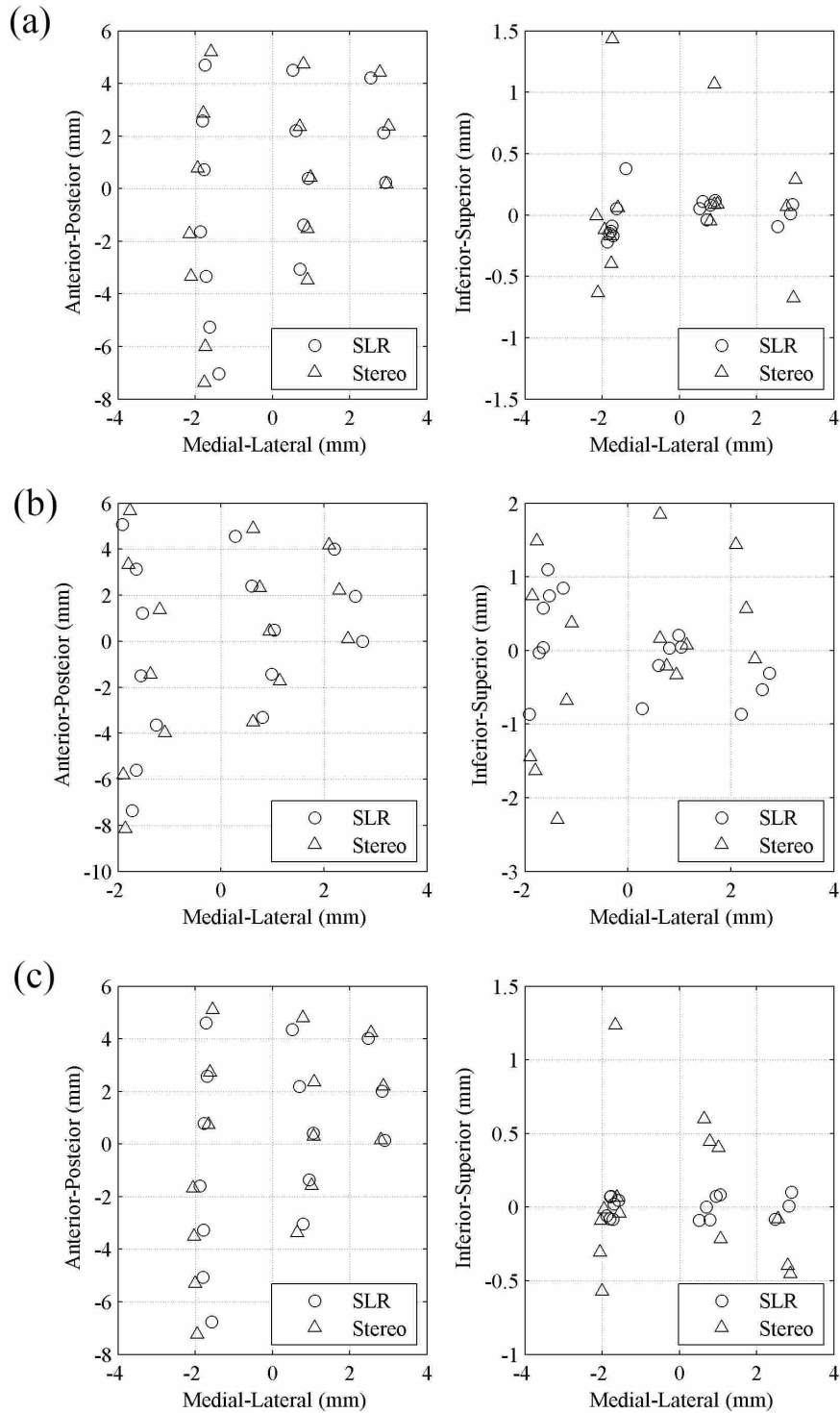


Figure 3.7: Locations of the marker points on the right vocal fold when (a) $\phi = 0^\circ$, (b) $\phi = 43.5^\circ$, and (c) $\phi = 73.1^\circ$. Note the different scales on the vertical axes.

Here, $(\tilde{X}_i, \tilde{Y}_i, \tilde{Z}_i)$ and $(\hat{X}_i, \hat{Y}_i, \hat{Z}_i)$ represent three dimensional location of the i -th marker estimated by stereo-endoscopy and DSLR camera systems, respectively. The errors are summarized in Table 3.1 for four different images, taken at varying points in the periodic cycle of the vocal fold model vibration.

Because of the differences in lighting between the left and right sides of the model, the two sides were analyzed and summarized separately. The average error in the X - and Y -directions is relatively small compared to the error in the Z -direction. This is not surprising, given the small baseline between the cameras on the stereo-endoscope (6 mm). Such a small baseline is necessary for the endoscope to be small enough for use *in vivo*. The error in the Z -direction also agrees quite well with that calculated by Sommer et al. [63], in which average errors of 2.1, 2.0, and 0.74 mm were reported for the three different subjects tested. The relatively low error in the measurement of absolute distances in the transverse (X, Y) -plane suggests that a potential application for the stereo-endoscope would be to obtain measurements of distances in that plane, such as glottal length, width, and area. It is impossible to measure absolute distances with a single camera without a mechanism for calibrating, such as placing a ruler or object of known size in the same plane as the measurements. However, the placement of such an object is very difficult *in vivo*. Even though the absolute error in the inferior-superior (Z) direction is greater than in the transverse plane, stereo-endoscopy may still provide useful information regarding the relative heights of features along the surface of the vocal folds, as well as the surface movement during one cycle of the vocal fold oscillation (e.g., [63]).

3.4 Conclusion

This chapter utilized a synthetic vocal fold model as an idealistic object to evaluate the accuracy of stereo-endoscopy to make three-dimensional measurements. The results were compared with those of two DSLR cameras, used as a secondary imaging system to provide a more accurate geometrical description of the object. Reconstruction of the three-dimensional coordinates using stereo-vision techniques is fraught with potential sources of error, including error from calibration and correspondence. Typically, finding good correspondence between left and right images is the most challenging aspect of three-dimensional imaging. This problem is compounded inside the glottis; poor lighting, smooth, continuous, and monochromatic tissue surface, non-distinct edges,

Table 3.1: Averaged estimation of error in each direction (mm) measured by distance between the stereo-endoscope and DSLR cameras. The phase of the glottal cycle is indicated by ϕ , where the zero phase corresponds to maximum glottal pressure.

Data #	side	Medial-lateral (X)	Anterior-posterior (Y)	Inferior-superior (Z)	Total	# points
$\phi = 0^\circ$	right	0.175 mm	0.232 mm	0.443 mm	0.599 mm	$N = 15$
	left	0.287 mm	0.280 mm	0.574 mm	0.778 mm	$N = 24$
$\phi = 43.5^\circ$	right	0.199 mm	0.254 mm	1.266 mm	1.366 mm	$N = 15$
	left	0.252 mm	0.347 mm	0.331 mm	0.575 mm	$N = 8$
$\phi = 73.1^\circ$	right	0.161 mm	0.229 mm	0.375 mm	0.530 mm	$N = 15$
	left	0.312 mm	0.245 mm	0.320 mm	0.583 mm	$N = 8$
$\phi = 92.6^\circ$	right	0.188 mm	0.183 mm	0.527 mm	0.636 mm	$N = 15$
	left	0.325 mm	0.284 mm	0.618 mm	0.815 mm	$N = 21$
Mean		0.237 mm	0.257 mm	0.557 mm	0.735 mm	

spectral reflections from the mucosa, etc. make finding good correspondence especially challenging. Sommer et al. [63] have focused on this part of the problem, significantly improving the accuracy of the results. The present study focused on the triangulation aspect of the process, evaluating the error that comes mainly from hardware limitation and calibration of the stereo-endoscope. In order to significantly reduce any error due to correspondence between images, specific points were marked on the surface of the vocal folds; this work focused on finding the location of those specific points, rather than on a dense reconstruction of the entire surface.

In addition to reducing the correspondence challenge (matching locations in left and right images) imaging synthetic models provided the ideal imaging situation. The images were recorded an optimal distance from the stereo-endoscope to the surface of the vocal folds. In an *in vivo* environment, optimal placement of the endoscope is rarely possible, and the challenges with correspondence are still present. Such ideal conditions should be kept in mind when considering the present results. By focusing on the hardware capability (i.e., sensitivity of the stereo lens and resolution of the high speed camera) as the sources of error in the process of three-dimensional reconstruction, the present results highlight the potential and limitations of the current stereo-endoscope, suggesting directions for future development and areas in which the current endoscope may be of utility. The fine precision of the absolute distance measurements in the transverse plane is of particular note. Though further development might be needed before highly accurate information regarding

the dynamics of the mucosal wave or of small features on the surface of the vocal folds can be extracted from the present stereo-endoscope, stereo-endoscopy still could potentially be used to measure absolute distances *in vivo*.

Imagawa et al. [70] applied stereo-endoscopy to estimate absolute glottal dimensions such as the glottal width, length and area functions. For vocalization of a female subject (fundamental frequency of 230 Hz), the maximal glottal length, width, and area were estimated as 7 mm, 2 mm, and 11 mm², respectively. The averaged errors of 0.257 mm and 0.237 mm obtained in the present study for the anterior-posterior and medial-lateral directions imply that the estimation errors would be less than 4%, 12%, and 8% for the glottal length, width, and area, respectively. Therefore, the present technique is of practical use for measuring the vocal fold dimension in the transverse plane. Since the vertical range of the vocal fold movement is reported to be around 1.76 to 2.75 mm [49, 57], the averaged error of 0.557 mm in the inferior-superior direction is greater than 30%. Not only is the stereo-endoscope is less sensitive in the inferior-superior direction, but the scale of movement in that direction is smaller, making it insufficient to provide a reliable estimate on the vertical dynamics with the present hardware. Further hardware improvements, such as higher image resolution, brighter luminosity, and less optical distortion, would improve the accuracy of the stereo-endoscope. Until such advancements in hardware are realized, future work could include examining the spatial distribution of error, studying the error in absolute position relative to the error in tracking a point's displacement over time, or further theoretical study of the stereo-endoscope algorithms to identify the largest sources of error.

CHAPTER 4. POISSON'S RATIO OF SILICONE

4.1 Introduction

As described in Chapter 1, voice research entails a harmony of clinical, computational, experimental, *in vivo* and *ex vitro* studies. One area in particular where cooperation is vital is between the use of physical models and computational models, i.e., using physical models to validate computational models and exploring how changing model parameters affects output [15, 18]. Knowledge of model material properties is crucial for this comparison. Recently, self-oscillating silicone models have become popular for vocal fold experimental work [6, 16, 17, 64, 65, 71, 72]. A significant quantity of data regarding Young's modulus [18, 65, 68, 72, 73] and limited data concerning the rheological properties of silicone [16] is available, but to the author's knowledge no information on Poisson's ratio specific to the silicone used in vocal fold modeling has been published. Poisson's ratio is an essential parameter for computational modeling; therefore, data regarding Poisson's ratio would be beneficial. This chapter provides data from which a function for strain-varying Poisson's ratio is obtained for silicone frequently used in vocal fold experimental studies that will enable computational modeling.

In addition to being used in computational model development, Titze [74] advocated that Young's modulus, rheological properties, and Poisson's ratio are all important parameters that govern vocal fold oscillation. Knowing how the Poisson's ratio of silicone compares with that of excised tissue could lead to the development of better models.

Traditional engineering materials have a Poisson's ratio of 0.25 to 0.5. A perfectly incompressible material would have a Poisson's ratio of 0.5. For an isotropic material, it is theoretically possible to have ratios from -1.0 to 0.5. However, recently, many new materials, including many biomaterials [75], have been found to have directional ratios much higher than 0.5 due to their anisotropic nature. It is well known that the Poisson's ratio of rubber and rubber-like materials is close to 0.5 [76, 77]. However, Smith et al. [8] showed that for highly deformable materials at

large strains, Poisson's ratio varies with strain; therefore, a strain-varying Poisson's ratio model is needed, and traditional calculation methods may not be applicable. This chapter includes a brief review of relevant material property definitions followed by a discussion of several methods of calculating Poisson's ratio. The Poisson's ratio of silicone is calculated using each method and compared, and a strain-varying function for the Poisson's ratio of silicone is provided. The nomenclature used by Smith [10] was adopted throughout the chapter.

4.2 Poisson's Ratio Estimates

Poisson's ratio, in general terms, is a ratio of the transverse to axial strain in a material. Any definition of Poisson's ratio depends on the definition of strain used. Strain is a relative measure of deformation, i.e., it is the displacement of regions of a body normalized by a reference length. Which definition of strain is used depends on the level of deformation induced in the material, as described below.

Logarithmic, true, natural, or Hencky strain, ϵ^{log} , of a specimen subjected to stress induced deformation is a measure of the specimen's extension relative to its *instantaneous* length. Incremental strain is defined as

$$\delta\epsilon = \frac{\delta l_i}{l_i}, \quad (4.1)$$

where δl_i is the change in length of a given line element to its current or instantaneous length, l_i . The logarithmic strain is the integral of infinitely small incremental strains [78],

$$\epsilon^{log} = \int_{l_o}^{l_i} \frac{\delta l_i}{l_i}. \quad (4.2)$$

The logarithmic strain takes into account the strain path and is the correct strain to use when the deformation takes place in a series of increments.

Engineering, or Cauchy strain, e , is an approximation of logarithmic strain but is often used in engineering practice for convenience. It is a measure of the extension relative to the *original* length,

$$e = \frac{l_i - l_o}{l_o}, \quad (4.3)$$

where l_o , is the original length. For small strains (<2%), such as those typically encountered in traditional engineering materials like metals, engineering strain is very similar to logarithmic strain. However, at large strains, the logarithmic strain, ϵ^{log} , is preferred and for uniaxial strain is often calculated from the engineering strain, e , using the output of strain gages:

$$\epsilon^{log} = \ln(1 + e). \quad (4.4)$$

Smith [8] point out that a summative measure of strain (Eqns. 4.2 and 4.4) do not provide a tangent value of the deformation and propose using the instantaneous true strain, ϵ^{int} . They consider the incremental strain proposed in the original definition of strain, and state that with sequential experimental data, ϵ^{int} could be calculated as

$$\epsilon^{int} = \frac{\delta l}{l_i} = \frac{l_i - l_{i-1}}{l_{i-1}}, \quad (4.5)$$

where l_{i-1} is the instantaneous length at the previous increment. For a sufficiently small step size between data points, the summation of ϵ^{int} equals ϵ^{log} . Smith et al. [10] refer to the summation of ϵ^{log} as the total instantaneous true strain, ϵ^{tot} :

$$\epsilon^{tot} = \sum_1^i \frac{l_i - l_{i-1}}{l_{i-1}}. \quad (4.6)$$

With the variety of definitions of strain available, corresponding definitions of Poisson's ratio are possible. The standard definition of Poisson's ratio is

$$\nu_{xy}^{log} = \frac{-\epsilon_x^{log}}{\epsilon_y^{log}}, \quad (4.7)$$

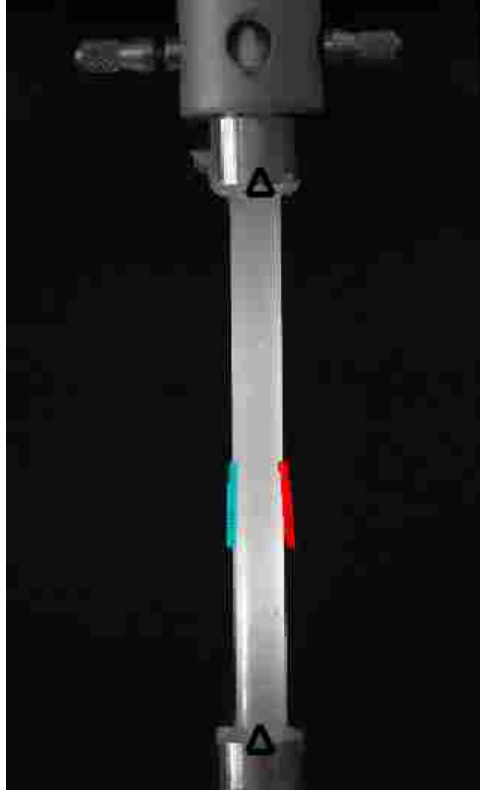


Figure 4.1: Sample image of the DS6a sample after measuring the length and width. Triangles indicate the location of the edges used to calculate length; red and green points indicate the location of the edges used to calculate width over time as the sample was stretched.

where y is the direction of applied strain and x is the orthogonal direction. Accordingly, using the definitions of strain given in Equations 4.3, 4.5, and 4.6 one obtains the following Poisson's ratios:

$$\nu_{xy}^{eng} = \frac{-e_x}{e_y}, \quad (4.8)$$

$$\nu_{xy}^{int} = \frac{-\epsilon_x^{int}}{\epsilon_y^{int}}, \quad (4.9)$$

$$\nu_{xy}^{tot} = \frac{-\epsilon_x^{tot}}{\epsilon_y^{tot}}. \quad (4.10)$$

Data calculated using each of the definitions of Poisson's ratio are compared in this chapter.

4.3 Method

Two types of silicone (three-part addition cure silicones, Ecoflex 00-30 and Dragon Skin, from Smooth-on, Inc.) frequently used to fabricate self-oscillating vocal fold models [16–18, 65, 68, 72, 73] were tested. Equal amounts of parts A and B of the silicone were mixed together with a thinning agent (Silicone Thinner, Smooth-On) to achieve varying degrees of stiffness; the addition of more thinning agent creates softer silicone. Two sets of samples were prepared, which will be referred to as sets (a) and (b). The type of silicone will be referred to as DS or EF, for Dragon Skin or Eco-Flex, followed by a number indicating the ratio (by weight) of thinning agent to parts A and B. For specific samples in this chapter, an (a) or (b) will be appended to indicate the data set from which the sample came. For example, EF8a would be Ecoflex with one part A, one part B, and eight parts thinning agent, and from the first set of data. The various mixtures of silicone are commonly used to fabricate model layers that correspond to the tissue layers of the vocal folds. For example, Murray [16] used DS1 in a layer representing the epithelium, EF9 in a cover, or superficial lamina propria layer, EF4 in a ligament layer, and EF1 in a body layer.

The silicones were thoroughly mixed, vacuumed to remove air bubbles, poured into cylindrical molds (diameter 8.33 mm, 650 mm long), and baked in an oven for 30-45 minutes at 240-250°F then allowed to cool in the mold. The samples were cured to aluminum holders which were used to mount the samples in a tensile test machine (Instron 3342). Most of the samples were stretched from 0 to 40% strain, as measured by the Instron software, at a rate of 2 mm/min. The EF6 and EF8 samples were so soft they were unable to support their weight without sagging excessively at 0% strain; therefore they were stretched to 60 and 70 mm, respectively, prior to beginning the tests, and stretched from approximately 10 to 50% strain during the tests. In order to compare with the other silicone samples, the beginning of each EF6 and EF8 elongation test is reported as if it were 0% strain in subsequent figures. During the extension, 65 pictures of the samples were taken with a tripod-mounted DSLR camera (Nikon 5100).

The images were analyzed in MATLAB as follows. The upper and lower edges of the sample, as indicated by triangles in Figure 4.1, were manually selected in the first frame. The location of the lower edge remained in the same position throughout the test. The location of the upper edge was tracked through time using cross-correlation as follows. A subset of the original image, or a window, centered on the upper edge was cross-correlated with a window located in the

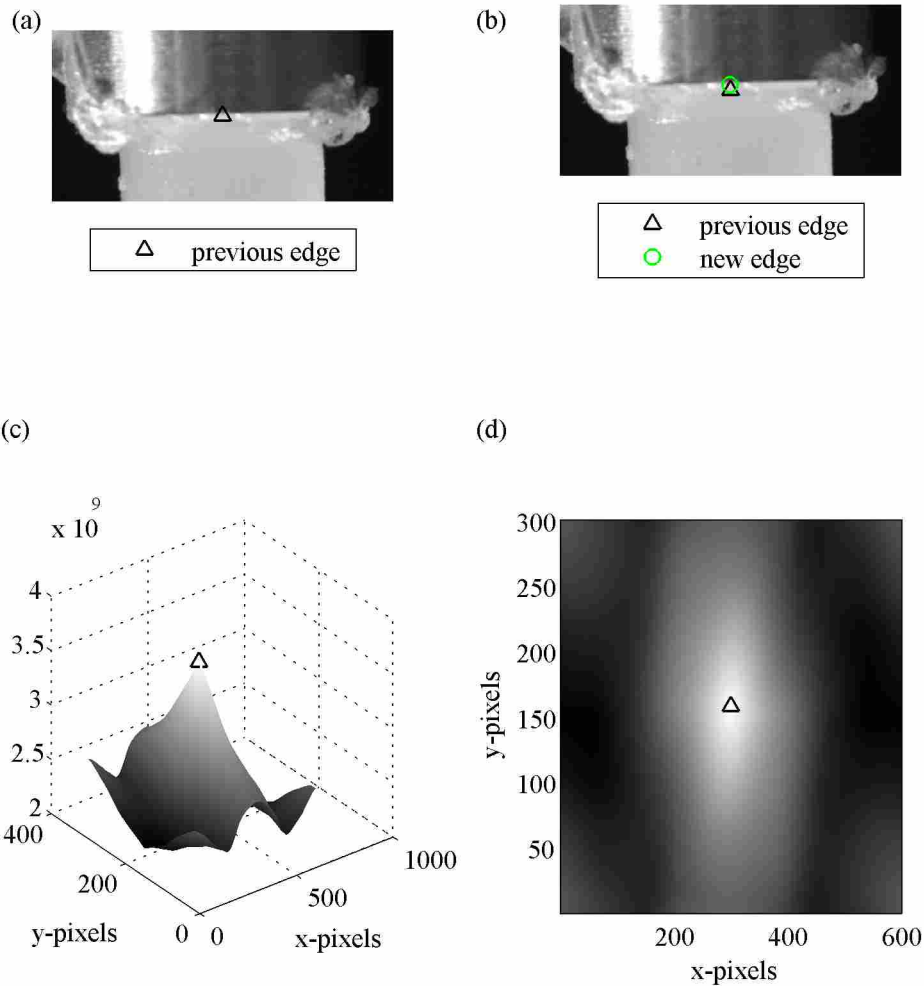


Figure 4.2: (a) Window from previous image with edge marked. (b) Window from present image, showing the location of the edge at the previous step and the present step. (c and d) The cross-correlation with the peak, which indicates the location of the new edge, marked.

same position in the next image, as shown in Figure 4.2. The location where the cross-correlation was a maximum was considered to be the location of the edge in that image. The difference between the location of the upper and lower edge was considered to be the length.

The width was measured by creating a vertically centered window, beginning approximately 20% of the way from the upper edge and extending to approximately 20% of the way from the lower edge of the sample, as shown in Figure 4.3. This window was located in the vertical

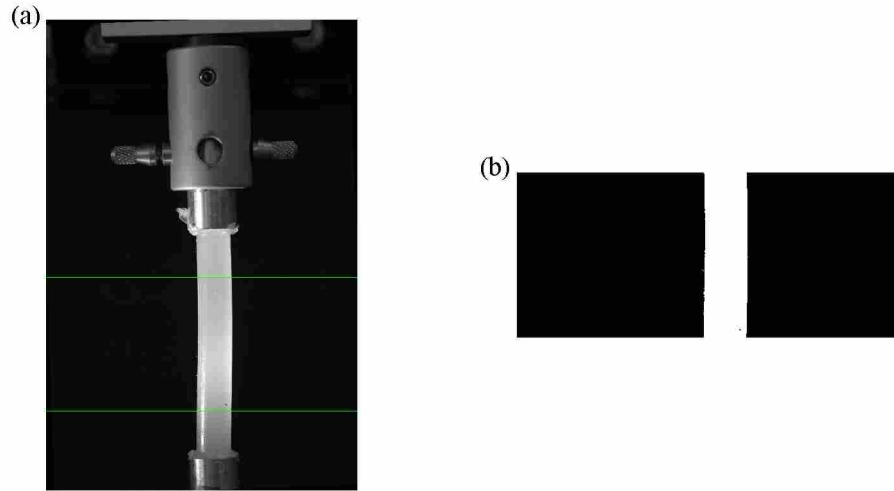


Figure 4.3: (a) Horizontal green lines indicate the location of the window used to find the width. (b) Sample at the location of the window, after thresholding.

center so that the width would be measured at the same point along the length of the sample as it was stretched; this was important because the degree of sagging of the EF6 and EF8 samples was such that the width changed along the length of the sample. A threshold was applied to the window from grayscale intensities to binary numbers, and the left and right edges of the sample were found by searching across a row until a transition from black to white occurred. The width was taken as the average difference between the left and right edges and was measured at 200 points, evenly spaced along the length of the sample. This was done to minimize the effect of the rough edges of the sample on the accuracy of the width. The average width was used as the width of the sample in the subsequent strain calculations. The locations of the upper and lower edges (triangles) and left and right edges over time can be seen in Figure 4.1. The MATLAB code used in the image processing and to calculate Poisson's ratio can be found in Appendix C.

4.4 Results and Discussion

4.4.1 Length and Width Measurements

Accurate measurements of the length and width of the sample were required in order to calculate the axial and transverse strain in the sample, and thereby obtain Poisson's ratio. The

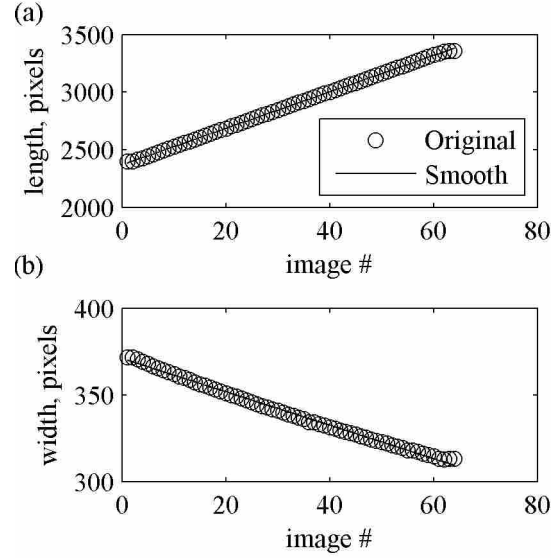


Figure 4.4: Length (a) and width (b) of one sample before and after smoothing.

measured length and width were nearly linear, and little noise was present; in an attempt to further reduce experimental noise, a linear regression was performed on the points, smoothing the length and width, as shown in Figure 4.4.

4.4.2 Poisson's Ratio

Poisson's ratio was calculated according to Eqns. 4.3-4.9 for the original and smoothed data. Despite the smooth appearance of the original data, the linear regression had a large effect on the Poisson's ratio, as can be seen in Figure 4.5 for DS1a. Poisson's ratio calculated with engineering or Cauchy strain has a constant value of approximately 0.4 for v_{xy}^{eng} , whereas with the original, or non-smoothed data v_{xy}^{eng} decrease to approximately 0.4. The true and total instantaneous Poisson's ratios, v_{xy}^{log} , v_{xy}^{tot} are nearly indistinguishable in both cases, as observed by Smith et al. [8]. However, they have a nearly constant value of about 0.5 with the non-smoothed data, whereas the value increases gradually for the smoothed data. The instantaneous strain, v_{xy}^{int} is very sensitive to experimental noise, which Smith et al. [8] saw in their data as well. In the smooth case, v_{xy}^{int} increases with strain at a much higher rate than any of the other strains. Similar trends were observed across all samples.

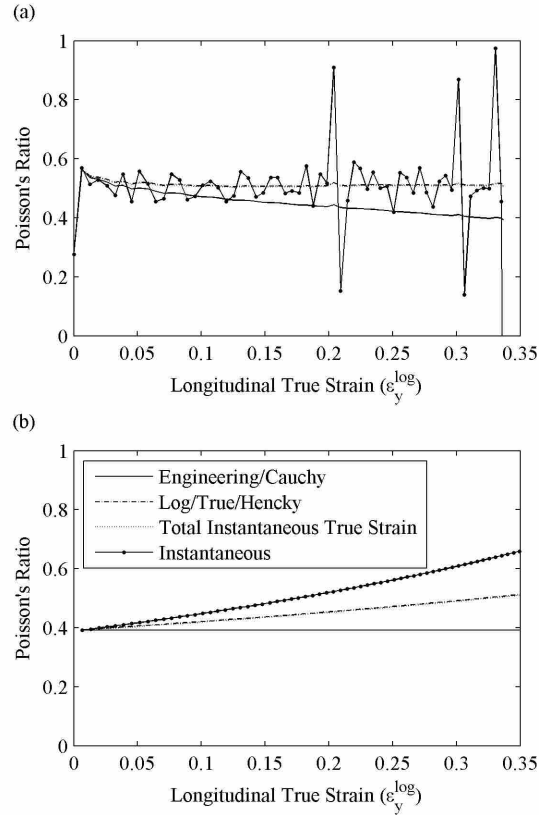


Figure 4.5: Poisson's ratio calculated four different ways, before (a) and after (b) smoothing. The legend is the same for (a) and (b).

4.4.3 Comparison Between Types of Silicone

In order to compare samples, an appropriate definition of Poisson's ratio must be selected. For the present data, ν_{xy}^{int} was often greater than 0.5, which is impossible for isotropic materials. Smith et al. [8] found that ν_{xy}^{int} best captured abrupt changes in the gradient of the strain. Such behavior can occur for auxetic (expanding laterally when stretched, yielding a negative Poisson's ratio) materials. However, in the case of the present data, since the silicone displayed linear strain behavior, it seems that the more traditional definition of strain and Poisson's ratio would be more appropriate. Accordingly, ν_{xy}^{tot} is shown for all the samples tested in Figures 4.6 and 4.7. With the exception of the EF8 samples, there was fairly good agreement ($< 2.6\%$ difference) between the samples created from the same type of silicone, as can be seen in Figure 4.6. It is not surprising that EF8 would not have very consistent data since it was so soft that it sagged excessively and offered

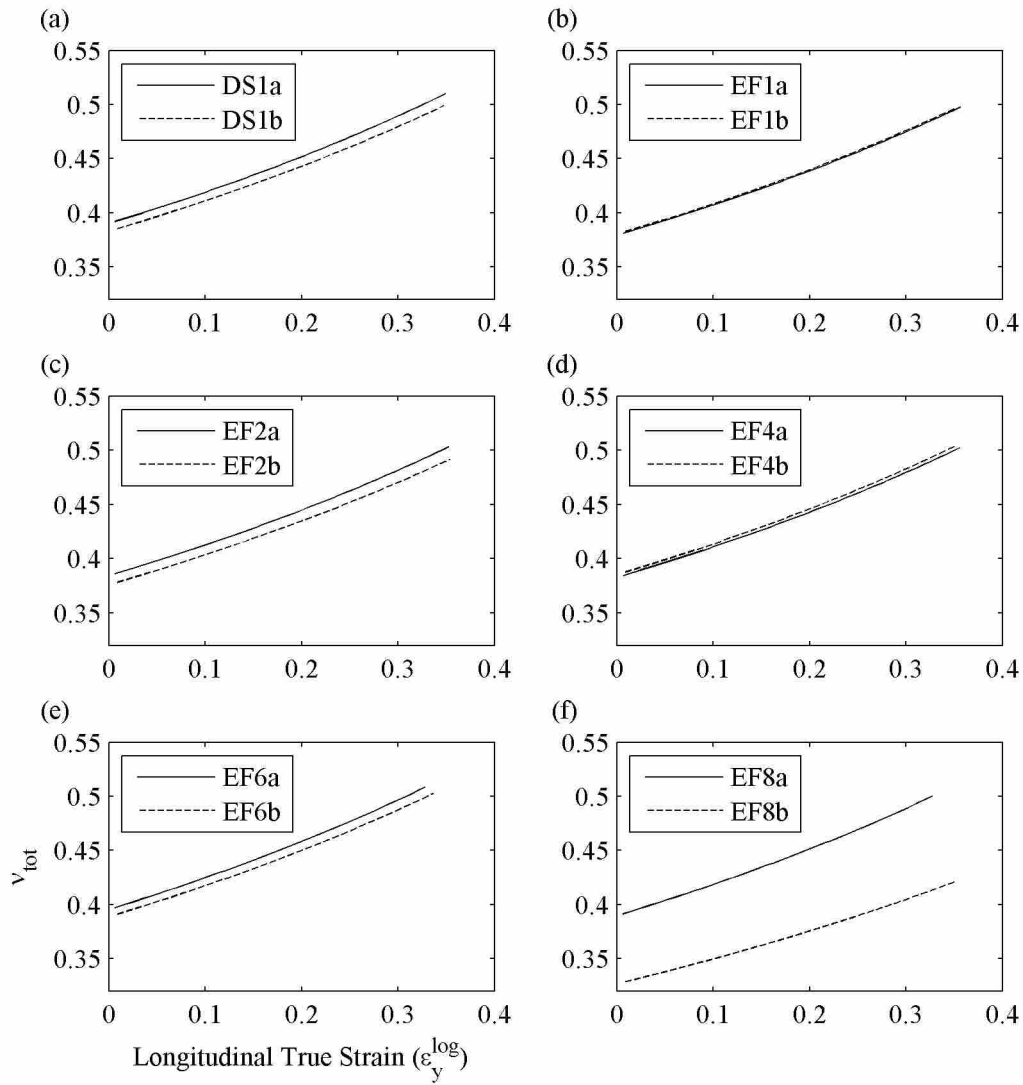


Figure 4.6: Comparison of v_{xy}^{tot} between sets (a) and (b), showing the repeatability of the measurements. Set (b) is a duplicate of set (a).

very little resistance to elongation. It is questionable whether a tensile extension test even applies for such a soft material. However, despite this, both sets of EF8 follow the same trend as the other samples, and while the y-intercept of the curve may be uncertain, it is apparent that even this very soft silicone behaves similarly to the other types. In all cases, Poisson's ratio increases with strain. There appears to be no consistent variation in Poisson's ratio with type of silicone, though there is a strong variation with strain, as is apparent from Figure 4.7. For the type of silicone tested in this

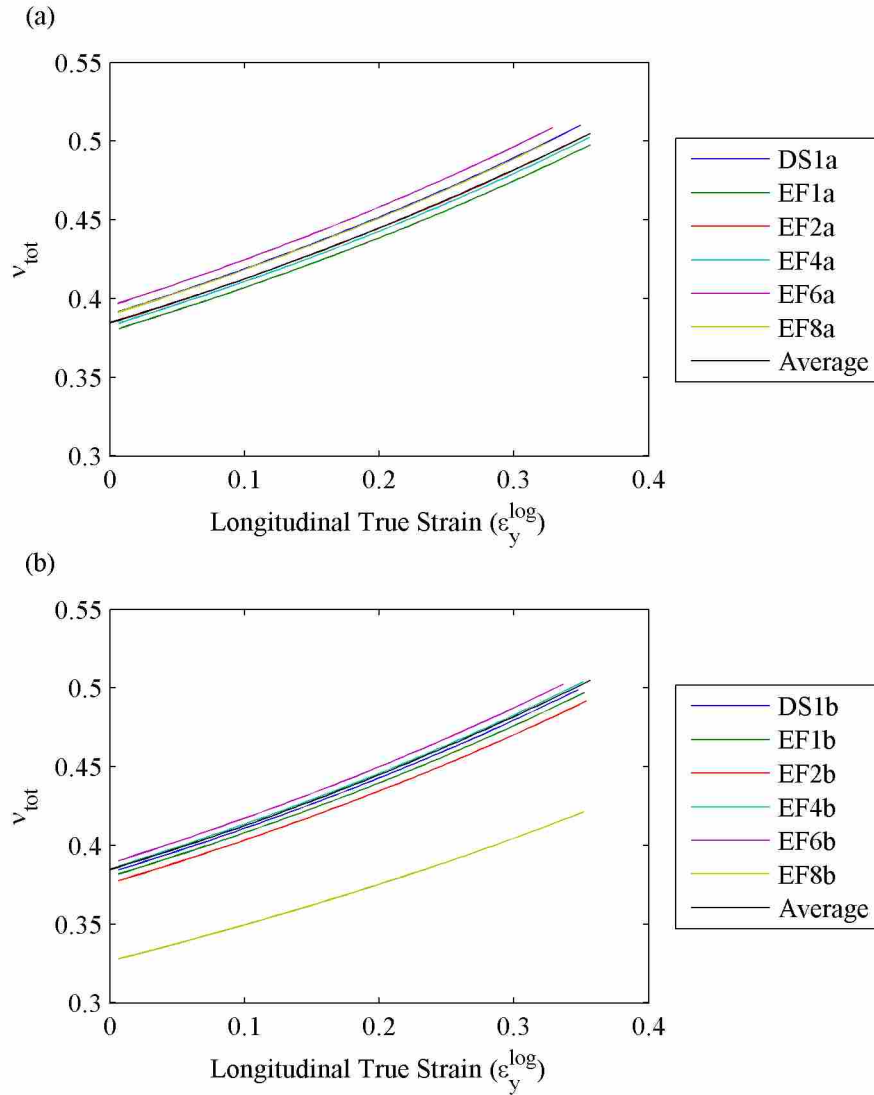


Figure 4.7: Poisson's ratio, v_{xy}^{tot} , for the six types of silicone tested. (a) and (b) represent two separate sets of data. Note that the average of all the samples is also plotted and represents the behavior of the individual samples well.

study, reporting a single value for Poisson's ratio is insufficient, and a strain-varying function is a more appropriate metric.

4.4.4 Poisson's Ratio Function

All of the samples except EF8a and EF8b were used to create a single strain-varying function for Poisson's ratio. The total instantaneous true strain, v_{xy}^{tot} , of all the samples were fit to a

second order polynomial and averaged together, and the averaged curve can also be seen in Figure 4.7. A second order polynomial was fit to the averaged curve to create a strain-dependent Poisson's ratio, as follows:

$$v_{xy}^{tot} = 0.22(\epsilon_y^{log})^2 + 0.26\epsilon_y^{log} + 0.38 \quad (4.11)$$

The polynomial fit the averaged curve so well that it was indistinguishable from the original curve and is not shown. Equation 4.11 deviates from the original data by less than 3%. Equation 4.11 can be used to estimate Poisson's ratio as a function of strain for Dragon Skin or Eco-Flex 00-30 silicone from Smooth-On for mixture ratios of 100-600% silicone to thinning agent. Given the fact that changing the ratio of silicone to thinning agent did not significantly influence Poisson's ratio, it seems reasonable to apply this relation to silicone or similar materials outside this range, though caution should be exercised beyond the reported range. Equation 4.11 can be used, for example, to define Poisson's ratio in computational models of vocal folds using silicone.

4.5 Conclusion

The present data indicate that Poisson's ratio for silicone varies significantly with strain. Therefore, a function for Poisson's ratio as a function of the true strain is provided. This ratio varies from 0.4 to 0.5 over a strain range of 0 to 35%. Alipour [79] measured the Poisson's ratio of human vocal fold tissue to be 0.57, thus the present silicone Poisson's ratios are reasonably close, at least at high strains, to those of vocal fold tissue during voice production. Until an anisotropic material is used in physical models, the Poisson's ratio of silicone reasonably approximates that of human tissue.

4.5.1 Future Work

The present study measured Poisson's ratio for a constant rate of deformation; since vocal fold tissue is a viscoelastic material, exploration of the effect of varying strain rate on Poisson's ratio might be of interest. This is especially true for the softer varieties of silicone, which exhibit significant viscoelastic properties. Furthermore, the samples were all prepared under similar con-

ditions, particularly the step of curing in the oven. It has been observed that curing temperature and time can affect the Young's modulus of silicone; future work could involve exploring if curing conditions affect the Poisson's ratio as well.

CHAPTER 5. CONCLUSION

5.1 A Mother's Lullaby

The ultimate purpose for the analysis in this thesis is to increase understanding of the structure that allows mothers to sing their babies to sleep, Abraham Lincoln to deliver the Gettysburg Address, and actors to entertain and inspire. The chapters in this thesis were intended to develop knowledge that will allow voice researchers to better understand vocal fold dynamics. In Chapter 2, porcine vocal folds were shown to be qualitatively similar in shape to human vocal folds and may thus constitute a suitable model. Further, the level of distortion freezing induces in laryngeal tissue, which is relevant information for those doing histological processing of the vocal folds, was quantified. In Chapter 3, the accuracy and potential applicability of a stereo-endoscope, an imaging tool designed to provide three-dimensional information about the vibrating surface of *in vivo* vocal folds, was explored. The stereo-endoscope was shown to be most accurate in the transverse plane, and it is apparent that more development is needed before the stereo-endoscope can provide clinically relevant information in the inferior-superior direction. In Chapter 4, a function for a strain-varying Poisson's ratio was provided for use in computer models and for comparison with actual tissue. Such information has the potential to help voice researchers in their quest to understand how the humans produce sound, like the sound of a mother's lullaby.

5.2 Chapter 2: Quantification of Porcine Vocal Fold Geometry

In Chapter 2, the medial surfaces at the mid-membranous section of the vocal folds were compared, showing that freezing does cause a geometrical distortion of the tissue, but not in a consistent manner. Overall, the tissue experiences about a 5% change in volume in the entire larynx, but this does not appear to cause consistent or uniform shrinkage or expansion in any one direction in the region of the vocal folds.

The geometry of the medial surface of porcine vocal folds was also quantified and compared with human and canine vocal folds and various synthetic model geometric data. The shape is similar to the other geometries, though the porcine folds appear to be slightly thicker. It is apparent that more human geometric data is needed for a better comparison. Some obvious differences between pig and human vocal folds exist, such as the underlying tissue structure and the 40° downward angle of the porcine folds, but otherwise it is evident that the geometry of porcine vocal folds is relatively similar to that of canine and human vocal folds.

Despite the fact that the geometry plays such an important role in phonation, relatively little quantitative information is available regarding the shape of the vocal folds, particularly of the internal layers. This is due to the difficulty associated with obtaining sufficient spatial resolution in medical imaging and the distortion associated with histological processing. The present work addressed one part of the challenge of obtaining accurate geometrical information from histological processing by quantifying the overall three-dimensional effect of freezing, one step in a common method of fixation shown to have less distortion, on tissue geometry.

Though traditional medical imaging does not yet allow the differentiation of tissue layers, the technology is continually improving and the future development of such capabilities seems likely. The method outlined in this chapter to go from medical images to a 2D profile describing the geometry could be applied to obtain descriptions of the different tissue layers on excised human larynges, and even to *in vivo* humans, once this level of detail becomes technologically feasible. One obvious limitation of histological processing is that the excised tissue cannot be postured for voicing in precisely the same way as that which occurs *in vivo*. Even when the vocal folds are adducted via sutures or other means for phonation, the nerves controlling muscles activation are not stimulated, thus geometry obtained in this manner is still only a limited representation of *in vivo* conditions. The ability to posture the folds for speech is a major advantage of *in vivo* medical imaging and will certainly be used in the future to obtain accurate geometrical models of the vocal folds. However, until that time, the methods described in this chapter can contribute to an overall estimate of the accuracy of future geometries derived from histological section processing.

5.3 Chapter 3: Validating a Stereo-Endoscope with a Synthetic Vocal Fold Model

In this chapter a synthetic vocal fold model was utilized as a test subject to evaluate the accuracy of stereo-endoscopy to make three-dimensional measurements. The locations of specific three-dimensional coordinates found using the stereo-endoscope were compared with locations obtained using two DSLR cameras that constructed a secondary imaging system to provide a more accurate geometrical description of the object. Using stereo-vision techniques to reconstruct three-dimensional coordinates is prone to several potential sources of error, including error from calibration and correspondence. The error that comes mainly from hardware limitation and calibration of the stereo-endoscope was evaluated. The error was low in the transverse plane, but high in the inferior-superior direction. Therefore, it was concluded that stereo-endoscopy still could potentially be used to measure absolute distances in the transverse plane *in vivo*. Further improvements, such as higher image resolution, brighter luminosity, and less optical distortion, are awaited. Until then, future work could include examining the spatial distribution of error, studying the error in absolute position relative to the error in tracking a point's displacement over time, or further theoretical study of the stereo-endoscope algorithms to identify the largest sources of error.

5.4 Chapter 4: Poisson's Ratio of Silicone

A strain-varying function for Poisson's ratio was proposed for silicone, a material commonly used in vocal fold model making. The ratio varies from about 0.4 to 0.5 for strains from 0 to 35%, which is close to that of human tissue. The present study measured Poisson's ratio for a constant rate of deformation; since vocal fold tissue is a viscoelastic material, it would be of interest to explore the effect of varying strain rate on Poisson's ratio, particularly for the softer varieties of silicone that exhibit viscoelastic properties. Furthermore, the samples were all prepared under similar conditions, particularly the step of curing in the oven. It has been observed that curing temperature and time can effect the Young's modulus of silicone; future work could involve exploring whether curing conditions affect the Poisson's ratio as well.

REFERENCES

- [1] Gray, H., 2000. *Gray's anatomy of the human larynx*. viii, 2
- [2] NIDCD, 2010. *Quick statistics*. 1
- [3] NIDCD, 2010. *Voice, speech, and language charts and tables*. 1
- [4] Ziethe, A., Patel, R., Kunduk, M., Eysholdt, U., and Graf, S., 2011. "Clinical analysis methods of voice disorders." *Current Bioinformatics*, **6**(3), pp. 270–285. 3
- [5] Dollinger, M., Kobler, J., A Berry, D., D Mehta, D., Luegmair, G., and Bohr, C., 2011. "Experiments on analysing voice production: Excised (human, animal) and in vivo (animal) approaches." *Current Bioinformatics*, **6**(3), pp. 286–304. 3
- [6] Kniesburges, S., Thomson, S. L., Barney, A., Triep, M., idlof, P., Horcek, J., Brcker, C., and Becker, S., 2011. "In vitro experimental investigation of voice production." *Current bioinformatics*, **6**(3), p. 305. 4, 42
- [7] Alipour, F., Brucker, C., D Cook, D., Gommel, A., Kaltenbacher, M., Mattheus, W., Mongeau, L., Nauman, E., Schwarze, R., and Tokuda, I., 2011. "Mathematical models and numerical schemes for the simulation of human phonation." *Current Bioinformatics*, **6**(3), pp. 323–343. 4
- [8] Smith, C., Wootton, R., and Evans, K., 1999. "Interpretation of experimental data for poisson's ratio of highly nonlinear materials." *Experimental mechanics*, **39**(4), pp. 356–362. 6, 42, 44, 49, 50
- [9] Inagi, K., Khidr, A. A., Ford, C. N., Bless, D. M., and Heisey, D. M., 1997. "Correlation between vocal functions and glottal measurements in patients with unilateral vocal fold paralysis." *Laryngoscope*, **107**(6), pp. 782–91. 7
- [10] Smith, M. E., Marsh, J. H., Cotton, R. T., and Myer, C. M., r., 1993. "Voice problems after pediatric laryngotracheal reconstruction: videolaryngostroboscopic, acoustic, and perceptual assessment." *Int J Pediatr Otorhinolaryngol*, **25**(1-3), pp. 173–81. 7, 43, 44
- [11] Berry, D. A., Herzel, H., Titze, I. R., and Story, B. H., 1996. "Bifurcations in excised larynx experiments." *J Voice*, **10**(2), pp. 129–38. 7
- [12] Berry, D. A., and Titze, I. R., 1996. "Normal modes in a continuum model of vocal fold tissues." *J Acoust Soc Am*, **100**(5), pp. 3345–54. 7
- [13] Titze, I. R., and Talkin, D. T., 1979. "A theoretical study of the effects of various laryngeal configurations on the acoustics of phonation." *J Acoust Soc Am*, **66**(1), pp. 60–74. 7

- [14] Bhattacharya, P., and Siegmund, T. H., 2012. “A canonical biomechanical vocal fold model.” *J Voice*, **26**(5), pp. 535–47. 7
- [15] Smith, S. L., and Thomson, S. L., 2012. “Effect of inferior surface angle on the self-oscillation of a computational vocal fold model.” *J Acoust Soc Am*, **131**(5), pp. 4062–75. 7, 42
- [16] Murray, P. R., and Thomson, S. L., 2012. “Vibratory responses of synthetic, self-oscillating vocal fold models.” *J Acoust Soc Am*, **132**(5), pp. 3428–38. 7, 17, 30, 42, 46
- [17] Murray, P. R., Thomson, S. L., and Smith, M. E., 2014. “A synthetic, self-oscillating vocal fold model platform for studying augmentation injection.” *J Voice*, **28**(2), pp. 133–43. 7, 42, 46
- [18] Pickup, B. A., and Thomson, S. L., 2010. “Flow-induced vibratory response of idealized versus magnetic resonance imaging-based synthetic vocal fold models.” *J Acoust Soc Am*, **128**(3), pp. EL124–9. 7, 8, 42, 46
- [19] Chan, R. W., and Rodriguez, M. L., 2008. “A simple-shear rheometer for linear viscoelastic characterization of vocal fold tissues at phonatory frequencies.” *J Acoust Soc Am*, **124**(2), pp. 1207–19. 8
- [20] Chan, R. W., and Titze, I. R., 2000. “Viscoelastic shear properties of human vocal fold mucosa: theoretical characterization based on constitutive modeling.” *J Acoust Soc Am*, **107**(1), pp. 565–80. 8
- [21] Chan, R. W., and Titze, I. R., 2003. “Effect of postmortem changes and freezing on the viscoelastic properties of vocal fold tissues.” *Ann Biomed Eng*, **31**(4), pp. 482–91. 8
- [22] Chhetri, D. K., Zhang, Z., and Neubauer, J., 2011. “Measurement of young’s modulus of vocal folds by indentation.” *J Voice*, **25**(1), pp. 1–7. 8
- [23] Goodyer, E., Hemmerich, S., Muller, F., Kobler, J. B., and Hess, M., 2007. “The shear modulus of the human vocal fold, preliminary results from 20 larynxes.” *Eur Arch Otorhinolaryngol*, **264**(1), pp. 45–50. 8
- [24] Goodyer, E., Muller, F., Licht, K., and Hess, M., 2007. “In vivo measurement of the shear modulus of the human vocal fold: interim results from eight patients.” *Eur Arch Otorhinolaryngol*, **264**(6), pp. 631–5. 8
- [25] Haji, T., Mori, K., Omori, K., and Isshiki, N., 1992. “Mechanical properties of the vocal fold. stress-strain studies.” *Acta Otolaryngol*, **112**(3), pp. 559–65. 8
- [26] Hess, M. M., Mueller, F., Kobler, J. B., Zeitels, S. M., and Goodyer, E., 2006. “Measurements of vocal fold elasticity using the linear skin rheometer.” *Folia Phoniatr Logop*, **58**(3), pp. 207–16. 8
- [27] Berry, D. A., Clark, M. J., Montequin, D. W., and Titze, I. R., 2001. “Characterization of the medial surface of the vocal folds.” *Ann Otol Rhinol Laryngol*, **110**(5 Pt 1), pp. 470–7. 8, 11, 16, 18

- [28] Sidlof, P., Svec, J. G., Horacek, J., Vesely, J., Klepacek, I., and Havlik, R., 2008. “Geometry of human vocal folds and glottal channel for mathematical and biomechanical modeling of voice production.” *J Biomech*, **41**(5), pp. 985–95. 8, 11, 17, 18
- [29] Agarwal, M., Scherer, R. C., and Hollien, H., 2003. “The false vocal folds: shape and size in frontal view during phonation based on laminagraphic tracings.” *J Voice*, **17**(2), pp. 97–113. 8, 17
- [30] Bakhshae, H., Moro, C., Kost, K., and Mongeau, L., 2013. “Three-dimensional reconstruction of human vocal folds and standard laryngeal cartilages using computed tomography scan data.” *J Voice*, **27**(6), pp. 769–77. 8
- [31] Oyamada, Y., Yumoto, E., Nakano, K., and Goto, H., 2005. “Asymmetry of the vocal folds in patients with vocal fold immobility.” *Arch Otolaryngol Head Neck Surg*, **131**(5), pp. 399–406. 8
- [32] Hiramatsu, H., Tokashiki, R., and Suzuki, M., 2008. “Usefulness of three-dimensional computed tomography of the larynx for evaluation of unilateral vocal fold paralysis before and after treatment: technique and clinical applications.” *Eur Arch Otorhinolaryngol*, **265**(6), pp. 725–30. 8
- [33] Gokcan, M. K., Kurtulus, D. F., Ustuner, E., Ozyurek, E., Kesici, G. G., Erdem, S. C., Dursun, G., and Yagci, C., 2010. “A computational study on the characteristics of airflow in bilateral abductor vocal fold immobility.” *Laryngoscope*, **120**(9), pp. 1808–18. 8
- [34] Johnson, R. E., Sigman, J. D., Funk, G. F., Robinson, R. A., and Hoffman, H. T., 1997. “Quantification of surgical margin shrinkage in the oral cavity.” *Head Neck*, **19**(4), pp. 281–6. 9
- [35] Kimura, M., Tayama, N., and Chan, R. W., 2003. “Geometrical deformation of vocal fold tissues induced by formalin fixation.” *Laryngoscope*, **113**(4), pp. 607–13. 9
- [36] Eckel, H. E., and Sittel, C., 1995. “Morphometry of the larynx in horizontal sections.” *Am J Otolaryngol*, **16**(1), pp. 40–8. 9
- [37] Tayama, N., Chan, R. W., Kaga, K., and Titze, I. R., 2002. “Functional definitions of vocal fold geometry for laryngeal biomechanical modeling.” *Ann Otol Rhinol Laryngol*, **111**(1), pp. 83–92. 9, 10, 16
- [38] Alipour, F., Finnegan, E. M., and Jaiswal, S., 2013. “Phonatory characteristics of the excised human larynx in comparison to other species.” *J Voice*, **27**(4), pp. 441–7. 10
- [39] Alipour, F., and Jaiswal, S., 2008. “Phonatory characteristics of excised pig, sheep, and cow larynges.” *J Acoust Soc Am*, **123**(6), pp. 4572–81. 10, 12
- [40] Garrett, C. G., Coleman, J. R., and Reinisch, L., 2000. “Comparative histology and vibration of the vocal folds: implications for experimental studies in microlaryngeal surgery.” *Laryngoscope*, **110**(5 Pt 1), pp. 814–24. 10

- [41] Jiang, J. J., Raviv, J. R., and Hanson, D. G., 2001. “Comparison of the phonation-related structures among pig, dog, white-tailed deer, and human larynges.” *Ann Otol Rhinol Laryngol*, **110**(12), pp. 1120–5. 10
- [42] Yushkevich, P. A., Piven, J., Hazlett, H. C., Smith, R. G., Ho, S., Gee, J. C., and Gerig, G., 2006. “User-guided 3d active contour segmentation of anatomical structures: significantly improved efficiency and reliability.” *Neuroimage*, **31**(3), pp. 1116–28. 12
- [43] Scherer, R. C., Shinwari, D., De Witt, K. J., Zhang, C., Kucinski, B. R., and Afjeh, A. A., 2001. “Intraglottal pressure profiles for a symmetric and oblique glottis with a divergence angle of 10 degrees.” *J Acoust Soc Am*, **109**(4), pp. 1616–30. 17
- [44] Kitzing, P., 1985. “Stroboscopy—a pertinent laryngological examination.” *J Otolaryngol*, **14**(3), pp. 151–7. 28
- [45] Kiritani, S., Hirose, H., and Imagawa, H., 1993. “High-speed digital image-analysis of vocal cord vibration in diplophonia.” *Speech Communication*, **13**(1-2), pp. 23–32. 28
- [46] Baer, T., Lofqvist, A., and McGarr, N. S., 1983. “Laryngeal vibrations: a comparison between high-speed filming and glottographic techniques.” *J Acoust Soc Am*, **73**(4), pp. 1304–8. 28
- [47] Bless, D. M., Hirano, M., and Feder, R. J., 1987. “Videostroboscopic evaluation of the larynx.” *Ear Nose Throat J*, **66**(7), pp. 289–96. 28
- [48] Van Den Berg, J., and Tan, T. S., 1959. “Results of experiments with human larynxes.” *Pract Otorhinolaryngol (Basel)*, **21**, pp. 425–50. 28
- [49] Dollinger, M., Berry, D. A., and Berke, G. S., 2005. “Medial surface dynamics of an in vivo canine vocal fold during phonation.” *J Acoust Soc Am*, **117**(5), pp. 3174–83. 28, 41
- [50] Berry, D. A., Montequin, D. W., and Tayama, N., 2001. “High-speed digital imaging of the medial surface of the vocal folds.” *J Acoust Soc Am*, **110**(5 Pt 1), pp. 2539–47. 28
- [51] Tang, S., Zhang, Y., Qin, X., Wang, S., and Wan, M., 2013. “Measuring body layer vibration of vocal folds by high-frame-rate ultrasound synchronized with a modified electroglottograph.” *J Acoust Soc Am*, **134**(1), pp. 528–38. 28
- [52] Saito, S., Fukuda, H., Kitahira, S., Isogai, Y., Tsuzuki, T., Muta, H., Takyama, E., Fujika, T., Kokawa, N., and Makino, K., 1985. *Pellet tracking in the vocal fold while phonating: experimental study using canine larynges with muscle activity*. Denver Center for the Performing Arts 1985, Denver, CO, p. 169182. 28
- [53] Tokuda, I. T., Iwawaki, M., Sakakibara, K., Imagawa, H., Nito, T., Yamasoba, T., and Tayama, N., 2013. “Reconstructing three-dimensional vocal fold movement via stereo matching.” *Acoustical Science and Technology*, **34**(5), pp. 374–377. 28, 29, 31, 32, 34
- [54] Schuster, M., Lohscheller, J., Kummer, P., Eysholdt, U., and Hoppe, U., 2005. “Laser projection in high-speed glottography for high-precision measurements of laryngeal dimensions and dynamics.” *Eur Arch Otorhinolaryngol*, **262**(6), pp. 477–81. 28

- [55] Wurzbacher, T., Voigt, I., Schwarz, R., Dollinger, M., Hoppe, U., Penne, J., Eysholdt, U., and Lohscheller, J., 2008. “Calibration of laryngeal endoscopic high-speed image sequences by an automated detection of parallel laser line projections.” *Med Image Anal*, **12**(3), pp. 300–17. 28
- [56] George, N. A., de Mul, F. F., Qiu, Q., Rakhorst, G., and Schutte, H. K., 2008. “Depth-kymography: high-speed calibrated 3d imaging of human vocal fold vibration dynamics.” *Phys Med Biol*, **53**(10), pp. 2667–75. 28
- [57] Luegmair, G., Kniesburges, S., Zimmermann, M., Sutor, A., Eysholdt, U., and Dollinger, M., 2010. “Optical reconstruction of high-speed surface dynamics in an uncontrollable environment.” *IEEE Trans Med Imaging*, **29**(12), pp. 1979–91. 28, 29, 41
- [58] Yu, L., Liu, G., Rubinstein, M., Saidi, A., Wong, B. J., and Chen, Z., 2009. “Office-based dynamic imaging of vocal cords in awake patients with swept-source optical coherence tomography.” *J Biomed Opt*, **14**(6), p. 064020. 29
- [59] Chang, E. W., Kobler, J. B., and Yun, S. H., 2011. “Triggered optical coherence tomography for capturing rapid periodic motion.” *Sci Rep*, **1**, p. 48. 29
- [60] Sawashima, M., and Miyazaki, S., 1974. “Stereo-fiberscopic measurement of the larynx: a preliminary experiment by use of ordinary laryngeal fiberscopes.” *Ann. Bull. RILP*, **8**, pp. 7–10. 29
- [61] Fujimura, O., Baer, T., and Niimi, S., 1979. “A stereo-fiberscope with a magnetic interlens bridge for laryngeal observation.” *J Acoust Soc Am*, **65**(2), pp. 478–80. 29
- [62] Sawashima, M., Hirose, H., Honda, K., Yoshioka, H., Hibi, S., Kawase, N., and Yamada, M., 1983. *Stereoendoscopic measurement of the laryngeal structure*. College-Hill Press, San Diego, pp. 264–276. 29
- [63] Sommer, D. E., Tokuda, I. T., Peterson, S. D., Sakakibara, K., Imagawa, H., Yamauchi, A., Nito, T., Yamasoba, T., and Tayama, N., 2014. “Estimation of inferior-superior vocal fold kinematics from high-speed stereo endoscopic data in vivo.” *J Acoust Soc Am*, **136**(6), p. 3290. 29, 31, 39, 40
- [64] Drechsel, J. S., and Thomson, S. L., 2008. “Influence of supraglottal structures on the glottal jet exiting a two-layer synthetic, self-oscillating vocal fold model.” *J Acoust Soc Am*, **123**(6), pp. 4434–45. 30, 42
- [65] Murray, P. R., and Thomson, S. L., 2011. “Synthetic, multi-layer, self-oscillating vocal fold model fabrication.” *J Vis Exp*(58). 30, 42, 46
- [66] Titze, I. R., 2000. *Principles of Voice Production (2 ed.)*. National Center for Voice and Speech. 30
- [67] Baken, R., and Orlikoff, R., 2000. *Clinical Measurement of Speech and Voice (2 ed.)*. Singular Publishing Group, San Diego, CA. 30

- [68] Riede, T., Tokuda, I. T., Munger, J. B., and Thomson, S. L., 2008. “Mammalian laryngeal air sacs add variability to the vocal tract impedance: physical and computational modeling.” *J Acoust Soc Am*, **124**(1), pp. 634–47. 30, 42, 46
- [69] Abdel-Aziz, YI; Karara, H., 1971. Direct linear transformation from comparator coordinates into object space coordinates in close-range photogrammetry. 34
- [70] Imagawa, H., Sakakibara, K.-I., Tokuda, I. T., Otsuka, M., and Tayama, N., 2010. “Estimation of glottal area function using stereo-endoscopic high-speed digital imaging.” In *Interspeech*, pp. 1005–1008. 41
- [71] Thomson, S. L., Mongeau, L., and Frankel, S. H., 2005. “Aerodynamic transfer of energy to the vocal folds.” *J Acoust Soc Am*, **118**(3 Pt 1), pp. 1689–700. 42
- [72] Pickup, B. A., and Thomson, S. L., 2009. “Influence of asymmetric stiffness on the structural and aerodynamic response of synthetic vocal fold models.” *J Biomech*, **42**(14), pp. 2219–25. 42, 46
- [73] Murray, P. R., 2011. “Flow induced responses of normal, bowed, and augmented synthetic vocal fold models.” Thesis. 42, 46
- [74] Titze, I. R., 2006. *The myoelastic aerodynamic theory of phonation (1 ed.)*. National Center for Voice and Speech. 42
- [75] Hewitt, J., Guilak, F., Glisson, R., and Vail, T. P., 2001. “Regional material properties of the human hip joint capsule ligaments.” *Journal of Orthopaedic Research*, **19**(3), pp. 359–364. 42
- [76] Greaves, G. N., Greer, A. L., Lakes, R. S., and Rouxel, T., 2011. “Poisson’s ratio and modern materials.” *Nat Mater*, **10**(11), pp. 823–837. 42
- [77] Mott, P. H., Dorgan, J. R., and Roland, C. M., 2008. “The bulk modulus and poisson’s ratio of incompressible materials.” *Journal of Sound and Vibration*, **312**(45), pp. 572–575. 42
- [78] Rees, D., 2012. *Basic Engineering Plasticity: An Introduction with Engineering and Manufacturing Applications*. Elsevier Science. 43
- [79] Alipour, F., and Vigmostad, S., 2012. “Measurement of vocal folds elastic properties for continuum modeling.” *Journal of voice : official journal of the Voice Foundation*, **26**(6), pp. 816.e21–816.e29. 53

APPENDIX A. RELAVENT MATLAB CODE FROM CHAPTER 1

MATLAB was used calculate the volume of the tissue and airway. The CT images were converted into tiffs in Analyze, then opened in MATLAB. The image was converted to black and white using a threshold selected in PickThreshAuto.m, based off of the value at the edge of the airway. Connected components was used to find the area of the tissue or airway. ExtractAreaALL.m runs the function PickThreshAuto and plots the results.

A.1 ExtractAreaALL.m

```
close all
clear all
clc

%% User input
temp='R';
Lnum=5;
if temp=='R'
colNum=Lnum*2-1;
else
colNum=Lnum*2;
end
orientation='trans';

%% Code:
filename=['F:\...\RotTiff\' num2str(Lnum) '\' temp num2str(Lnum) orientation];
limits=load('MASTERLIMITS.txt');
savename=['Anatomical_' temp num2str(Lnum) orientation '.txt'];
if strcmp(orientation, 'trans')
mult=0;
```

```

elseif strcmp(orientation, 'sag')
mult=1;
elseif strcmp(orientation, 'cor')
mult=2;
else
ERROR='TRUE'
end

start=limits(1+mult*15, colNum);
increment=1;
finish=limits(2+mult*15, colNum);
image2view=limits(3+mult*15, colNum);
T0=limits(4+mult*15, colNum);
Tf=limits(5+mult*15, colNum);
xlim0=limits(6+mult*15, colNum);
xlimf=limits(7+mult*15, colNum);
ylim0=limits(8+mult*15, colNum);
ylimf=limits(9+mult*15, colNum);
AW0=limits(10+mult*15, colNum);
AWf=limits(11+mult*15, colNum);
twoArea0=limits(12+mult*15, colNum);
twoAreaf=limits(13+mult*15, colNum);
twoAreaA=limits(14+mult*15, colNum);
twoAreaB=limits(15+mult*15, colNum);

%% find maximum value for the entire volume (for all slices)
for i=start:increment:finish
ImageName=[filename num2str(i, '%.4d') '.tif'];
im=imread(ImageName);
if ndims(im)>1
im=im(:,:,1);
end
im=double(im);
N(i)=max(max(im));
end
N=max(max(N));

```

```

%% pick a point in the center of the airway
ImageName=[filename num2str(image2view, '%.4d') '.tif'];
im=double(imread(ImageName));
im=im/N;
figure, imshow(im), title('Shifted image. Pick point in airway')
[x y]=ginput(1);
figure
%% T for each image
for i=T0:Tf
ImageName=[filename num2str(i, '%.4d') '.tif'];
im=imread(ImageName);
if ndims(im)>1
im=im(:,:,1);
end
im=double(im);
im=im/N;
T(i-T0+1)=PickThreshAuto(im, x, y);
end

Tavg=mean(T);
Tstd=std(T);
newlist=[];
newlist2=[];
for i=1:length(T)
if T(i)>Tavg-std(T) && T(i)<Tavg+std(T)
newlist=[newlist T(i)];
end
if T(i)>Tavg-2*std(T) && T(i)<Tavg+2*std(T)
newlist2=[newlist2 T(i)];
end
end
T68=mean(newlist);
T95=mean(newlist2);
figure, plot(1:length(T), T, 1:length(T), T68), xlabel('slice number'),

```

```

ylabel('threshold used')
AAW=zeros(1,finish-start+1);
AAW2=AAW;
figure,

%% Calculate and Plot the area for all the images
for i=start:increment:finish
ImageName=[filename num2str(i, '%.4d') '.tif'];
im=imread(ImageName);
if ndims(im)>1
im=im(:,:,1);
end
im=double(im);
im=im/N;
imbw=im2bw(im,T68);
A(i-start+1)=sum(sum(imbw));
%% find the area of the airway
if i>AW0 && i<AWf
imbw=abs(imbw-1);
imbwc=imbw(ylim0:ylimf,xlim0:xlimf);
% imc=im(ylim0:ylimf,xlim0:xlimf);
stats=regionprops(logical(imbwc),'Area','PixelList');
AW=zeros(size(imbwc));
Alist=cat(1,stats.Area);
%find biggest area and set to zero (background)
if strcmp(orientation,'trans')
Alist(find(max(Alist)==Alist))=0;
end
%find next biggest area, add to Airway Area, add to plot, and set to zero
AAW(i-start+1)=max(Alist);
ConCompNum=find(max(Alist)==Alist);
list=getfield(stats(ConCompNum),'PixelList');
for j=1:size(list,1)
AW(list(j,2),list(j,1))=1;
end
Alist(find(max(Alist)==Alist))=0;

```

```

AW2=AW;
AAW2(i-start+1)=AAW(i-start+1);
if (i>=twoArea0 && i<=twoAreaf) || (i>=twoAreaA && i<=twoAreaB)
if length(Alist)>1 && max(Alist)>5
AAW2(i-start+1)=max(Alist)+AAW2(i-start+1);
ConCompNum=find(max(Alist)==Alist);
list=getfield(stats(ConCompNum), 'PixelList');
for j=1:size(list,1)
AW2(list(j,2),list(j,1))=1;
end
end
end
else
imbwc=zeros(size(imbw));
AW=zeros(size(imbw));
AW2=AW;
end
subplot(2,1,1),imshowpair(AW,AW2,'montage'), title(['slice #' num2str(i) ' L:1 area,
R: 2 areas'])
subplot(2,1,2),imshowpair(im,imbw,'montage'), title('L: original image,
R: thresholded area')
if i>150 && i<170
%           pause(.0000005)
%           waitforbuttonpress
else
pause(.0001)
end
end

slicenum=start:increment:finish;
A_and_x=[slicenum' A' AAW2' padarray(T,[0 finish-start+1-length(T)],0,'post')'];
figure, plot(slicenum,A,slicenum,AAW,slicenum,AAW2), xlabel('slice'),
ylabel('Area in pixels')
save(savename,'A_and_x','-ascii')

volume=0;

```

```

for i=start:finish
volume=volume+A(find(slicenum==i));
end
volume

sliderGUI(filename, start, finish, N, T68, xlim0, xlimf, ylim0, ylimf, AW0, AWf, twoArea0, twoAreaf,
twoAreaA, twoAreaB, orientation)

```

A.2 PickThreshAuto.m

```

function [ newT ] = PickThreshAuto(im, x, y)
%% edge finding
[Eim, T]=edge(im, 'Sobel');
Eim=edge(im, 'Sobel', T);
while Eim(round(y), round(x))==0
x=x+1;
end
%% do connected components on the edge image
L = bwlabel(Eim, 8);
stats=regionprops(Eim, 'PixelList');
ConCompNum=L(round(y), round(x));
list=getfield(stats(ConCompNum), 'PixelList');
rows=[list(:, 2)];
cols=[list(:, 1)];
for j=1:length(rows)
Eim(rows(j), cols(j))=0;
end

%% put all the points that lie on the edges into list, plot histogram of the values,
take mode
both=im;
for i=1:length(rows)
Elist(i)=im(rows(i), cols(i));
both(rows(i), cols(i))=1;

```

```

end
imshow(both), title('Edges picked super-imposed on original image')
pause(.01)
xvect=0:.01:1;
% figure, plot(xvect,hist(Elist,xvect)), title('Histogram of Values on the edges picked')
hold on
% plot(mean(Elist),0:140,mean(Elist)-std(Elist),0:140,mean(Elist)+std(Elist),0:140,
mean(Elist)-2*std(Elist),0:140,mean(Elist)+2*std(Elist),0:140)
hold off
% M(1)=xvect((find(hist(Elist,xvect)==max(hist(Elist,xvect)))));
M(2)=mean(Elist);
newlist2=[];
newlist1=[];
for i=1:length(Elist)
if Elist(i)>M(2)-2*std(Elist) && Elist(i)<M(2)+2*std(Elist)
newlist2=[newlist2 Elist(i)];
end
if Elist(i)>M(2)-std(Elist) && Elist(i)<M(2)+std(Elist)
newlist1=[newlist1 Elist(i)];
end
end
M(3)=mean(newlist1);
M(4)=mean(newlist2);
newT=M(2);
% M'
end

```


APPENDIX B. IMAGE PROCESSING DETAILS FROM CHAPTER 3

B.1 Overview

MATLAB was used to calibrate the ground-truth system, reconstruct the three-dimensional locations of the coordinates in both the ground-truth and stereo-endoscope systems, and to compare the agreement between them. This appendix contains all the MATLAB code that was used. An overview of the steps used is included below. See each section for more details.

B.2 Ground-Truth System Calibration

In order to calibrate the ground-truth system, 7 calibration images of a checkerboard target were used. The calibration target was 2 mm apart in each image. The center of the white squares in the calibration images are found. The direct linear transform between 2-D and 3-D space is found using the Moore-Penrose pseudo-inverse method. The original calibration points are mapped into 3D space using this transformation and compared with the known points in order to obtain the accuracy of the transformation.

- FindCalibrationPtsAuto.m—finds the calibration points in each image and saves them. Calls on function getCalPts.m
- getCalPts.m—uses connected components to find each of the white squares in the calibration image, then finds and returns the center of each. Calls on function ThreshSlider.m
- ThreshSlider.m—creates an image with a slider bar to help the user determine the appropriate threshold to use to convert the images to black and white. A different threshold was required for each calibration image because of poor lighting and spectral reflections.
- Calibrate.m—loads the calibration points, calculates the calibration matrices, then checks the accuracy.

FindCalibrationPtsAuto.m

```
% 1.) Allows the user to crop around the calibration images to crop the image such that
%all parts of the checkerboard pattern that should be used for calibration are included,
%excluding errant reflections on the edges.
%2.) The function calls a function, getCalPts, which returns the centroid of each
%white square in the calibration image.
% 3.) The user is allowed to accept or re-do the calculation of the centroids for each
%image.

close all
clear all
clc

%% User defined variables
N=28; %Number of points to find in each image
startL=242; %frame numbers of the left and right images
endL=248;
startR=257;
endR=263;
FileDirL=['F:/.../Left/'];
FileNameL=['_DSC'];
FileDirR=['/.../'];
FileNameR=FileNameL;

for i=startL:endL
ImageName=[FileDirL FileNameL num2str(i, '%.4d') '.jpg'];
imL=imread(ImageName);
[xnew, ynew] = getCalPts(imL,i);
%     savename=['calibrationL' num2str(i)];
%     save(savename, 'xnew', 'ynew')
U1((i-startL)*N+1:(i-startL)*N+N)=xnew;
V1((i-startL)*N+1:(i-startL)*N+N)=ynew;
end

save calibrationPoints7_16_L U1 V1
```

```

close all

for i=startR:endR
    ImageName=[FileDirR FileNameR num2str(i, '%.4d') '.jpg'];
    imR=imread(ImageName);
    [xnew, ynew] = getCalPts(imR,i);
    U2((i-startR)*N+1:(i-startR)*N+N)=xnew;
    V2((i-startR)*N+1:(i-startR)*N+N)=ynew;
end

save calibrationPoints7_16_R U2 V2

```

getCalPts.m

```

% The image is converted to black and white using an user specified
% threshold. The function ThreshSlider is used to assist the user in
% selecting the appropriate threshold. The white areas are found using
% connected components. Only areas greater than a certain threshold are
% used (to eliminate noise), then the centroid of the remaining areas is
% calculated.

function [xnew, ynew] = getCalPts(im,i)

happy=0;
while happy==0
    areas=[];
    listCen=[];

    ThreshSlider(im,1)
    T=input('Which threshold should be used?');
    BW=im2bw(im,T);
    imshow(BW); axis image; title(['Click on the upper left and lower right corners where
    you would like to crop. You are on calibration target ' num2str(i)])
    [x y]=ginput(2);
    x=round(x);

```

```

y=round(y);
BWcrop=zeros(size(BW));
BWcrop(y(1):y(2),x(1):x(2))=BW(y(1):y(2),x(1):x(2));
BWcrop=logical(BWcrop);
imbw = bwareaopen(BWcrop,3.4e4);
stats = regionprops(imbw,'Centroid');
cen= cat(1,stats.Centroid);
xnew=cen(:,1);
ynew=cen(:,2);

figure, imshow(imbw)
hold on
plot(xnew, ynew, '*')
hold off

%% rearrange so that the points are in the same order as the known matrix-----
[sortednewy,indy] = sort(ynew);
sortednewx = xnew(indy,:);
a=1;
b=0;
for r=1:7
a=1+b;
if rem(r,2)
b=a+3;
else
b=a+3;
end
[sortednewx(a:b) indx]=sort(sortednewx(a:b));
sortednewyShort=sortednewy(a:b);
sortednewy(a:b)=sortednewyShort(indx,:);
end
xnew=sortednewx;
ynew=sortednewy;
%% end rearrange-----

figure, imshow(im)

```

```

hold on
plot(xnew,ynew, '*',xnew,ynew), title(['Press a key if you are happy, click the
mouse to restart this image. There are ' num2str(length(xnew)) ' points.'])
happy=waitforbuttonpress;
hold off
end

end

```

ThreshSlider.m

```

function ThreshSlider(im, calibrate)
hFig = figure('menu','none');
hAx = axes('Parent',hFig);
uicontrol('Style','slider','Value',.7,'Position',[150 5 300 20], 'Callback',
@sliderCallback);
T=.7;
if calibrate==1
imbw=im2bw(im,T);
else
imbw=~im2bw(im,T);
end
imshow(imbw,'Parent',hAx), title('Choose threshold by using slider.')

function sliderCallback(hObject, evt)
T=get(hObject, 'Value');
if calibrate==1
imbw=im2bw(im,T);
else
imbw=~im2bw(im,T);
end
imshow(imbw), title(['Threshold: ' num2str(T)])

end

```

Calibrate.m

```
%loads calibration points obtained using one of the FindCalibration codes and
%saves the L&R matrix, then checks the accuracy.
% error is calculated in mm

clear all
close all
clc
load calibrationpoints7-16-L.mat;
load calibrationpoints7-16-R.mat;

N=length(U1);
calcCen=1;
%% create the matrices of known points
% % Code for the 7/14 calibration
% knownX=[0 1 2 .5 1.5 2.5];
% knownX=[knownX knownX knownX knownX(1:3)];
% knownY=[];
% for i=0:6
%     rowVect=ones(1,3);
%     knownY=[knownY rowVect*i];
% end

%Code for the 7/16 calibration
knownX=[0 1 2 3 .5 1.5 2.5 3.5];
knownX=[knownX knownX knownX knownX(1:4)];
knownY=[];
for i=0:6
rowVect=ones(1,4);
knownY=[knownY rowVect*i];
end

knownX=knownX*6; %convert to mm
```

```

knownY=knownY*3; %convert to mm

knownZ=[];
X=[];
Y=[];
for i=0:6
X=[X knownX];
Y=[Y knownY];
rowVect=ones(1,length(knownX))*i;
knownZ=[knownZ rowVect];
end

knownZ=knownZ*2; %convert to mm
knownY=Y;
knownX=X;

known=[knownX' knownY' knownZ'];

%% calibrate to find R and L
Fl=zeros(2*N,11);
gl=zeros(2*N,1);
Fr=zeros(2*N,11);
gr=zeros(2*N,1);

for i=1:N
Fl(2*i-1,1:3)=known(i,:);
Fl(2*i-1,4)=1;
Fl(2*i-1,9:11)=-known(i, :)*U1(i);
Fl(2*i,5:7)=known(i,:);
Fl(2*i,8)=1;
Fl(2*i,9:11)=-known(i, :)*V1(i);
gl(2*i-1,1)=U1(i);
gl(2*i,1)=V1(i);
end
L=inv(Fl'*Fl)*Fl'*gl;

```

```

for i=1:N
Fr(2*i-1,1:3)=known(i,:);
Fr(2*i-1,4)=1;
Fr(2*i-1,9:11)=-known(i,)*U2(i);
Fr(2*i,5:7)=known(i,:);
Fr(2*i,8)=1;
Fr(2*i,9:11)=-known(i,)*V2(i);
gr(2*i-1,1)=U2(i);
gr(2*i,1)=V2(i);
end
R=inv(Fr'*Fr)*Fr'*gr;

save calibrationMatrix7_16 L R
%% check how good the calibration is
%find Q, q to get location of point
for i=1:N
Q=[
L(1)-L(9)*U1(i) L(2)-L(10)*U1(i) L(3)-L(11)*U1(i)
L(5)-L(9)*V1(i) L(6)-L(10)*U1(i) L(7)-L(11)*V1(i)
R(1)-R(9)*U2(i) R(2)-R(10)*U2(i) R(3)-R(11)*U2(i)
R(5)-R(9)*V2(i) R(6)-R(10)*V2(i) R(7)-R(11)*V2(i)
];
q=[
U1(i)-L(4)
V1(i)-L(8)
U2(i)-R(4)
V2(i)-R(8)
];
location(i,:)=inv(Q'*Q)*Q'*q;
end

% error=sum(sum(sqrt((known-location).^2)))/(N*3);
errorInEachCoordinate=sqrt((known-location).^2);
errorInEachPoint=sqrt(sum(errorInEachCoordinate.^2,2));
averageError=sum(errorInEachPoint)/N;
figure,

```



```

grid on
plot3(known(:,1),known(:,2),known(:,3),'*',location(:,1),location(:,2),
location(:,3),'*'), xlabel('x, mm'), ylabel('y, mm'), zlabel('z, mm'),
legend('known location of calibration points','location found with DLT from
calibration points'))

```

B.3 Ground-Truth System Reconstruction

The location of the reference points in three dimensions was found with the script trackdot3D.m.

1.) The location of reference points in each of the images was found using the script getPts.m. Using a user-selected threshold, the images are converted to black and white. The locations of the reference points each image from the left camera is found using connected components.

2.) Once the centroid of the reference points are found in each image, they are converted to three-dimensions using the mapping calculated in the calibration in the script DLT.m.

trackdot3D.m

```

% trackdot3D--program that tracks the 3D position of 1 or more points in 3D using a DLT
% Before running this program, several other steps must be completed first.
% 1.) Find calibration points. Run the program FindCalibrationPtsAuto.m
%      (or FindCalibrationPts.m--semi-automatic or manual or
%FindCalibrationSimple.m--manual only) to
%      select and save the locations of known points in space.
% 2.) Find the calibration matrices L & R. Run the program Calibrate.m,
%      which calculates and saves calibration matrices L and R based on the DLT
%algorithm.
% This program then loads calibration matrices L and R.
%
% Written by Kim Stevens, 6/25/14. Contact: kimst12@gmail.com for
% questions or comments

close all
clear all

```

```

clc

startImageL=191;
startImageR=startImageL+15;
Npoints=24;

Name='M5_mark_3';
saveName=['/.../' Name 'L_' num2str(startImageL)];
saveName2D=['/.../2D' Name 'L_' num2str(startImageL)];
FileDirL=['/.../' Name '/'];
FileDirR=['/.../' Name '/'];
FileNameL=['_DSC'];
FileNameR=FileNameL;
TL=.78;
TR=.75;
f=500;

ImageName=[FileDirL FileNameL num2str(startImageL, '%.4d') '.jpg'];
imL=(imread(ImageName));
imshow(imL)
method=input('By hand? 1 for yes, 0 for no ');
if method
Npoints=input('How many points? ');
[xl, yl]=ginput(Npoints);
else
[xl, yl] = getPts(imL,0,'left',f);
end

ImageName=[FileDirR FileNameR num2str(startImageR, '%.4d') '.jpg'];
imR=(imread(ImageName));
imshow(imR)
method=input('By hand? 1 for yes, 0 for no ');
if method
Npoints=input('How many points? ');
[xr, yr]=ginput(Npoints);
else

```

```

[xr, yr] = getPts(imR,0,'right',f);
end

%Put in clauses to ensure that there are the same number of points from
%the left and right images.
if length(xr)<length(xl)
im=imread('stop.jpg');
figure, imshow(im), title('You have more points from the left image than the right. Go
back and redo the left with fewer points.')
[xl, yl] = getPts(imL,i,'left',f);
end
if length(xr)>length(xl)
im=imread('stop.jpg');
figure, imshow(im), title('You have more points from the right image than the left. Go
back and redo the right with fewer points.')
[xr, yr] = getPts(imR,i,'right',f);
end

save(saveName2D, 'xl', 'xr', 'yl','yr')

%% convert points to 3D real space
% make sure you run the findcalibration function first, which gets the
% calibration points and saves them. Then run calibraionMatrix to get L & R
load calibrationMatrix7_14.mat
location3D=DLT(xl,yl,xr,yr,L,R);

figure, hold on
for i=1:length(xl)
plot3(location3D(i,1),location3D(i,2),location3D(i,3),'*')
end
hold off
xlabel('x'), ylabel('y'), zlabel('z'), grid on

save(saveName, 'location3D')

```

getPts.m

```
function [xnew, ynew] = getPts(im,i,LorR,f)

happy=0;
while happy==0
% image pre-processing
im=im(:,:,1);
figure(1), imshow(im), title(['Click on the upper left and lower right corners where
you would like to crop. You are on ' LorR ' image ' num2str(i+1)])
[x y]=ginput(2);
x=round(x);
y=round(y);
imcrop=uint8(ones(size(im)));
imcrop(y(1):y(2),x(1):x(2))=im(y(1):y(2),x(1):x(2));
%         figure, imshow(imcrop), title('Cropped Image');

%         imcrop=imadjust(imcrop);
%         figure, imshow(imcrop), title('Adjusted Image');

ThreshSlider(imcrop,0)
T=input('Which threshold should be used?');

imbw=im2bw(imcrop,T);
%         figure, imshow(imbw), title('black and white');

imbw=logical(imbw);
imbw=~imbw;

% get rid of specs and non-dots
imbw = bwareaopen(imbw,f);
figure(1), imshow(imbw), title('filtered. Click once to the right of each of the rows. ');

stats = regionprops(imbw, 'Area', 'Centroid');
```

```

areas = cat(1, stats.Area);
cen= cat(1,stats.Centroid);

% get rid of largest area, which comes from the cropped edges.
cen(find(max(areas)),:)=[];

xnew=cen(:,1);
ynew=cen(:,2);

%% rearrange--the purpose of this is to make sure points from the left and right images
%are in the same order. You could do some kind of matching thing to get the same result.
col1=[];
col2=[];
col3=[];
[x2,y2]=ginput(2);
c1=x2(1);
c2=x2(2);
for j=1:length(xnew)
if xnew(j)>1 && xnew(j)<c1
col1=[col1; ynew(j) xnew(j)];
elseif xnew(j)>c1 && xnew(j)<c2
col2=[col2; ynew(j) xnew(j)];
else
col3=[col3; ynew(j) xnew(j)];
end
end
col1=sortrows(col1,1);
col2=sortrows(col2,1);
col3=sortrows(col3,1);
xnew=[col1(:,2); col2(:,2); col3(:,2)];
ynew=[col1(:,1); col2(:,1); col3(:,1)];
%% end rearrange-----
if strcmp(LorR,'left')
figure(3)
else
figure(4)

```

```

end
imshow(imbw)
hold on
plot(xnew,ynew,'*',xnew,ynew), title(['Press a key if you are happy, click the
mouse to restart this image. There are ' num2str(length(xnew)) ' points.']), xlabel(['You
happy=waitforbuttonpress;
hold off
if happy
%         if length(xnew) > Npoints
skip=input('Enter any points you would like to skip. You may enter multiple
points, but separate them by a space, and list them from largest to smallest. ','s');
skip=str2num(skip);
for i=1:length(skip)
xnew(skip(i))=[];
ynew(skip(i))=[];
end
imshow(imbw)
hold on
plot(xnew,ynew,'*',xnew,ynew), title(['Press a key if you are happy, click the
mouse to restart this image. There are ' num2str(length(xnew)) ' points.']), xlabel(['You
happy=waitforbuttonpress;
hold off
end
end
end

```

DLT.m

```

function [ answer ] = DLT(U1,V1,U2,V2,L,R)
%DLT converts x and y points in picture space from 2 cameras into 3D space
%using the calibration matrices L&R which are obtained from the Calibrate
%function

numpts=length(U1);
for i=1:numpts

```

```

Q=[
L(1)-L(9)*U1(i) L(2)-L(10)*U1(i) L(3)-L(11)*U1(i)
L(5)-L(9)*V1(i) L(6)-L(10)*U1(i) L(7)-L(11)*V1(i)
R(1)-R(9)*U2(i) R(2)-R(10)*U2(i) R(3)-R(11)*U2(i)
R(5)-R(9)*V2(i) R(6)-R(10)*V2(i) R(7)-R(11)*V2(i)
];
q=[
U1(i)-L(4)
V1(i)-L(8)
U2(i)-R(4)
V2(i)-R(8)
];
locationpt(i,:) = inv(Q'*Q)*Q'*q;
end
answer=locationpt;
end

```

B.4 Stereo-endoscope Reconstruction

The location of the reference points in three dimensions was found with the script `trackdot3DStereo.m`.

1.) The location of reference points in each of the left images manually because the resolution of the images and poor lighting prevented automatic selection as in the ground-truth system. The location of each point in the left image is matched to the corresponding point in the right image using a cross-correlation in `XCorrPts.m`. Sub-pixel accuracy is obtained by fitting a Gaussian 3-pt curve to the cross-correlation.

2.) Once the centroid of the reference points are found in each image, they are converted to three-dimensions using the script `ReconstructStereoKS.m`.

B.4.1 `trackdot3DStereo.m`

```

close all
clear all

```

```

clc

Name='m5_d.116000001';
FileDir=['/.../' ];
saveName=[FileDir Name];
saveName2D=[FileDir '2D' Name];
SLR2DL='/.../2DM5_mark_2L_168';
SLR2DR='/.../2DM5_mark_2_168';
SLR_Lim='/.../M5_mark_2/_DSC0168.jpg';
SLR_Rim='/.../M5_mark_2/_DSC0183.jpg';

load(SLR2DL);
imshow(imread(SLR_Lim))
hold on
plot(xl,yl,'*')
load(SLR2DR);
plot(xl,yl,'*')
hold off

% subplot(212), imshow(imread(SLR_Rim))
% subplot(212), plot(xr,yr,'*')
% subplot(212), plot(xr,yr,'*')

f=25; %filter size--how small of areas do you want to not consider?

ImageName=[FileDir Name '.tif'];
im=(imread(ImageName));

method=1;
% method=input('By hand? 1 for yes, 0 for no ');
if method
Npoints=input('How many points? ');
figure, imshow(im)
title(['pick ' num2str(Npoints) ' on the left. (In the same order as the SLRs)'])
[xl, yl]=ginput(Npoints);
title(['pick the same ' num2str(Npoints) ' on the right, in the same order.'])

```



```

[xr, yr]=ginput(Npoints);

[ Xint,Yint,X,Y ] = XCorrPts( im,xl,xr,yl,yr );
figure, imshow(im)
hold on
plot(xl,yl,'r*',xr,yr,'r*',Xint,Yint,'g*',X,Y,'b*'), legend('left', 'by
hand','matched','matched sub-pixel')
hold off
xr=X';
yr=Y';

else
[xl, yl] = getPts(im,0,'left',f);
[xr, yr] = getPts(im,0,'right',f);
end

save(saveName2D, 'xl', 'xr', 'yl','yr')

%% convert points to 3D real space
[Stereox Stereoy Stereoz]=ReconstructStereoKS([xl yl xr yr], zeros(2), zeros(2));

figure, plot3(Stereox,Stereoy,Stereoz,'*'),xlabel('x'), ylabel('y'), zlabel('z'),
grid on
save(saveName, 'StereoX', 'Stereoy', 'Stereoz')

```

B.4.2 XCorrPts.m

```

function [ Xint,Yint,X,Y ] = XCorrPts( im,xl,xr,yl,yr )

% User defined variables
intwindx=64; %choose the interrogation window size in pixels
intwindy=64;

xr=round(xr);
xl=round(xl);

```

```

yr=round(yr);
yl=round(yl);

for i=1:length(xl)
imL=im(yl(i)-intwindy/2:yl(i)+intwindy/2,xl(i)-intwindx/2:xl(i)+intwindx/2);
imR=im(yr(i)-intwindy/2:yr(i)+intwindy/2,xr(i)-intwindx/2:xr(i)+intwindx/2);

phi=fftshift(iff2(fft2(imL).*conj(fft2(imR))) ); %use here the cross correlation
%of the fft; but you could easily use something more simple
[npeakint,mpeakint] = find(max(max(phi))==phi);

%pick just one in case there are multiple peaks
npeakint = npeakint(1);
mpeakint = mpeakint(1);

%convert into x/y coord
xint=intwindx+1-mpeakint;
yint=intwindy+1-npeakint;

%calculate subpixel accuracy
mstar = (log(phi(npeakint,mpeakint+1)) -
log(phi(npeakint,mpeakint-1)))/(4*log(phi(npeakint,mpeakint)) -
2*log(phi(npeakint,mpeakint-1)) - 2*log(phi(npeakint,mpeakint+1)));
nstar = (log(phi(npeakint+1,mpeakint)) -
log(phi(npeakint-1,mpeakint)))/(4*log(phi(npeakint,mpeakint)) -
2*log(phi(npeakint-1,mpeakint)) - 2*log(phi(npeakint+1,mpeakint)));
mpeak = mpeakint + mstar;
npeak = npeakint + nstar;

%convert into x/y coord
x=intwindx+1-mpeak;
y=intwindy+1-npeak;

% figure,
% subplot(221), imshow(imL), title('left'), grid on
% hold on

```

```

% plot(intwindx/2+1,intwindx/2+1,'r*')
% hold off
% subplot(222), imshow(imR), title('right'), grid on
% hold on
% plot(xint, yint, 'g*', x, y, 'b*')
% plot(intwindx/2+1,intwindy/2+1,'r*')
% hold off
% subplot(223), mesh(phi), xlabel('m'), ylabel('n'), shading interp
% hold on
% plot3(mpeakint, npeakint, max(max(phi)), 'g*', mpeak, npeak, max(max(phi)), 'b*')
% hold off
% subplot(224), axis square, pcolor(phi), xlabel('m'), ylabel('n'), shading interp
% hold on
% plot(mpeakint, npeakint, 'g*')
% hold off
%
% figure, surf(phi), xlabel('m'), ylabel('n'), shading interp
% hold on
% plot3(mpeakint, npeakint, max(max(phi)), 'g*', mpeak, npeak, max(max(phi)), 'b*')
% hold off

%convert back into global coordinates
Xint(i)=xint+xr(i)-intwindx/2;
Yint(i)=yint+yr(i)-intwindy/2;
X(i)=x+xr(i)-intwindx/2;
Y(i)=y+yr(i)-intwindy/2;

% figure, imshow(im);
% hold on
% plot(Xint(i), Yint(i), 'g*', X(i), Y(i), 'b*')
% hold off
% waitforbuttonpress
end
end

```

B.4.3 ReconstructStereoKS.m

```

function [estimate_Xp estimate_Yp estimate_Zp] =
ReconstructStereoKS(Iresult, coord_l, coord_r)
Nfeat=size(Iresult,1);

estimate_Xp = zeros(Nfeat,1);
estimate_Yp = zeros(Nfeat,1);
estimate_Zp = zeros(Nfeat,1);

%%%%%%%%%%%%%%%%%%%%%%%%%%%%%%%%%%%%%%%%%%%%%%%%%%%%%%%%%%%%%%%%%%%%%%%%

K1 = 3.19748609652514E-04;
K2 = -3.24774404879771E-03;
K3 = 1.71312215887679E-03;
K4 = -2.06852241297674;
K5 = 1.72418519136038E-03;
K6 = -5.08296987326447E-02;

C1 = 0.00014;
C2 = -0.0023;
C3 = 0.000062;
C4 = 0.0026;

LOriginX = 160.5;
LOriginY = 141;
ROriginX = 534;
ROriginY = 139;

cn = 1;
for n = 1:Nfeat,

XL = coord_l(1,1)+double(Iresult(n,1));
YL = coord_l(1,2)+double(Iresult(n,2));
XR = coord_r(1,1)+double(Iresult(n,3));
YR = coord_r(1,2)+double(Iresult(n,4));

DL = XL - LOriginX;
DR = XR - ROriginX;

```

```

Dv = -((YL + YR) / 2 - LOriginY);
Dv = -(YL - LOriginY);

estimate_Zp(cn) = 1/(K1*((DL-DR)+C1*DL*DL+C2*DL+C3*Dv*Dv+C4*Dv)+K2);
estimate_Xp(cn) = K3 * (estimate_Zp(cn) * DL) + K4;
estimate_Yp(cn) = K5 * (estimate_Zp(cn) * Dv) + K6;
cn = cn+1;

end
end

```

B.5 Comparison Between Stereo-endoscope and Ground-truth Systems

In order to compare between the stereo-endoscope and ground-truth systems, the origins of the coordinate frames from each system were shifted to the centroid of the reference points. Each frame was then rotated to be in line with the anatomical coordinate systems.

Compare.m

```

close all
clear all
clc
%user input
NameStereo='m5_d.115000001';
numSLR_L=165;
numSLR_R=180;

Stereo3D=['F:/.../' NameStereo];
Stereo2D=['F:/.../2D' NameStereo];
FileDir=['F:/.../' ];
startPt=1;
endPt=8;
SLR3D=['F:/.../M5_mark_2L-' num2str(numSLR_L)];
SLR2D=['F:/.../2DM5_mark_2L-' num2str(numSLR_L)];

```

```

SLR_Lim=['F:/.../_DSC0' num2str(numSLR_L) '.jpg'];
SLR_Rim=['F:/.../_DSC0' num2str(numSLR_R) '.jpg'];

ImageName=[FileDir NameStereo '.tif'];
im=(imread(ImageName));
load(Stereo3D)
load(Stereo2D)

StereoX=StereoX(startPt:endPt);
StereoY=StereoY(startPt:endPt);
StereoZ=StereoZ(startPt:endPt);

%shift the coordinates so the first point is at the origin
StereoX=StereoX-StereoX(1);
StereoY=StereoY-StereoY(1);
StereoZ=StereoZ-StereoZ(1);

StereoX=StereoX-mean(StereoX);
StereoY=StereoY-mean(StereoY);
StereoZ=StereoZ-mean(StereoZ);

%load SLR data
location3D=load (SLR3D);
%shift so that the first point has the origin located at zero. Also flip
%the y axis so that it matches the stereo coordinate system.
SLRx=location3D.location3D(:,1)-location3D.location3D(1,1);
SLRy=-location3D.location3D(:,2)+location3D.location3D(1,2);
SLRz=location3D.location3D(:,3)-location3D.location3D(1,3);

%shift so that the centroid is located at the origin. Also flip
%the y axis so that it matches the stereo coordinate system.
SLRx=location3D.location3D(:,1)-mean(location3D.location3D(:,1));
SLRy=-location3D.location3D(:,2)+mean(location3D.location3D(:,2));
SLRz=location3D.location3D(:,3)-mean(location3D.location3D(:,3));

```

```

%plot the 2D coordinates from the stereo-endoscope
figure,
subplot(233), imshow(im)
hold on
plot(xl(startPt:endPt),yl(startPt:endPt),'*'),xr(startPt:endPt),yr(startPt:endPt),'*')
hold off

%plot the 2D coordinates from the SLR cameras
load(SLR2D);
subplot(231), imshow(imread(SLR_Lim))
hold on
plot(xl,yl,'*')
hold off
subplot(232), imshow(imread(SLR_Rim))
hold on
plot(xr,yr,'*')
hold off

subplot(234), plot3(SLRx,SLRy,SLRz,'*'), xlabel('x'), ylabel('y'), zlabel('z'),
grid on, title('SLR')

subplot(235), plot3(Stereox,Stereoy,Stereoz,'*'), xlabel('x'), ylabel('y'),
zlabel('z'), grid on, title('Stereo-endoscope')

subplot(236), plot3(SLRx,SLRy,SLRz,'*',Stereox,Stereoy,Stereoz,'*'), xlabel('x'),
ylabel('y'), zlabel('z'), grid on, legend('SLR','Stereo-endoscope')

% calculate difference
SLR=[SLRx SLRy SLRz];
Stereo=[StereoX StereoY StereoZ];
errorInEachCoordinate=sqrt((SLR-Stereo).^2);
averageerrorInX=mean(errorInEachCoordinate(:,1))
averageerrorInY=mean(errorInEachCoordinate(:,2))
averageerrorInZ=mean(errorInEachCoordinate(:,3))
errorInEachPoint=sqrt(sum(errorInEachCoordinate.^2,2));
averageError=sum(errorInEachPoint)/length(SLR)

```

```

result(1,1:4)=[averageerrorInX averageerrorInY averageerrorInZ averageError];

%% rotate points about the y axis so the z-points are in the same plane.
%PROCEDURE
% Create a line in the anterior-posterior direction
% Create a line in the medial lateral direction, using the 3 most anterior
% points
% Use these two lines to create a plane
% Define an angle for this plane
% Create a rotation matrix to rotate the planes to be normal to z direction

% FOR SLRS
% % Set1--if 8 points in first column
% [m,p,s] = best_fit_line(SLRx(1:8),SLRy(1:8),SLRz(1:8));
% [pt1]= m+p*5;
% [pt2]= m+p*-10;
% [m,p,s] = best_fit_line([SLRx(1) SLRx(9) SLRx(17)]',[SLRy(1) SLRy(9)
%SLRy(17)]',[SLRz(1) SLRz(9) SLRz(17)]');
% [pt3]= m+p*5;
% [pt4]= m+p*-10;
% thetaSLR=-atan((pt3(3)-pt4(3))/(pt3(1)-pt4(1)));
% RSLR=[cos(thetaSLR) 0 -sin(thetaSLR); 0 1 0; sin(thetaSLR) 0 cos(thetaSLR)];
% figure,
% subplot(221), plot3(SLRx,SLRy,SLRz,'*',[pt1(1) pt2(1)],[pt1(2) pt2(2)],[pt1(3)
%pt2(3)],[pt3(1) pt4(1)],[pt3(2) pt4(2)],[pt3(3) pt4(3)]), xlabel('x'),
%ylabel('y'), zlabel('z'), grid on, title('SLR-original')

%Set2--if 7 points in first column
% [m,p,s] = best_fit_line(SLRx(1:7),SLRy(1:7),SLRz(1:7));
% [pt1]= m+p*5;
% [pt2]= m+p*-10;
% [m,p,s] = best_fit_line([SLRx(1) SLRx(8) SLRx(13)]',[SLRy(1) SLRy(8)
%SLRy(13)]',[SLRz(1) SLRz(8) SLRz(13)]');
% [pt3]= m+p*5;
% [pt4]= m+p*-10;
% thetaSLR=-atan((pt3(3)-pt4(3))/(pt3(1)-pt4(1)));

```



```

% RSLR=[cos(thetaSLR) 0 -sin(thetaSLR); 0 1 0; sin(thetaSLR) 0 cos(thetaSLR)];
% figure,
% subplot(221), plot3(SLRx,SLRy,SLRz,'*',[pt1(1) pt2(1)],[pt1(2) pt2(2)],[pt1(3)
%pt2(3)], [pt3(1) pt4(1)],[pt3(2) pt4(2)],[pt3(3) pt4(3)]), xlabel('x'),
%ylabel('y'), zlabel('z'), grid on, title('SLR-original')

% %Set3--for 2 & 3 left (Stereo images 115 and 116)
% [m,p,s] = best_fit_line(SLRx(1:8),SLRy(1:8),SLRz(1:8));
% [pt1]= m+p*5;
% [pt2]= m+p*-10;
% thetaSLR=-atan(pt2(3)-pt1(3)/(pt2(1)-pt1(1)))
% RSLR=[cos(thetaSLR) 0 -sin(thetaSLR); 0 1 0; sin(thetaSLR) 0 cos(thetaSLR)];
% figure,
% subplot(221), plot3(SLRx,SLRy,SLRz,'*',[pt1(1) pt2(1)],[pt1(2) pt2(2)],[pt1(3)
%pt2(3)]), xlabel('x'), ylabel('y'), zlabel('z'), grid on, title('SLR-original')

% Set 4
[m,p,s] = best_fit_line(SLRx,SLRy,SLRz);
[pt1]= m+p*15;
[pt2]= m+p*-15;
thetaSLR=-atan((pt2(3)-pt1(3))/(pt2(1)-pt1(1)))
RSLR=[cos(thetaSLR) 0 -sin(thetaSLR); 0 1 0; sin(thetaSLR) 0 cos(thetaSLR)];
figure,
subplot(221), plot3(SLRx,SLRy,SLRz,'*',[pt1(1) pt2(1)],[pt1(2) pt2(2)],[pt1(3)
pt2(3)]), xlabel('x'), ylabel('y'), zlabel('z'), grid on, title('SLR-original')

% FOR STEREO-ENDOSCOPE
%set1
% [m,p,s] = best_fit_line(Stereox(1:8),Stereoy(1:8),Stereozy(1:8));
% [pt1]= m+p*5;
% [pt2]= m+p*-10;
% [m,p,s] = best_fit_line([Stereoxy(1) Stereoxy(9) Stereoxy(17)]',[Stereoy(1)
%Stereoy(9) Stereoy(17)]',[Stereozy(1) Stereozy(9) Stereozy(17)]');
% [pt3]= m+p*5;
% [pt4]= m+p*-10;

```

```

% thetaStereo=-atan((pt3(3)-pt4(3))/(pt3(1)-pt4(1)));
% RStereo=[cos(thetaStereo) 0 -sin(thetaStereo); 0 1 0; sin(thetaStereo) 0
%cos(thetaStereo)];
% subplot(222), plot3(Stereox,Stereoy,Stereoz,'*', [pt1(1) pt2(1)], [pt1(2)
%pt2(2)], [pt1(3) pt2(3)], [pt3(1) pt4(1)], [pt3(2) pt4(2)], [pt3(3) pt4(3)]),
%xlabel('x'), ylabel('y'), zlabel('z'), grid on, title('SLR'),
%title('Stereo-original')

%set2
% [m,p,s] = best_fit_line(Stereox(1:7),Stereo(1:7),Stereo(1:7));
% [pt1]= m+p*5;
% [pt2]= m+p*-10;
% [m,p,s] = best_fit_line([Stereo(1) Stereo(8) Stereo(13)]', [Stereo(1)
%Stereo(8) Stereo(13)]', [Stereo(1) Stereo(8) Stereo(13)]');
% [pt3]= m+p*5;
% [pt4]= m+p*-10;
% thetaStereo=-atan((pt3(3)-pt4(3))/(pt3(1)-pt4(1)));
% RStereo=[cos(thetaStereo) 0 -sin(thetaStereo); 0 1 0; sin(thetaStereo) 0
%cos(thetaStereo)];
% subplot(222), plot3(Stereox,Stereoy,Stereoz,'*', [pt1(1) pt2(1)], [pt1(2)
%pt2(2)], [pt1(3) pt2(3)], [pt3(1) pt4(1)], [pt3(2) pt4(2)], [pt3(3) pt4(3)]),
%xlabel('x'), ylabel('y'), zlabel('z'), grid on, title('SLR'),
%title('Stereo-original')

% %Set3--for 2 & 3 left (Stereo images 115 and 116)
% [m,p,s] = best_fit_line(Stereox(1:8),Stereo(1:8),Stereo(1:8));
% [pt1]= m+p*5;
% [pt2]= m+p*-10;
% thetaStereo=-atan(pt2(3)-pt1(3)/(pt2(1)-pt1(1)))
% RStereo=[cos(thetaStereo) 0 -sin(thetaStereo); 0 1 0; sin(thetaStereo) 0
%cos(thetaStereo)];
% subplot(222), plot3(Stereox,Stereoy,Stereoz,'*', [pt1(1) pt2(1)], [pt1(2)
%pt2(2)], [pt1(3) pt2(3)]), xlabel('x'), ylabel('y'), zlabel('z'), grid on,
%title('Stereo-original')

% Set 4

```

```

[m,p,s] = best_fit_line(Stereox,Stereoy,Stereoz);
[pt1]= m+p*5;
[pt2]= m+p*-10;
thetaStereo=-atan((pt1(3)-pt2(3))/(pt1(1)-pt2(1)))
RStereo=[cos(thetaStereo) 0 -sin(thetaStereo); 0 1 0; sin(thetaStereo) 0
cos(thetaStereo)];
subplot(222), plot3(Stereox,Stereoy,Stereoz,'*', [pt1(1) pt2(1)], [pt1(2)
pt2(2)], [pt1(3) pt2(3)]), xlabel('x'), ylabel('y'), zlabel('z'), grid on,
title('Stereo-original')

for i=1:length(Stereox)
row=[Stereox(i) Stereoy(i) Stereoz(i)];
Stereo(i,:)=RStereo*row';
row=[SLRx(i) SLRy(i) SLRz(i)];
SLR(i,:)=RSLR*row';
end

errorInEachCoordinate=sqrt((SLR-Stereo).^2);
averageerrorInX=mean(errorInEachCoordinate(:,1))
averageerrorInY=mean(errorInEachCoordinate(:,2))
averageerrorInZ=mean(errorInEachCoordinate(:,3))
errorInEachPoint=sqrt(sum(errorInEachCoordinate.^2,2));
averageError=sum(errorInEachPoint)/length(SLR)
averageError=sqrt(averageerrorInX^2+averageerrorInY^2+averageerrorInZ^2)
subplot(223), plot3(SLR(:,1),SLR(:,2),SLR(:,3),'*'), xlabel('x'), ylabel('y'),
zlabel('z'), grid on, title('SLR-rotated')
subplot(224), plot3(Stereo(:,1),Stereo(:,2),Stereo(:,3),'*'), xlabel('x'),
ylabel('y'), zlabel('z'), grid on, title('Stereo-rotated')

figure, plot3(SLR(:,1),SLR(:,2),SLR(:,3),'*',Stereo(:,1),Stereo(:,2),Stereo(:,3),'*'),
xlabel('x (mm)'), ylabel('y (mm)'), zlabel('z (mm)'), grid on, legend('SLR',
'Stereo'), title('Rotated points')

result(2,1:4)=[averageerrorInX averageerrorInY averageerrorInZ averageError];
save(['resultL' NameStereo])

```

APPENDIX C. MATLAB CODE FROM CHAPTER 4

C.1 Overview

MATLAB was used for the image processing, strain, and Poisson's ratio calculations in this chapter. FindWidths.m called on XCorrPtsPoisson.m to find the lengths and widths of the images at each point, using cross-correlation and simple thresholding. Poisson.m calculates Poisson's ratio in the four ways described in the chapter, using Smooth.m to fit the data to a line. Compare.m fits averages the the resulting Poisson's ratio curves into one and fits them to a 2nd order polynomial.

C.2 XCorrPtsPoisson.m

```
function [ Xint,Yint,X,Y ] = XCorrPtsPoisson( imold,imnew,x,yold,ynew )

% User defined variables
intwindx=600; %choose the interrogation window size in pixels
intwindy=300;

x=round(x);
ynew=round(ynew);
yold=round(yold);

for i=1:length(x)
imold=imold(yold-intwindy/2:yold+intwindy/2,x-intwindx/2:x+intwindx/2);
imnew=imnew(ynew-intwindy/2:ynew+intwindy/2,x-intwindx/2:x+intwindx/2);

phi=fftshift(iff2( fft2(imold).*conj(fft2(imnew))) );
[npeakint,mpeakint] = find(max(max(phi))==phi);
```

```

%pick just one in case there are multiple peaks
npeakint = npeakint(1);
mpeakint = mpeakint(1);

%convert into x/y coord
xint=intwindx+1-mpeakint;
yint=intwindy+1-npeakint;

%calculate subpixel accuracy
mstar = (log(phi(npeakint,mpeakint+1)) - log(phi(npeakint,mpeakint-1)))/
(4*log(phi(npeakint,mpeakint)) - 2*log(phi(npeakint,mpeakint-1)) -
2*log(phi(npeakint,mpeakint+1)));
nstar = (log(phi(npeakint+1,mpeakint)) - log(phi(npeakint-1,mpeakint)))/
(4*log(phi(npeakint,mpeakint)) - 2*log(phi(npeakint-1,mpeakint)) -
2*log(phi(npeakint+1,mpeakint)));
mpeak = mpeakint + mstar;
npeak = npeakint + nstar;

%convert into x/y coord
x=intwindx+1-mpeak;
y=intwindy+1-npeak;

%convert back into global coordinates
Xint(i)=xint+x(i)-intwindx/2;
Yint(i)=yint+ynew(i)-intwindy/2;
X(i)=x+x(i)-intwindx/2;
Y(i)=y+ynew(i)-intwindy/2;

% figure, imshow(im);
% hold on
% plot(Xint(i),Yint(i),'g*',X(i),Y(i),'b*')
% hold off
% waitforbuttonpress
% close
end
end

```

C.3 FindWidths.m

```
%This program is designed to step through a series of images of silicone  
%tensile samples, finding the length and width of each sample.
```

```
close all  
clear all  
clc  
warning('off', 'Images:initSize:adjustingMag');  
  
FileDir=('F:\...\');  
savename='EF1a';  
if savename=='DS1a'  
startpt=2;  
endpt=65;  
elseif savename=='EF1a'  
startpt=67;  
endpt=131;  
elseif savename=='EF2a'  
startpt=133;  
endpt=197;  
elseif savename=='EF4a'  
startpt=199;  
endpt=263;  
elseif savename=='EF6a'  
startpt=265;  
endpt=329;  
elseif savename=='EF8a'  
startpt=331;  
endpt=395;  
elseif savename=='DS1b'  
startpt=397;  
endpt=461;  
elseif savename=='EF1b'  
startpt=463;
```

```

endpt=527;
elseif savename=='EF2b'
startpt=529;
endpt=593;
elseif savename=='EF4b'
startpt=595;
endpt=659;
elseif savename=='EF6b'
startpt=661;
endpt=725;
elseif savename=='EF8b'
startpt=727;
endpt=791;
end
center=0;
for i= startpt : endpt
ImageName=[FileDir num2str(i) '.tif'];
A=imread(ImageName);
A=imrotate(A,2,'bilinear','crop');

%convert to greyscale to speed up operations
A=rgb2gray(A);

%Start at a point within the sample
x=1765;

if i==startpt
imshow(A), title('click at the top, then the bottom')
[junk, y]=ginput(2);
y1=y(1);
y2=y(2);

Aorig=A;
y1Orig=y1;
else
%find upper point for subsequent points

```

```

[ Xint,Yint,X,Y ] = XCorrPtsPoisson( Aorig,A,x,y1Orig,y1 );
y1=Yint;
end

%calculate the center point
leng(i)=y2-y1;
center(i)=y1+(leng(i)/2);

%find the edges
subset=A(round(center(i))-700:round(center(i))+700,1:size(A,2));
B=im2bw(subset,80/255);
numdiv=200;
space=round(1400/numdiv);
%    figure(2), imshow(B)
for j=1:numdiv-1
x1(j)=x;
ycord=space*j;
while B(ycord,x1(j))==1
x1(j)=x1(j)+1;
end
x2(j)=x;
while B(ycord,x2(j))==1
x2(j)=x2(j)-1;
end
%    hold on
%    plot(x1(j),ycord,'o',x2(j),ycord,'o')
end
x1avg(i)=mean(x1);
x2avg(i)=mean(x2);

%calculate the width of the sample
wid(i)=x1avg(i)-x2avg(i);
figure(1),
imshow(A);
hold on
plot(x,y1,'^',x,y2,'^',x1avg,center,'o',x2avg,center,'o');

```



```

hold off
end

wid=wid(startpt:endpt);
leng=leng(startpt:endpt);
figure, plot(wid), xlabel('image #'), ylabel('width, pixels')
figure, plot(leng), xlabel('image #'), ylabel('length, pixels')
save(savename)

```

C.4 Smooth.m

```

function [ yfit ] = Smooth( x,y )
%SMOOTH accepts a function y=f(x) and returns a linear function yfit=f(x)
%using Matlab's linear regression algorithm.

%smooth butterworth
fs=65;
w=10/(.5*fs); %the numerator is the cutoff frequency
[b,c]=butter(2,w);
lengB=filtfilt(b,c,y);

% linear regression:
p=polyfit(x,y,1);
yfit=polyval(p,x);
yresid=y-yfit;
SSresid=sum(yresid.^2);
SStotal=(length(y)-1)*var(y);
rsq=1-SSresid/SStotal;

% figure, plot(1:length(leng),lengB,1:length(leng),lengyfit,1:length(leng),wid)
% legend('butterworth','linear regression','original')

end

```

C.5 Poisson.m

```
function [ vTot,vInt,eyLog ] = Poisson( name )

load(name)

leng=Smooth(1:length(leng),leng);
wid=Smooth(1:length(wid),wid);

%paper
% wid=[10:-.002:9.98 9.98:-.006:9.92];
% leng=[10:.001:10.01 10.01:.0015:10.025];

eyEng=(leng-leng(1))/leng(1);
exEng=(wid-wid(1))/wid(1);
vEng=-exEng./eyEng;

eyLog=log(1+eyEng);
exLog=log(1+exEng);
vLog=-exLog./eyLog;

eyTot(1)=0;
exTot(1)=0;
for i=2:length(leng)
eyInt(i)=(leng(i)-leng(i-1))/leng(i-1);
exInt(i)=(wid(i)-wid(i-1))/wid(i-1);
eyTot(i)=eyTot(i-1)+eyInt(i);
exTot(i)=exTot(i-1)+exInt(i);
end

vTot=-exTot./eyTot;
vInt=-exInt./eyInt;

end
```

C.6 Compare.m

```
close all
clear all
clc

[ vTotDS1a,vIntDS1a,eylogDS1a ] = Poisson('DS1a');
[ vTotDS1b,vIntDS1b,eylogDS1b ] = Poisson('DS1b');
[ vTotEF1a,vIntEF1a,eylogEF1a ] = Poisson('EF1a');
[ vTotEF1b,vIntEF1b,eylogEF1b ] = Poisson('EF1b');
[ vTotEF2a,vIntEF2a,eylogEF2a ] = Poisson('EF2a');
[ vTotEF2b,vIntEF2b,eylogEF2b ] = Poisson('EF2b');
[ vTotEF4a,vIntEF4a,eylogEF4a ] = Poisson('EF4a');
[ vTotEF4b,vIntEF4b,eylogEF4b ] = Poisson('EF4b');
[ vTotEF6a,vIntEF6a,eylogEF6a ] = Poisson('EF6a');
[ vTotEF6b,vIntEF6b,eylogEF6b ] = Poisson('EF6b');
[ vTotEF8a,vIntEF8a,eylogEF8a ] = Poisson('EF8a');
[ vTotEF8b,vIntEF8b,eylogEF8b ] = Poisson('EF8b');

%% Figure out what fit
p2=polyfit(eylogDS1a(2:end),vTotDS1a(2:end),2);
yfit2=polyval(p2,eylogDS1a);
p3=polyfit(eylogDS1a(2:end),vTotDS1a(2:end),3);
yfit3=polyval(p3,eylogDS1a);
figure, plot(eylogDS1a,vTotDS1a,eylogDS1a,yfit2,eylogDS1a,yfit3);
legend('Original','2nd order','3rd order')

%% Average over all except 1:1:8
yfit1=polyval(polyfit(eylogDS1a(2:end),vTotDS1a(2:end),2),eylogEF1a);
yfit2=polyval(polyfit(eylogDS1b(2:end),vTotDS1b(2:end),2),eylogEF1a);
yfit3=polyval(polyfit(eylogEF1a(2:end),vTotEF1a(2:end),2),eylogEF1a);
yfit4=polyval(polyfit(eylogEF1b(2:end),vTotEF1b(2:end),2),eylogEF1a);
yfit5=polyval(polyfit(eylogEF2a(2:end),vTotEF2a(2:end),2),eylogEF1a);
yfit6=polyval(polyfit(eylogEF2b(2:end),vTotEF2b(2:end),2),eylogEF1a);
yfit7=polyval(polyfit(eylogEF4a(2:end),vTotEF4a(2:end),2),eylogEF1a);
```

```

yfit8=polyval(polyfit(eylogEF4b(2:end),vTotEF4b(2:end),2),eylogEF1a);
yfit9=polyval(polyfit(eylogEF6a(2:end),vTotEF6a(2:end),2),eylogEF1a);
yfit10=polyval(polyfit(eylogEF6b(2:end),vTotEF6b(2:end),2),eylogEF1a);
meanFunc=(yfit1+yfit2+yfit3+yfit4+yfit5+yfit6+yfit7+yfit8+yfit9+yfit10)/10;

%% fit curve to average
p=polyfit(eylogEF1a,meanFunc,2);
figure, plot(eylogEF1a,meanFunc,eylogEF1a,polyval(p,eylogEF1a))
xlabel('Longitudinal True Strain (\epsilon_y^{\log})','FontSize',10,'FontName','Times')
ylabel('\nu_{tot}','FontSize',10,'FontName','Times')
legend('Average of all curves','2nd order polynomial fit to average')

%% plot ratio
figure,
subplot(211), plot(eylogDS1a,vTotDS1a,eylogEF1a,vTotEF1a,eylogEF2a,vTotEF2a,eylogEF4a,
vTotEF4a,eylogEF6a,vTotEF6a,eylogEF8a,vTotEF8a,eylogEF1a,polyval(p,eylogEF1a),'k')
xlabel('Longitudinal True Strain (\epsilon_y^{\log})','FontSize',10,'FontName','Times')
ylabel('\nu_{tot}','FontSize',10,'FontName','Times')
legend('DS1a','EF1a','EF2a','EF4a','EF6a','EF8a','Average','Location','EastOutside')
set(gca,'FontSize',10,'FontName','Times');

subplot(212), plot(eylogDS1b,vTotDS1b,eylogEF1b,vTotEF1b,eylogEF2b,vTotEF2b,eylogEF4b,
vTotEF4b,eylogEF6b,vTotEF6b,eylogEF8b,vTotEF8b,eylogEF1a,polyval(p,eylogEF1a),'k')
xlabel('Longitudinal True Strain (\epsilon_y^{\log})','FontSize',10,'FontName','Times')
ylabel('\nu_{tot}','FontSize',10,'FontName','Times')
legend('DS1b','EF1b','EF2b','EF4b','EF6b','EF8b','Average','Location','EastOutside')
set(gca,'FontSize',10,'FontName','Times');

set(gcf,'PaperPosition',[1 1 5 6]); % ?? width height (inches)
hold(gca,'all');
print('-dpng','-r300','ratio.png');

%% plot aAndb
figure,
subplot(321), plot(eylogDS1a,vTotDS1a,'k',eylogDS1b,vTotDS1b,'--k')
legend('DS1a','DS1b','Location','NorthWest')

```

```

ylim([.32 .55])
xlim([0 .4])
set(gca, 'FontSize', 10, 'FontName', 'Times');

subplot(322), plot(eylogEF1a, vTotEF1a, 'k', eylogEF1b, vTotEF1b, '--k')
legend('EF1a', 'EF1b', 'Location', 'NorthWest')
ylim([.32 .55])
xlim([0 .4])
set(gca, 'FontSize', 10, 'FontName', 'Times');

subplot(323), plot(eylogEF2a, vTotEF2a, 'k', eylogEF2b, vTotEF2b, '--k')
legend('EF2a', 'EF2b', 'Location', 'NorthWest')
ylim([.32 .55])
xlim([0 .4])
set(gca, 'FontSize', 10, 'FontName', 'Times');

subplot(324), plot(eylogEF4a, vTotEF4a, 'k', eylogEF4b, vTotEF4b, '--k')
legend('EF4a', 'EF4b', 'Location', 'NorthWest')
ylim([.32 .55])
xlim([0 .4])
set(gca, 'FontSize', 10, 'FontName', 'Times');

subplot(325), plot(eylogEF6a, vTotEF6a, 'k', eylogEF6b, vTotEF6b, '--k')
legend('EF6a', 'EF6b', 'Location', 'NorthWest')
ylim([.32 .55])
xlim([0 .4])
set(gca, 'FontSize', 10, 'FontName', 'Times');
xlabel('Longitudinal True Strain ( $\epsilon_y^{\log}$ )', 'FontSize', 10, 'FontName', 'Times')
ylabel('\nu_{tot}', 'FontSize', 10, 'FontName', 'Times')

subplot(326), plot(eylogEF8a, vTotEF8a, 'k', eylogEF8b, vTotEF8b, '--k')
legend('EF8a', 'EF8b', 'Location', 'NorthWest')
ylim([.32 .55])
xlim([0 .4])
set(gca, 'FontSize', 10, 'FontName', 'Times');
set(gcf, 'PaperPosition', [1 1 6 6]);

```

```
hold(gca, 'all');  
print('-dpng', '-r300', 'aAndb.png');
```